UC Berkeley
UC Berkeley Electronic Theses and Dissertations

Title
Towards Precision Standard Model Calculations

Permalink
https://escholarship.org/uc/item/0cp4d788

Author
Girard, Michael

Publication Date
2018

Peer reviewed|Thesis/dissertation

Towards Precision Standard Model Calculations

by

Michael Girard

A dissertation submitted in partial satisfaction of the

requirements for the degree of

Doctor of Philosophy

in

Physics

in the

Graduate Division

of the

University of California, Berkeley

Committee in charge:

Dr. Christian Bauer, Co-chair
Professor Yasunori Nomura, Co-chair
Professor Lawrence Hall
Professor Leo Blitz

Summer 2018

Towards Precision Standard Model Calculations

Abstract

Towards Precision Standard Model Calculations

by

Michael Girard

Doctor of Philosophy in Physics

University of California, Berkeley

Dr. Christian Bauer, Co-chair

Professor Yasunori Nomura, Co-chair

For many years the consistency of the Standard Model(SM) of particle physics has been unflinching. The structure and content of the Standard Model has remained whole in the face of shockingly many experimental tests. Predicting the existence of new particles and yielding incredibly accurate calculations of fundamental measurements have been the hallmark of the Standard Model. Currently, experimentalists are testing several Standard Model quantities to such precision that 5th order terms are needed in theoretical calculations to match this precision. Never-the-less, the predictions of the Standard Model have kept pace with experiment and have yet to be contradicted.

Unfortunately, this incredible stretch of experimental validation comes at a cost. Several very large problems still are without solutions and finding them in the particle content of the Standard Model alone is unlikely. The huge range of scales seen in nature, a dark matter candidate, and the cosmic baryon asymmetry still loom as major flaws in the Standard Model. In this manuscript we aim to increase the accuracy of several Standard Model predictions to push the experimental limits of the Standard Model. We start with a brief introduction to the Standard Model and its sector we will be mainly concerned with, namely QCD. In Chapter 2, we will consider the Standard Model as an effective field theory for a new physics model that resides at a mass scale much higher than the electro-weak scale. By interpreting the SM as an effective theory it allows us to extend the Standard Model Lagrangian with new, higher-dimensional operators that depend on the scale of new physics. We then calculate the next-to-leading order corrections to these operators in QCD and combine these calculations with parton showers via the `POWHEG` method. In the final section of Chapter 2 we present a discussion of the bounds on the scale of new physics that can be drawn from comparing our results to Large-Hadron-Collider(LHC) searches. In the third chapter of this manuscript, we will briefly introduce the importance of W+charm events at the LHC followed by a discussion of NLO QCD calculations and heavy meson fragmentation resummation. Next, we give a general method for combining a fixed order, massive calculation with a massless calculation

with large logarithms resummed. Numerical results of resummation and an implementation of the afore mention method are discussed followed by future outlook.

For William and Alice.

Contents

List of Figures

List of Tables

Executive Summary for non-Experts

As the scales at which humans can probe the world around us become smaller and smaller, the theories needed to describe phenomena at these scales have become more fundamental and unifying. There might not be a better example of this pairing of scale and unification than the history and slow formation of the theory of all known particles in the universe, the Standard Model. The Standard Model has been precisely tested over and over again. Virtually every attempt to experimentally disprove the Standard Model have failed. The Standard Model is the basic theory underlying our understanding of three of the fundamental forces of nature: the electromagnetic force, the weak nuclear force and the strong nuclear force. In this work, the force that we will focus on, as it relates to precise calculations, is the strong nuclear force. The strong nuclear force is the theory of its matter particles, quarks, associated force-carrying particles, called gluons. The strong nuclear force, also called quantum-chromodynamics, suffers from a unique difficulty not seen in the other parts of the Standard Model. At high energies the theory of the strong force is well-behaved and calculations can be carried out in ways similar to those of theories that describe the other forces of the Standard Model. However, at low energy, the description of quarks and gluons becomes unstable to the point of completely breaking down and yielding catastrophically wrong results. Physicists have come up with very creative and novel ways to avoid this catastrophe, some of which we discuss below, but, unfortunately, this problem is a constant challenge to face whenever trying to make an experimental prediction of the strong force.

In what follows, we will discuss two ways in which the precision of Standard Model calculations are increased to yield better experimental predictions.

Firstly, we have supposed a more fundamental theory of physics that exists at energies much higher than those at which the Standard Model is tested today. The Standard Model is now the result of this theory being mapped onto physical scales that we currently have access to. Without adding any additional particles we extended the Standard Model to include more complex interactions. This extension feels the effects of the more fundamental theory and the scale at which it fully resolves. By comparing this enlarged theory's predictions to current experimental results we can gain some insight into the higher energy theory and what it might mean for future discovery.

Secondly, we have combined two calculations, each dealing with the challenge of strong force calculations in their own way. By carefully combining these two calculations we also combine the regions in which the full calculation is valid where as the individual calculations were valid in only one.

Both of these projects have the aim of increasing the precision with which we can predict experimental results and push the limits of the Standard Model. By continually and more effectively testing the Standard Model we can find its failures, and by exploiting these shortcomings we can discover the theory that will ultimately dethrone the Standard Model as the fundamental theory of our universe as we know it.

Chapter 1

Introduction

1.1 History of the Standard Model

The history of physical science has regularly shown us that our current understanding of the universe is, more than likely, merely an effective theory for an underlying and more fundamental theory. As the scales at which humans can probe the world around us become smaller and smaller the theories needed to describe phenomena at these scales have become more fundamental and unifying. There might not be a better example of this pairing of scale and unification than the history and slow formation of the theory of all known particles in the universe, the Standard Model(SM).

The history of the standard model is closely linked to the history of quantum mechanics, and later quantum field theory, as many of the discoveries in quantum mechanics lead to a better understanding of particle behavior and vice versa. Simply noting the Nobel Prizes awarded in the last 150 years one should have impressed upon them the importance of a re-emerging pattern of tension between current theories of particle interactions and experiment followed by theoretical insight leading to a unification of theories.

Starting with the discovery of the electron by J.J. Thomson and the apparent incompatibility of a wave theory of light with experiment, Einstein's 1905 resolution to the photo-electric effect, for which he would win the 1921 Nobel Prize, was one of the first instances of the tension/unification cycle. Another instance of this cycle can be seen in the 1930's after the discovery of the neutron. After it was discovered that nuclei were made of protons and neutrons the issues of nuclei decay and binding forces now were main issues facing the current theories of particle interactions. Enter Hideki Yukawa, who proposed a field theory of nuclear forces and an accompanying new boson, named the pion. It would be more than ten years, but his prediction was ultimately proven correct with the discovery of the pion in 1947 [3]. In 1969 the seemingly nonsensical pattern of baryons and mesons was resolved by the discovery of the up, down and strange quarks and an approximate symmetry relating them, predicted by Gell-Mann and Zweig [4]. The rate of discovery accelerated with the advent of particle colliders and the explosion of discovery in the 1970's with the $J(\psi)$ being

the catalyst(coincidentally this is when the Standard Model got its name). The experimental discovery of the $J(\psi)$, simultaneously showed the existence of a fourth quark, the charm quark, that would allow flavor conserving weak interactions. The necessity of this quark was seen and predicted by Bjorken and Glashow several years before [5]. The SM continued to grow and discoveries culminated in 2012 with the discovery of the capstone of the Standard Model, the Higgs Boson [6].

What is needed now is another era of experimental tension on the Standard Model so that a unifying breakthrough can be made.

1.2   SM and QCD in practice

1.2.1   SM basic building blocks

The SM is defined by its matter particle content and its Lagrangian's invariance under a local SU(3) × SU(2) × U(1) gauge symmetry group. Its matter content is composed of left handed quarks, transforming as $(3, 2, \frac{1}{6})$ under the SU(3) × SU(2) × U(1) gauge groups, right handed quarks, $(3, 1, -\frac{1}{3})$ and $(3, 1, \frac{2}{3})$, left handed leptons, $(1, 2, \frac{1}{2})$, right handed leptons(non-neutrino), $(1, 1, -1)$ and a $(1, 2, 0)$ scalar field, which gives rise to Higgs Boson. The force mediators of the SM are bosons that transforms as adjoint representations of their associated gauge group and are: gluons (8) under the SU(3) color group, the W_1, W_2, W_3 and B, the gauge bosons of the SU(2) × U(1) gauge groups. Through the kinetic interaction of the Standard Model Lagrangian the SU(2) × U(1) gauge bosons interact with the fundamental scalar field, $(1, 2, 0)$, and when this field acquires a vacuum-expectation-value the electroweak symmetry of the W's and B is broken. Under this broken symmetry the W_1 and W_2 combine to become the W^+ and W^- bosons while the W_3 and B rotate into one-another to become the Z boson the massless photon of an intact U(1)$_{EM}$ symmetry.

1.2.2   Quantum chromodynamics

An important sector of the Standard Model, on which much of the following projects are based, is the strong interaction of quantum-chromodynamics (QCD). The QCD Lagrangian is relatively simple to write down as

$$\mathcal{L}_{\text{QCD}} = -\frac{1}{2g^2}\text{tr}\{G_{\mu\nu}G^{\mu\nu}\} + \sum_j \bar{\psi}_j(i\gamma^\mu D_\mu - m_j)\psi_j \tag{1.1}$$

where

$$-\frac{1}{2g^2}\text{tr}\{G_{\mu\nu}G^{\mu\nu}\} = -\frac{1}{4g^2}G^a_{\mu\nu}G^{\mu\nu}_a, \tag{1.2}$$

$$G^a_{\mu\nu} \equiv \partial_\mu A^a_\nu - \partial_\nu A^a_\mu + i f^a_{bc} A^b_\mu A^c_\nu \tag{1.3}$$

and

$$D^\mu \equiv \partial^\mu - ig A^\mu . \tag{1.4}$$

Eq. (1.1) has many interesting subtleties, one of the most important is the fact that the gauge group describing the gluon interaction is non-abelian. As consequence f^a_{bc} is non-zero and leads to a very rich theory of self interacting gauge bosons. By calculating the scale dependence of the coupling constant $\alpha_s = g^2/4\pi$, by

$$\mu^2 \frac{\partial \alpha_s}{\partial \mu^2} = \beta(\alpha_s) \tag{1.5}$$

one finds that the $\beta(\alpha_s)$ function is negative and, in what might be the most fundamental 'minus' sign in human history, the strong coupling constant tends towards zero as the scale increases, $\alpha_s \to 0$ as $\mu \to \infty$. This interesting result is can be rationalized by comparing QCD to the eletromagnetic theory of electrons and photons, called quantum-electrodynamics(QED). An electron, or any particle with electric change, is constantly surrounded by a cloud of particle pairs, quickly coming into and out of existence as allowed by the uncertainty principle. As charge attracts the opposite charge, the positively charged particle in these short lived pairs tend to be closer to the electron and effectively screen the electron's charge. Because of this screening the β function of QED is positive. Contrast this picture with QCD and the self coupling of the gluon plays a key role. A quark is surrounded by a field of rapidly appearing and vanishing particles, just as the electron. However, now this field contains quark/anti-quark pairs AND gluons. If the gluons were not present, the result would be similar to that of QED. The gluons have an effect opposite to that of the quickly vanishing quark pairs and, in the end, the gluon effect is larger leading to the negative beta function. This reasoning of QCD charge being anti-screened is made explicit by calculating the vacuum polarization in QCD(a calculation too lengthy to be repeated here). A fantastic result, for which Gross, Wilczek and Politzer won the 2004 Nobel Prize. Their discovery of "asymptotic freedom" means that at sufficiently high energies, α_s is small and fixed order perturbation theory can be utilized to calculate a wide range of physical observables. Unfortunately, this also leads to a phenomenon known as "confinement". Just as α_s becomes small at high energies, it also becomes large at low energies. As scale decreases, α_s grows until eventually it becomes larger than one, near a scale labeled Λ_{QCD}. While confinement is great for the formation of protons, neutrons and heavy nuclei it spoils perturbative expansions in α_s as higher order terms are now as large, if not larger, than lower order terms and the theory becomes incalculable. As we bring the tools of QCD calculations to bear on

hadron collider events, we will see that this divergence manifests in two ways that are critical to collider observables. These are the quarks' ability to couple strongly to soft and collinear gluons. These divergent couplings to soft and collinear gluon radiation is a major hurdle on the path to finite experimental predictions and in what follows we will discuss methods to overcome this hurdle, and in some cases step around it.

1.3   Precision Tests

To say the Standard Model has been incredibly successful in providing experimental predictions would be understating its value to the science. Time and time again the SM has provided robust predictions that withstand highly stringent experimental limits. Tests like the prediction of the top quark mass [7, 8], flavor processes [9, 10, 11] and existence of the Higgs Boson [6], all put forth the Standard Model as a highly tested theory. Not only are colliders allowing for direct measurements and tests of the Standard Model but recently atom interferometry has allowed a measurement of $\alpha_{\mathbf{EM}}$ that can probe corrections to the fine structure constant to the fifth order in QED Feynman diagrams [12]. The inner workings of QCD have also been tested to very high precision. The running of α_s, Eq. (1.5), has been measured in many different experimental settings and scales, see Figure 1.1a, [13]. The precision tests of QCD are almost to numerous to point out but one such of QCD in collider events can be seen in Figure 1.1b, which shows the total cross section of QCD radiation production as a function of the energy scale of the underlying event [14].

1.4   Flaws and Missing Pieces

However, the Standard Model is most probably not the ultimate theory of particle physics describing our universe. For all its success the SM has glaring flaws that are unlikely to be resolved by the particle content of the SM alone. The observed cosmic Baryon asymmetry, a dark matter candidate and the hierarchy of scales in the Standard Model are all major issues that need explanations. Current searches for Beyond the Standard Model (BSM) physics have failed to show any signals, beyond the occasional slight deviation, that would indicate the scale of new physics is much below $10\,TeV$. Such searches have pushed possible mass scales of minimally super-symmetric extensions to the Standard Model, gluinos, light stops and winos, above $1\,\mathrm{TeV}$ in some cases [15], see Figures 1.1c and 1.1d.

While exploring the space of BSM models is still important in the search for particles that exist outside the realm of the Standard Model, another approach should also be employed to test the Standard Model for experimental deviations. New and unforeseen physics is manifestly hidden in those deviations and should be explored. By increasing the precision with which calculations are made in the SM and also by utilizing the SM as an effective theory we can push observable predictions into new experimental phase spaces where they can be meaningfully tested. What follows are two projects that aim to do just this. We
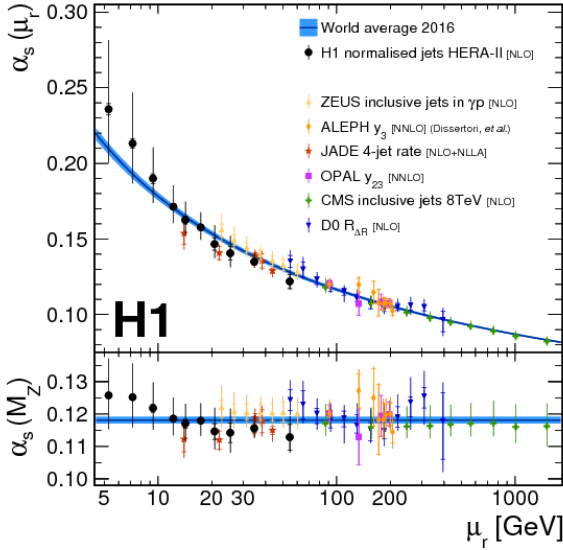
(a) Plot from [13] showing the experimental tests of the running of α_s
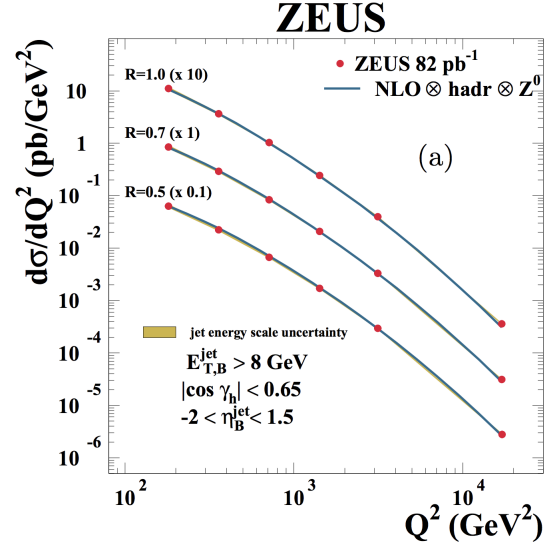
(b) Plot which shows the total cross section of QCD radiation production, as a function of the energy scale of the underlying event [14]
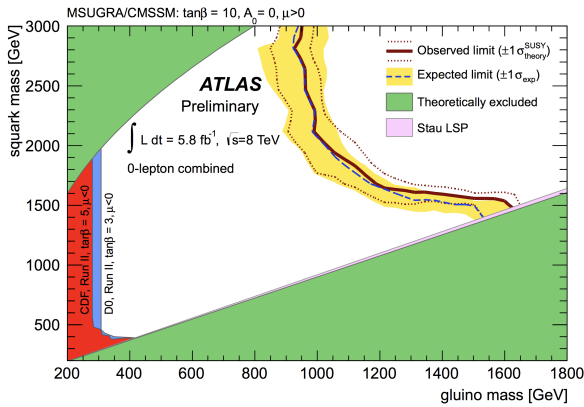
(c) Plot from [15] showing MSUGRA/CMSSM exclusion limits of ATLAS expressed in terms of squark and gluino masses
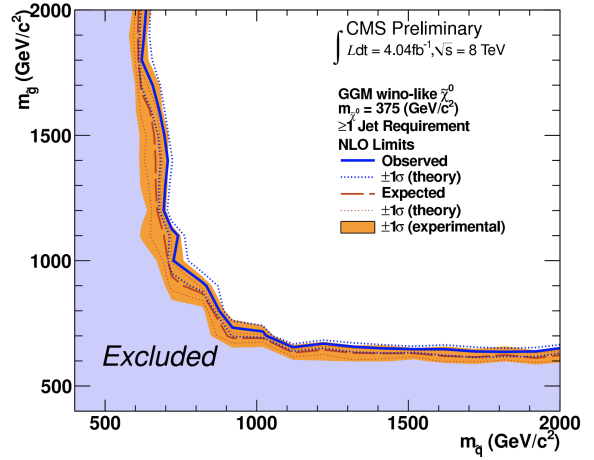
(d) Plot from [15] showing CMS limits in general gauge mediation for wino-like neutralinos from the diphoton plus $E_T^{missing}$ analysis

Figure 1.1: Plots of precision tests of the Standard model and beyond the Standard Model searches.

first discuss the Standard Model as an effective field theory, that is sensitive to the scale of new physics , Λ, through its higher dimensional operators and coefficients. We further consider its use to probe the corrections to several important collider observables. Secondly, we present a method for increasing precision in collider events that produce a W Boson and charm quark with very large transverse momentum. Events of this type probe a region of phase space that simple fixed order calculations fail to describe and have direct effect on the uncertainty of important Standard Model measurables.

Chapter 2

SM-EFT, QCD corrections and parton showers

2.1 Theoretical Introduction

In the following chapter we present an extended theory of the Standard Model in order to better investigate the scale of new physics at the Large Hadron Collider. In this extended theory the Standard Model is taken to be an effective field theory of some higher scale physical model. The heavier degrees of freedom of the high scale new physics has been integrated out and at the low scale accessible by the LHC the Standard Model in only sensitive to the heavy states through non-renormalizable, higher-dimension operators whose couplings are suppressed by powers of the scale at which the new physics is realized. In the simplest version of these type theories, it is assumed that there are no new fields in the low physics scale, that is near the electro-weak symmetry breaking scale, and that the scalar boson observed as the Higgs boson is part of a field that transforms as a $(1, 2, 0)$ in the $SU(3) \times SU(2) \times U(1)$ gauge group, than the new effective field theory created by integrating out heavy states from new physics is called the Standard Model Effective Field Theory, SM-EFT, [16, 17, 18, 19, 20].

In this work we will utilize the full set of dimension six operators in the SM-EFT in the basis used in [17]. These operators yield the tree level corrections to Drell-Yan processes in both the charged and neutral currents. Higgs production via Vector-Boson-Fusion(VBF) and associated Higgs + Z or W bosons are also affected by these operators. To this we include the next-to-leading order QCD corrections to the hard partonic process and match with parton shower in the POWHEG method, from [21, 22, 23], and Refs. [24, 25, 26].

What follows is our analysis of including NLO QCD corrections to these collider events, Drell-Yan, WH or ZH and Higgs production via VBF, using a broad set of operators in the more general POWHEG method. By using the POWHEG method we allow for more flexibility in experimental predictions. The results presented in this chapter is work from Ref. [27], published by the author of this manuscript and others.

2.2 The operator basis

Before discussing dimension-six operators, we define a few SM ingredients in greater detail needed to establish our conventions. The SM Lagrangian is completely determined by the invariance under the Lorentz group, the gauge group $SU(3)_c \times SU(2)_L \times U(1)_Y$, and by the matter content. We consider here the SM in its minimal version, with three families of leptons and quarks, and one scalar doublet. The left-handed quarks and leptons transform as doublets under $SU(2)_L$

$$q_L = \begin{pmatrix} u_L \\ d_L \end{pmatrix}, \qquad \ell_L = \begin{pmatrix} \nu_L \\ e_L \end{pmatrix}, \tag{2.1}$$

while the right-handed quarks, u_R and d_R, and charged leptons, e_R, are singlets under $SU(2)_L$. We do not include sterile right-handed neutrinos, but their effects on e.g. W production can be straightforwardly included [28]. The scalar field φ is a doublet under $SU(2)_L$. In the unitary gauge we have

$$\varphi = \frac{v}{\sqrt{2}} U(x) \begin{pmatrix} 0 \\ 1 + \frac{h}{v} \end{pmatrix}, \tag{2.2}$$

where $v = 246$ GeV is the scalar vacuum expectation value (*vev*), h is the physical Higgs field and $U(x)$ is a unitary matrix that encodes the Goldstone bosons. By $\tilde{\varphi}$ we denote $\tilde{\varphi} = i\tau_2 \varphi^*$.

The gauge interactions are determined by the covariant derivative

$$D_\mu = \partial_\mu + i\frac{g}{2}\boldsymbol{\tau} \cdot W_\mu + ig'Y B_\mu + ig_s G_\mu^a t^a \tag{2.3}$$

where B_μ, W_μ^I and G_μ^a are the $U(1)_Y$, $SU(2)_L$ and $SU(3)_c$ gauge fields, respectively, and g', g, and g_s are their gauge couplings. Furthermore, $\boldsymbol{\tau}/2$ and t^a are the $SU(2)_L$ and $SU(3)_c$ generators, in the representation of the field on which the derivative acts. In the SM, the gauge couplings g and g' are related to the electric charge and the Weinberg angle by $gs_w = g'c_w = e$, where $e > 0$ is the charge of the positron and $s_w = \sin\theta_W$, $c_w = \cos\theta_W$. We will shortly discuss how these relations are affected in the presence of dimension-six operators. The hypercharge assignments under the group are $1/6$, $2/3$, $-1/3$, $-1/2$, -1, and $1/2$ for q_L, u_R, d_R, ℓ_L, e_R, and φ, respectively. The SM Lagrangian then consists of the Lorentz- and gauge-invariant terms with dimension $d \leq 4$ that can be constructed from the above fields.

The processes we aim to study, Drell-Yan, WH, ZH, and VBF, are affected by many dimension-six operators. Following the notation of Ref. [17], we classify the relevant operators according to their content of gauge (denoted by X), fermion (ψ), and scalar fields (φ). The operators that contribute at tree level fall in the following five classes

$$\mathcal{L} = \mathcal{L}_{X^2\varphi^2} + \mathcal{L}_{\psi^2 X\varphi} + \mathcal{L}_{\psi^2\varphi^2 D} + \mathcal{L}_{\psi^2\varphi^3} + \mathcal{L}_{\psi^4}. \tag{2.4}$$

Here $\mathcal{L}_{X^2\varphi^2}$ contains operators with two scalars and two gauge bosons. At the order we are working and for the processes we are considering, the only relevant operators are the ones involving $SU(2)_L$ and $U(1)_Y$ gauge bosons:

$$
\begin{aligned}
\mathcal{L}_{X^2\varphi^2} &= C_{\varphi W}\frac{\varphi^\dagger \varphi}{v^2}W^I_{\mu\nu}W^{I\,\mu\nu} + C_{\varphi B}\frac{\varphi^\dagger \varphi}{v^2}B_{\mu\nu}B^{\mu\nu} + C_{\varphi WB}\frac{\varphi^\dagger \tau^I \varphi}{v^2}W^I_{\mu\nu}B^{\mu\nu} \\
&+ C_{\varphi \tilde{W}}\frac{\varphi^\dagger \varphi}{v^2}\tilde{W}^I_{\mu\nu}W^{I\,\mu\nu} + C_{\varphi \tilde{B}}\frac{\varphi^\dagger \varphi}{v^2}\tilde{B}_{\mu\nu}B^{\mu\nu} + C_{\varphi \tilde{W}B}\frac{\varphi^\dagger \tau^I \varphi}{v^2}\tilde{W}^I_{\mu\nu}B^{\mu\nu}
\end{aligned}
\tag{2.5}
$$

where $W^I_{\mu\nu}$ and $B_{\mu\nu}$ denote the $SU(2)_L$ and $U(1)_Y$ field strengths, and $\tilde{X}_{\mu\nu} = \varepsilon_{\mu\nu\alpha\beta}X^{\alpha\beta}/2$. The operators in the first line of Eq. (2.5) are CP-even, while those on the second line violate CP. Here, and in what follows, we define the coefficients of dimension-six operators to be dimensionless. Thus, $C_{\varphi X}$ and $C_{\varphi \tilde{X}}$ scale as v^2/Λ^2, where Λ is the new physics scale. The remaining operators in the class $\mathcal{L}_{X^2\varphi^2}$ involve the gluon field strength $G_{\mu\nu}$. While these are very interesting for Higgs boson production via gluon fusion, they contribute to the processes we are considering – all of which are (anti-)quark-initiated – only at higher order, and we neglect them.

The classes $\psi^2 X\varphi$ and $\psi^2\varphi^2 D$ both contain fermion bilinears. The former class consists of dipole operators, of which we focus on the dipole couplings of quarks and leptons to the $SU(2)_L$ and $U(1)_Y$ gauge bosons:

$$
\begin{aligned}
\mathcal{L}_{\psi^2 X\varphi} &= -\frac{1}{\sqrt{2}}\bar{q}_L\sigma^{\mu\nu}(g'\Gamma^u_B B_{\mu\nu} + g\Gamma^u_W \boldsymbol{\tau}\cdot \boldsymbol{W}_{\mu\nu})\frac{\tilde{\varphi}}{v^2}u_R \\
&-\frac{1}{\sqrt{2}}\bar{q}_L\sigma^{\mu\nu}(g'\Gamma^d_B B_{\mu\nu} + g\Gamma^d_W \boldsymbol{\tau}\cdot \boldsymbol{W}_{\mu\nu})\frac{\varphi}{v^2}d_R \\
&-\frac{1}{\sqrt{2}}\bar{\ell}_L\sigma^{\mu\nu}(g'\Gamma^e_B B_{\mu\nu} + g\Gamma^e_W \boldsymbol{\tau}\cdot \boldsymbol{W}_{\mu\nu})\frac{\varphi}{v^2}e_R + \text{h.c.} \ .
\end{aligned}
\tag{2.6}
$$

Here $\Gamma^{u,d,e}_W$ and $\Gamma^{u,d,e}_B$ are generally 3×3 matrices in flavor space, which we will discuss in more detail shortly. In what follows we trade the couplings to the B gauge field, $\Gamma^{u,d,e}_B$, for those to the photon field

$$
\Gamma^u_\gamma = \Gamma^u_B + \Gamma^u_W, \qquad \Gamma^d_\gamma = \Gamma^d_B - \Gamma^d_W \quad \text{and} \quad \Gamma^e_\gamma = \Gamma^e_B - \Gamma^e_W.
\tag{2.7}
$$

$\mathcal{L}_{\psi^2\varphi^2 D}$ contains corrections to the SM couplings of the quarks and leptons to the Z and W bosons, which, in gauge invariant form, appear as

$$
\begin{aligned}
\mathcal{L}_{\psi^2\varphi^2 D} &= -\frac{\varphi^\dagger i\overleftrightarrow{D}_\mu\varphi}{v^2}\left(\bar{q}_L\gamma^\mu\, c^{(1)}_{Q\varphi}q_L + \bar{u}_R\gamma^\mu\, c_{U\varphi}u_R + \bar{d}_R\gamma^\mu\, c_{D\varphi}d_R\right) \\
&-\frac{\varphi^\dagger i\overleftrightarrow{D}^I_\mu\varphi}{v^2}\,\bar{q}_L\tau^I\gamma^\mu c^{(3)}_{Q\varphi}q_L + \left(i\frac{2}{v^2}\tilde{\varphi}^\dagger D_\mu\varphi\,\bar{u}_R\gamma^\mu\xi d_R + \text{h.c.}\right) \\
&-\frac{\varphi^\dagger i\overleftrightarrow{D}_\mu\varphi}{v^2}\left(\bar{\ell}_L\gamma^\mu\, c^{(1)}_{L\varphi}\ell_L + \bar{e}_R\gamma^\mu\, c_{e\varphi}e_R\right) - \frac{\varphi^\dagger i\overleftrightarrow{D}^I_\mu\varphi}{v^2}\,\bar{\ell}_L\tau^I\gamma^\mu c^{(3)}_{L\varphi}\ell_L.
\end{aligned}
\tag{2.8}
$$

Here $\overleftrightarrow{D}_\mu = D_\mu - \overleftarrow{D}_\mu$, $\overleftrightarrow{D}^I_\mu = \tau^I D_\mu - \overleftarrow{D}_\mu \tau^I$, and $c^{(1)}_{Q\varphi}$, $c^{(3)}_{Q\varphi}$, $c_{U\varphi}$, $c_{D\varphi}$, $c^{(1)}_{L\varphi}$, $c^{(3)}_{L\varphi}$, $c_{e\varphi}$ are hermitian, 3×3 matrices, while ξ is a generic 3×3 matrix. The operators $c^{(1)}_{L\varphi}$, $c^{(3)}_{L\varphi}$, $c_{e\varphi}$ couple lepton bilinears to the weak bosons, thus affecting Z and W production at tree level. However, these operators are strongly constrained by LEP measurements of the physics at the Z pole [29]. Furthermore, the Z and W production cross sections induced by these operators have the same shape as the SM, making it hard to identify them at collider. For these reasons, we neglect them in what follows.

The remaining operators involving quark bilinears in the dimension-six SM-EFT Lagrangian are corrections to the quark and lepton Yukawa couplings

$$\mathcal{L}_{\psi^2\varphi^3} = -\sqrt{2}\frac{\varphi^\dagger\varphi}{v^2}\left(\bar{q}_L Y'_u \tilde{\varphi} u_R + \bar{q}_L Y'_d \varphi d_R + \bar{\ell}_L Y'_e \varphi e_R\right). \tag{2.9}$$

These couplings are mainly constrained by Higgs boson production via quark-antiquark annihilation and by the Higgs boson branching ratios, but we will see that the quark couplings $Y'_{u,d}$ also give interesting contributions to WH and ZH.

Finally, we consider the following semileptonic four-fermion operators,

$$\begin{aligned}
\mathcal{L}_{\psi^4} =& -\frac{4G_F}{\sqrt{2}}\Bigg\{ C^{(1)}_{LQ}\,\bar{\ell}_L\gamma^\mu\ell_L\,\bar{q}_L\gamma_\mu q_L + C^{(3)}_{LQ}\,\bar{\ell}_L\boldsymbol{\tau}\gamma^\mu\ell_L\cdot\bar{q}_L\boldsymbol{\tau}\gamma_\mu q_L + C_{eu}\,\bar{e}_R\gamma^\mu e_R\,\bar{u}_R\gamma_\mu u_R \\
&+ C_{ed}\,\bar{e}_R\gamma^\mu e_R\,\bar{d}_R\gamma_\mu d_R + C_{Lu}\,\bar{\ell}_L\gamma^\mu\ell_L\,\bar{u}_R\gamma_\mu u_R + C_{Ld}\,\bar{\ell}_L\gamma^\mu\ell_L\,\bar{d}_R\gamma_\mu d_R \\
&+ C_{Qe}\,\bar{e}_R\gamma^\mu e_R\,\bar{q}_L\gamma_\mu q_L\Bigg\} \\
&- \frac{4G_F}{\sqrt{2}}\Bigg\{ C_{LedQ}\,\bar{\ell}^i_L e_R\,\bar{d}_R q^i_L + C^{(1)}_{LeQu}\,\varepsilon^{ij}\bar{\ell}^i_L e_R\,\bar{q}^j_L u_R + C^{(3)}_{LeQu}\,\varepsilon^{ij}\bar{\ell}^i_L\sigma^{\mu\nu}e_R\,\bar{q}^j_L\sigma_{\mu\nu}u_R + \text{h.c.}\Bigg\}.
\end{aligned} \tag{2.10}$$

Of these operators, only a few affect charged currents, introducing new Lorentz structures, such as scalar-scalar and tensor-tensor interactions. All of the above operators modify neutral currents and the couplings are, in general, four-indices tensors.

Having introduced the dimension-six operators of interest, we will first discuss how these new interactions affect the SM couplings. The assumptions on the flavor structure of the introduced couplings are discussed in Section 2.2.2.

2.2.1 Corrections to SM couplings

In the SM the gauge couplings g and g', the electric charge e, the Fermi constant G_F, the Weinberg angle $\sin\theta_W$, the gauge boson masses, and the Higgs boson mass and *vev* are not independent, but are connected by several relations, which hold at tree level, and are modified in a testable way by radiative corrections. Including the higher dimensional operators of Eqs. (2.5), (2.6), (2.8) and (2.10) modifies these relations, making it important to specify the input that is taken from the experiments. Here we use as experimental input

the values of the weak boson and Higgs boson masses m_Z, m_W, m_H [30], G_F, the electric charge, and $\sin\theta_W$ as extracted from the lepton asymmetries at LEP [30]. In the presence of new physics, these experimental values would include contributions from dimension-six operators, which we now describe.

The operators in Eq. (2.5) affect the normalization of the gauge bosons, and their masses, inducing, in particular, mass and kinetic mixing between W_μ^3 and B_μ. Here we follow Ref. [16], and diagonalize the gauge boson mass terms up to corrections of $\mathcal{O}(v^4/\Lambda^4)$, by rotating the W_3 and B_μ fields according to

$$
\begin{aligned}
W_\mu^3 &= s_{0w}(1+\alpha_{AA})A_\mu + (c_{0w}(1+\alpha_{ZZ}) - s_{0w}\alpha_{AZ})\, Z_\mu, & (2.11) \\
B_\mu &= c_{0w}(1+\alpha_{AA})A_\mu - (s_{0w}(1+\alpha_{ZZ}) + c_{0w}\alpha_{AZ})\, Z_\mu, & (2.12)
\end{aligned}
$$

where we have introduced

$$
\begin{aligned}
\alpha_{AA} &= s_{0w}^2\, C_{\varphi W} + c_{0w}^2\, C_{\varphi B} - s_{0w}c_{0w}\, C_{\varphi WB}, & (2.13) \\
\alpha_{ZZ} &= c_{0w}^2\, C_{\varphi W} + s_{0w}^2\, C_{\varphi B} + s_{0w}c_{0w}\, C_{\varphi WB}, & (2.14) \\
\alpha_{AZ} &= 2s_{0w}c_{0w}(C_{\varphi B} - C_{\varphi W}) + \left(c_{0w}^2 - s_{0w}^2\right) C_{\varphi WB}. & (2.15)
\end{aligned}
$$

The subscript 0 has been introduced to stress that Eqs. (2.13)-(2.15) involve the Weinberg angle in the SM

$$
c_{0w} = \cos\theta_W^0 = \frac{g}{\sqrt{g^2 + g'^2}}. \tag{2.16}
$$

In a similar way, we redefine $W_\mu^{1,2}$ to ensure the kinetic term of the W boson is canonically normalized. The weak boson masses are then given by Ref. [16]

$$
\begin{aligned}
m_W &= m_W^0\left(1 + C_{\varphi W}\right), & m_W^0 &= \frac{gv}{2}, & (2.17) \\
m_Z &= m_Z^0\left(1 + \alpha_{ZZ}\right), & m_Z^0 &= \frac{gv}{2c_{0w}}, & (2.18)
\end{aligned}
$$

for which we use the experimental values $m_W = 80.4$ GeV and $m_Z = 91.2$ GeV [30]. Notice that here we focused on the subset of the complete dimension-six Lagrangian presented in the previous section. The full expression of the W and Z boson masses in the SM-EFT are given in Ref. [16, 20].

The Higgs *vev* is defined in term of the observed Fermi constant. Up to corrections of $\mathcal{O}(v^4/\Lambda^4)$, the operators in Eqs. (2.5), (2.6), (2.8) and (2.10) do not affect the relation between v and G_F, and we still have

$$
v = (\sqrt{2}G_F)^{-1/2} = 246.2\,\mathrm{GeV}, \tag{2.19}
$$

where G_F is the measured Fermi constant, extracted from muon decay, $G_F = 1.166 \cdot 10^{-5}$ GeV^{-2}. Within the general SM-EFT the above relation receives corrections from additional operators that we do not consider here [16]. For example, at dimension-six Eq. (2.19) is

altered by the operator $c_{L\varphi}^{(3)}$ in Eq. (2.8), which modifies the leptonic couplings of the W. Using the physical masses and G_F, we define the effective couplings

$$g_{\text{eff}} = 2\frac{m_W}{v} = 0.653, \qquad \left(\frac{g}{c_w}\right)_{\text{eff}} = 2\frac{m_Z}{v} = 0.741, \tag{2.20}$$

which are useful in expressing the couplings of the quarks to the W and Z bosons. The electric charge is given by Ref. [30]

$$e = gs_{0w}\left(1 + \alpha_{AA}\right), \qquad \alpha(m_Z) = \frac{e(m_Z)^2}{4\pi} = 1/127.95. \tag{2.21}$$

Finally, we use the lepton asymmetry parameter A_e, as measured at LEP [30], to determine the Weinberg angle. A_e is related to the ratio of the electron vector and axial coupling, and, since we are not introducing new $\bar{e}eZ$ interactions, this ratio is only affected by the definition of the Z field,

$$\frac{g_V^e}{g_A^e} = 1 - 4|Q_e|s_{0w}^2\left(1 + \frac{c_{0w}}{s_{0w}}\alpha_{AZ}\right). \tag{2.22}$$

Using $g_V^e/g_A^e = 0.151 \pm 0.002$ [30], we define an effective s_w

$$(s_w^2)_{\text{eff}} = s_{0w}^2\left(1 + \frac{c_{0w}}{s_{0w}}\alpha_{AZ}\right) = 0.231. \tag{2.23}$$

With the above definitions, the SM couplings of the Z and W boson to quarks can be written as

$$\begin{aligned}
\mathcal{L} &= -\left(\frac{g}{c_w}\right)_{\text{eff}}\left\{\bar{q}_L\left(T_3 - Q(s_w^2)_{\text{eff}}\right)\gamma^\mu q_L\, Z_\mu - Q_u(s_w^2)_{\text{eff}}\,\bar{u}_R\gamma^\mu u_R\, Z_\mu \right.\\
&\quad \left. -Q_d(s_w^2)_{\text{eff}}\,\bar{d}_R\gamma^\mu d_R\, Z_\mu\right\} - \frac{(g)_{\text{eff}}}{\sqrt{2}}\bar{u}_L\gamma^\mu d_L W_\mu^+,
\end{aligned} \tag{2.24}$$

where T_3 is the third component of isospin, $Q = \text{diag}(Q_u, Q_d)$ is the quark charge matrix. The couplings of the Z and W boson to the Higgs boson are given by

$$\mathcal{L} = \frac{m_W^2}{v}h\left(W_1^\mu W_{1\,\mu} + W_2^\mu W_{2\,\mu}\right) + \frac{m_Z^2}{v}hZ^\mu Z_\mu. \tag{2.25}$$

We will compute the effects of dimension-six operators with respect to these definitions.

Lastly, the Yukawa operators in Eq. (2.9) affect the definition of the quark masses. We define the Yukawa Lagrangian in the presence of dimension-four and dimension-six operators as

$$\mathcal{L} = -v\bar{u}_L Y_u u_R\left(1 + \frac{h}{v}\right) - v\bar{d}_L Y_d d_R\left(1 + \frac{h}{v}\right) - \bar{u}_L Y_u' u_R h, -\bar{d}_L Y_d' d_R h + \text{h.c.} \tag{2.26}$$

where

$$Y_u = Y_u^0 + \frac{1}{2}Y_u', \qquad Y_d = Y_d^0 + \frac{1}{2}Y_d', \tag{2.27}$$

and $Y_{u,d}^0$ denote the Yukawa couplings in the SM. The matrices Y_u and Y_d can always be made diagonal and real by appropriate field redefinitions, and are determined by the observed quark masses, $M_{u,d} = vY_{u,d}$. In the mass basis, $Y_{u,d}'$ are generic 3×3 complex matrices. In what follows we will neglect the contribution of $Y_{u,d}$, which, for processes involving light quarks, is always negligible, and we will focus on $Y_{u,d}'$, which, being unrelated to the light quark masses, need to be independently constrained.

2.2.2 Flavor assumptions

Given the already large number of operators, keeping the flavor structure of Eqs. (2.6), (2.8) and (2.10) completely generic is a daunting task. We therefore work under two simplifying assumptions:

1. Lepton universality.

2. No tree-level flavor-changing neutral currents (FCNCs).

Lepton universality only affects the four-fermion and leptonic dipole operators in Eqs. (2.10) and (2.6), implying that they have a trivial flavor structure in the lepton sector, with the same couplings for the electron, muon and tau. This assumption can easily be relaxed by setting the `vdecaymode` flag in the `powheg.input` file to separately only select electron, muon or tau final states.

To enforce that there are no tree-level FCNCs we first rotate to the mass basis of the quarks, by performing the following transformation

$$u_{L,R} \to U_{L,R}^u u_{L,R}, \qquad d_{L,R} \to U_{L,R}^d d_{L,R}, \tag{2.28}$$

where $U_{L,R}^{u,d}$ are unitary matrices that diagonalize the mass matrices

$$(U_L^u)^\dagger M_u U_R^u = \mathrm{d}iag(m_u, m_c, m_t), \qquad (U_L^d)^\dagger M_d U_R^d = \mathrm{d}iag(m_d, m_s, m_b), \tag{2.29}$$

and the CKM matrix is $V_{\mathrm{CKM}} = (U_L^u)^\dagger U_L^d$. The rotations (2.28) affect the flavor structure of the dimension-six operators. For most operators, the effects of the transformation can be trivially absorbed by a redefinition of the couplings. For example, for the right-handed W current ξ, the net effect of switching to the mass basis is to replace the matrix ξ with $\xi' = (U_R^u)^\dagger \, \xi \, U_R^d$. Since ξ is an arbitrary matrix, the change has no practical effect. $c_{U\varphi}$, $c_{D\varphi}$, $Y_{u,d}'$, C_{eu}, C_{ed}, C_{Lu}, C_{Ld} and C_{Qe} only affect neutral currents, and we simply define them to be diagonal in the mass basis.

On the other hand, the rotation (2.28) has nontrivial consequences for operators that affect both neutral and charged currents. For example, for $c_{Q\varphi}^{(1)}$ and $c_{Q\varphi}^{(3)}$ we find, in the

unitary gauge and the weak basis,

$$
\begin{aligned}
\mathcal{L} \;=\; & -\left(1+\frac{h}{v}\right)^2 \left\{ \frac{g}{2c_w}\bar{q}_L\gamma^\mu Z_\mu \left(c_{Q\varphi}^{(1)}-c_{Q\varphi}^{(3)}\tau_3\right) q_L - \frac{g}{\sqrt{2}}\bar{u}_L\gamma^\mu W_\mu^+ \, c_{Q\varphi}^{(3)}d_L \right. \\
& \left. -\frac{g}{\sqrt{2}}\bar{d}_L\gamma^\mu W_\mu^- \, c_{Q\varphi}^{(3)}u_L \right\}.
\end{aligned}
\tag{2.30}
$$

Transforming to the mass basis, the left-handed couplings of the Z boson to u-type and d-type quarks are

$$
\left(c_{Q\varphi}^{(1)}-c_{Q\varphi}^{(3)}\right)' \;=\; (U_L^u)^\dagger \left(c_{Q\varphi}^{(1)}-c_{Q\varphi}^{(3)}\right) U_L^u \qquad \left(c_{Q\varphi}^{(1)}+c_{Q\varphi}^{(3)}\right)' = (U_L^d)^\dagger \left(c_{Q\varphi}^{(1)}+c_{Q\varphi}^{(3)}\right) U_L^d.
$$

If we now require all the Z couplings in the mass basis (the primed matrices) to be diagonal, this induces some non-diagonal W couplings,

$$
\begin{aligned}
\mathcal{L} \;=\; & \frac{g}{\sqrt{2}}\left(1+\frac{h}{v}\right)^2 \bar{u}_L\gamma^\mu W_\mu^+ \left(\frac{1}{2}\left[V_{\mathrm{CKM}},c_{Q\varphi}^{(1)\prime}\right]+\frac{1}{2}\left\{V_{\mathrm{CKM}},c_{Q\varphi}^{(3)\prime}\right\}\right) d_L \\
& +\frac{g}{\sqrt{2}}\left(1+\frac{h}{v}\right)^2 \bar{d}_L\gamma^\mu W_\mu^- \left(-\frac{1}{2}\left[V_{\mathrm{CKM}}^\dagger,c_{Q\varphi}^{(1)\prime}\right]+\frac{1}{2}\left\{V_{\mathrm{CKM}}^\dagger,c_{Q\varphi}^{(3)\prime}\right\}\right) u_L.
\end{aligned}
\tag{2.31}
$$

Thus, when we assume no tree-level FCNCs are induced, the non-diagonal effects in the W couplings are determined by the CKM matrix.

In a similar way, when we take the Z and γ dipoles to be diagonal, this results in the following couplings for the W dipoles

$$
\mathcal{L} \;=\; -\frac{g}{\sqrt{2}v}\left(1+\frac{h}{v}\right)\left\{ \bar{d}_L V_{\mathrm{CKM}}^\dagger \Gamma_W^u \sigma^{\mu\nu} u_R W_{\mu\nu}^- + \bar{u}_L V_{\mathrm{CKM}}\Gamma_W^d \sigma^{\mu\nu} d_R W_{\mu\nu}^+ \right\} + \mathrm{h.c.}
\tag{2.32}
$$

Finally, for the four-fermion operators we again enforce all the neutral-current couplings to be flavor diagonal in the mass basis, and we define the diagonal matrices

$$
\begin{aligned}
C_{LQ,U} &= \mathrm{diag}(C_{LQ,u},C_{LQ,c},C_{LQ,t}) = C_{LQ}^{(1)}-C_{LQ}^{(3)}, \\
C_{LQ,D} &= \mathrm{diag}(C_{LQ,d},C_{LQ,s},C_{LQ,b}) = C_{LQ}^{(1)}+C_{LQ}^{(3)}.
\end{aligned}
\tag{2.33}
$$

Assuming C_{LedQ}, $C_{LeQu}^{(1)}$, $C_{LeQu}^{(3)}$ to be diagonal, the charged-current interactions are

$$
\begin{aligned}
\mathcal{L} \;=\; & -\frac{4G_F}{\sqrt{2}}\left\{ \bar{\nu}_L\gamma^\mu e_L \bar{d}_L\gamma_\mu \left(C_{LQ,D}V_{CKM}^\dagger - V_{CKM}^\dagger C_{LQ,U}\right) u_L \right. \\
& \left. +\bar{\nu}_L e_R \left(\bar{d}_R C_{LedQ}V_{CKM}^\dagger u_L + \bar{d}_L V_{CKM}^\dagger C_{LeQu}^{(1)}u_R\right) + \bar{\nu}_L \sigma^{\mu\nu} e_R \, \bar{d}_L V_{CKM}^\dagger C_{LeQu}^{(3)}\sigma_{\mu\nu}u_R \right\} \\
& +\mathrm{h.c.}
\end{aligned}
\tag{2.34}
$$

Hermiticity of the Lagrangian in Eqs. (2.8) and (2.10) forces the couplings $c_{U\varphi}$, $c_{D\varphi}$, $c_{Q\varphi}^{(1)}$, $c_{Q\varphi}^{(3)}$, C_{eu}, C_{ed}, C_{Lu}, C_{Ld} and C_{Qe} to be real. These matrices can acquire imaginary components if one relaxes the flavor assumptions, and allows for off-diagonal Z couplings. On the other hand, the dipole couplings $\Gamma_{W,\gamma}^{u,d,e}$, the right-handed charge-current ξ, the Yukawa couplings $Y_{u,d}'$, and the scalar and tensor interactions C_{LedQ}, $C_{LeQu}^{(1)}$, $C_{LeQu}^{(3)}$ can have an imaginary part.

One can explore additional flavor structures such as minimal flavor violation [31]. For charge-current processes it is easy to allow more general flavor structures, by setting the non-diagonal entries of the 3×3 flavor matrices of couplings in `initcouplings.f` to the desired values. For neutral-current processes, non-diagonal Z couplings would require one to add new partonic channels, which at the moment are not included but can be easily incorporated, if necessary.

2.2.3 Renormalization

The coefficients of most operators in Eq. (2.4) do not run in QCD at one loop. The exceptions are the quark Yukawa couplings in Eq. (2.9) and the scalar operators in Eq. (2.10), whose coefficients $Y_{u,d}'$, $C_{LeQu}^{(1)}$ and C_{LedQ} obey the same renormalization group equation (RGE) as the quark masses, the dipole operators in Eq. (2.6), and the tensor operator in Eq. (2.10). The scalar and tensor operators satisfy

$$\frac{d}{d\log\mu}C_S = \frac{\alpha_s}{4\pi}\sum_n\left(\frac{\alpha_s}{4\pi}\right)^n\gamma_S^{(n)}C_S, \qquad C_S\in\left\{Y_u',Y_d',C_{LeQu}^{(1)},C_{LedQ}\right\}$$

$$\frac{d}{d\log\mu}C_T = \frac{\alpha_s}{4\pi}\sum_n\left(\frac{\alpha_s}{4\pi}\right)^n\gamma_T^{(n)}C_T, \qquad C_T\in\left\{\Gamma_W^u,\Gamma_W^d,\Gamma_\gamma^u,\Gamma_\gamma^d,C_{LeQu}^{(3)}\right\}, \quad (2.35)$$

where the two loop anomalous dimensions are [32, 33, 34]

$$\gamma_S^{(0)} = -6C_F, \qquad \gamma_S^{(1)} = -\left(3C_F + \frac{97}{3}N_C - \frac{10}{3}n_f\right)C_F,$$

$$\gamma_T^{(0)} = 2C_F, \qquad \gamma_T^{(1)} = \left(\frac{257}{9}N_C - 19C_F - \frac{26}{9}n_f\right)C_F. \quad (2.36)$$

Here $C_F = 4/3$, $N_C = 3$ and $n_f = 5$ is the number of light flavors. All the other coefficients do not run in QCD, and we neglect electroweak loops.

By default, all dimension-six corrections are switched off in the `POWHEG` input card. To investigate the effect of one or more dimension-six operator, the user needs to set the flag `dim6` to 1 and specify the values of the dimensionless coefficients defined in Eqs. (2.5), (2.6), (2.8) and (2.10) in the input file. The notation for the coefficients of the operators that can be set in the input file is listed in Table 2.1, while Table 2.2 summarizes the processes we considered, and which operator can be turned on and off in each process.

	Operator			Operator	
$C_{\varphi W, \varphi B, \varphi WB,}$	CC_ww, CC_bb, CC_wb		$C_{\varphi \tilde{W}, \varphi \tilde{B}, \varphi \tilde{W} B}$	CC_wwt, CC_bbt, CC_wbt	
Γ_W^u	ReGUw_i	$i \in \{$u,c,t$\}$	Γ_γ^u	ReGUe_i	$i \in \{$u,c,t$\}$
	ImGUw_i	$i \in \{$u,c,t$\}$		ImGUe_i	$i \in \{$u,c,t$\}$
Γ_W^d	ReGDw_j	$j \in \{$d,s,b$\}$	Γ_γ^d	ReGDe_j	$j \in \{$d,s,b$\}$
	ImGDw_j	$j \in \{$d,s,b$\}$		ImGDe_j	$j \in \{$d,s,b$\}$
Γ_W^e	ReGEw, ImGEw		Γ_γ^e	ReGEe, ImGEe	
$c_{Q\varphi}^{(1)}$	Qphi1_a	$a \in \{$11,22,33$\}$	$c_{Q\varphi}^{(3)}$	Qphi3_a	$a \in \{$11,22,33$\}$
$c_{U\varphi}$	Uphi_a	$a \in \{$11,22,33$\}$	$c_{D\varphi}$	Dphi_a	$a \in \{$11,22,33$\}$
ξ	ReXi_ij	$i \in \{$u,c,t$\}$			
	ImXi_ij	$j \in \{$d,b,s$\}$			
Y_u'	ReYu_i	$i \in \{$u,c,t$\}$	Y_d'	ReYd_j	$j \in \{$d,s,b$\}$
	ImYu_i	$i \in \{$u,c,t$\}$		ImYd_j	$j \in \{$d,s,b$\}$
$C_{LQ,U}$	QLu_a	$a \in \{$11,22,33$\}$	$C_{LQ,D}$	QLd_a	$a \in \{$11,22,33$\}$
C_{eu}	Ceu_a	$a \in \{$11,22,33$\}$	C_{ed}	Ced_a	$a \in \{$11,22,33$\}$
C_{Lu}	CLu_a	$a \in \{$11,22,33$\}$	C_{Ld}	CLd_a	$a \in \{$11,22,33$\}$
C_{Qe}	Qe_a	$a \in \{$11,22,33$\}$	C_{LedQ}	ReLedQ_a	$a \in \{$11,22,33$\}$
				ImLedQ_a	$a \in \{$11,22,33$\}$
$C_{LeQu}^{(1)}$	ReLeQu_a	$a \in \{$11,22,33$\}$	$C_{LeQu}^{(3)}$	ReLeQu3_a	$a \in \{$11,22,33$\}$
	ImLeQu_a	$a \in \{$11,22,33$\}$		ImLeQu3_a	$a \in \{$11,22,33$\}$

Table 2.1: Notation for the coefficients of the dimension-six operators that can be set in POWHEG. The flavor structures reflect the assumptions discussed in Section 2.2.2.

	$pp \to \ell\nu$	$pp \to \ell^+\ell^-$, $\nu\bar{\nu}$	WH	ZH	VBF
$C_{\varphi W}, C_{\varphi\tilde{W}}$	−	−	✓	✓	✓
$C_{\varphi B}, C_{\varphi\tilde{B}}$	−	−	−	✓	✓
$C_{\varphi WB}, C_{\varphi\tilde{W}\tilde{B}}$	−	−	−	✓	✓
$\Gamma_\gamma^{u,d}$	✓	✓	−	✓	✓
$\Gamma_W^{u,d}$	✓	✓	✓	✓	✓
$\Gamma_{\gamma,W}^e$	✓	✓	×	×	−
$c_{Q\varphi}^{(1,3)}$	✓	✓	✓	✓	✓
$c_{U\varphi}, c_{D\varphi}$	−	✓	−	✓	✓
ξ	✓	−	✓	−	✓
$c_{L\varphi}^{(1,3)}, c_{e\varphi}$	×	×	×	×	−
Y_u', Y_d'	−	−	✓	✓	−
$C_{LQ,U}, C_{LQ,D}$	✓	✓	−	−	−
C_{eu}, C_{ed}	−	✓	−	−	−
$C_{Lu}, C_{Ld,Qe}$	−	✓	−	−	−
$C_{LedQ}, C_{LeQu}^{(1,3)}$	✓	✓	−	−	−

Table 2.2: Contributions of the dimension-six operators in Eqs. (2.5), (2.6), (2.8), (2.9) and (2.10) to NC and CC Drell-Yan, associated production of a Higgs and a weak boson, and Higgs boson production via vector boson fusion. For each process, a ✓ indicates that the contribution has been implemented in POWHEG, a × that the operator contributes at tree level, but has been neglected because of the reasons explained in the text, while a − indicates that the operator does not contribute at leading order.

The new physics scale Λ, at which the coefficients are defined, can be specified by setting the flag `LambdaNP` to the desired value. Eqs. (2.35) and (2.36) are then used to run the coefficients from Λ to μ_R, the renormalization scale of the process of interest. By default, `LambdaNP` = 1 TeV. For the coefficients that do not have QCD evolution, the flag `LambdaNP` is irrelevant.

2.3 Neutral- and charged-current Drell-Yan production

We start by analyzing the contributions of the dimension-six SM-EFT operators to the processes $pp \to \ell^+ \nu_\ell$, $\ell^- \bar{\nu}_\ell$, $\ell^+ \ell^-$ and $\nu \bar{\nu}$. The SM background to these processes is known with very high accuracy, including fixed next-to-next-LO (NNLO) QCD corrections [35, 36, 37] and NLO electroweak (EW) corrections [38, 39, 40, 41, 42]. More recently, the interface of the NNLO predictions with the parton shower has been presented in Refs. [43, 44, 45], and a quantitative assessment of the size of different QCD and EW corrections has been discussed in Ref. [46]. Contributions from SM-EFT operators, at LO in QCD, have been considered, for example, in Refs. [28, 47, 48, 49] and rescaled by the SM NNLO K-factor in Ref. [50, 51]. In this work, we have calculated the NLO QCD corrections to the partonic processes mediated by SM-EFT operators in Table 2.2 and interfaced with the parton shower according to the `POWHEG` method, extending the original work of Ref. [24].

If the invariant mass of the leptons is close to the weak boson masses, NC and CC Drell-Yan production is dominated by the production of a W or Z boson, which subsequently decays into leptons. In this region, these processes are in principle sensitive to modifications of the SM W and Z couplings to quarks, represented by the operators $c_{Q\varphi}^{(1,3)}$, $c_{U\varphi}$ and $c_{D\varphi}$, or to new interactions of the W and Z boson: the W coupling to right-handed quarks, mediated by ξ, and the chiral-symmetry-breaking dipole couplings $\Gamma_{W,\gamma}^{u,d,e}$. For W production, the contributions of $c_{Q\varphi}^{(1,3)}$ amount to a shift in the values of the CKM mixing matrix, which, in the presence of these operators, is no longer unitary. Instead, ξ induces couplings to quarks with opposite chirality to the SM. If one considers observables that are symmetric under the exchange of the charged lepton and the neutrino momenta, the contributions of these operators are identical to those of the SM, making it difficult to obtain strong constraints [52]. The right-handed nature of ξ would manifest, for example, in a larger fraction of right-handed polarized W bosons. Appreciable deviations, however, require large couplings that are already ruled out by other collider and low-energy observables, such as associated production of a W and a Higgs boson [52]. Similarly, in Z production, the cross section induced by the operators $c_{Q\varphi}^{(1,3)}$, $c_{U\varphi}$ and $c_{D\varphi}$ is qualitatively very similar to the SM, and thus other processes, such as $e^+ e^- \to q\bar{q}$ at the Z pole, or $pp \to HZ$, provide stronger bounds. In the case of the dipole couplings $\Gamma_{W,\gamma}^{u,d,e}$, the cross section has a different shape, being enhanced for large values of W boson transverse mass or the dilepton invariant mass. Furthermore, the different chiral structure of the vertex could be identified by looking at the W and Z

boson polarization.

When the dilepton invariant mass is much larger than the W or Z boson mass, NC and CC Drell-Yan production receive important contributions from the four-fermion operators in Eq. (2.10). $C_{LQ,U}$, $C_{LQ,D}$, C_{LedQ} and $C_{LeQu}^{(1,3)}$ contribute to the neutral and charged-current processes, while the remaining operators in Eq. (2.10) only contribute to neutral currents. Most of the semi-leptonic interactions, namely $C_{LQ,U}$, $C_{LQ,D}$, C_{eu}, C_{ed}, C_{Lu}, C_{Ld} and C_{Qe}, couple left- and right-handed quarks to left- or right-handed leptons, and therefore modify the helicity structures which already exist in the SM. On the other hand, C_{LedQ} and $C_{LeQu}^{(1)}$ are scalar couplings, while $C_{LeQu}^{(3)}$ has the form of a tensor coupling, all of which give rise to new helicity structures.

We computed the W and Z production cross sections in the presence of the dimension-six operators in Table 2.2, including NLO QCD corrections, and implemented them in the `POWHEG BOX V2`. The cross section has the schematic structure

$$\sigma = \sigma_{\text{SM}} + \sum_i \sigma_i C_i + \sum_{ij} \sigma_{ij} C_i C_j, \qquad (2.37)$$

where σ indicates a generic (differential) cross section in the $\ell\nu$, $\ell^+\ell^-$ or $\nu\bar{\nu}$ channels. If one neglects light-quark mass effects, only the semileptonic four-fermion operator $C_{LQ,U}$ and $C_{LQ,D}$ and the vertex correction $c_{Q\varphi}^{(1,3)}$ interfere with the SM amplitude for $pp \to \ell\nu$, due to helicity considerations. In the case of Z production, the index i in the interference term in Eq. (2.37) runs over the operators

$$\{c_{Q\varphi}^{(1,3)}, c_{U\varphi}, c_{D\varphi}, C_{LQ,U}, C_{LQ,D}, C_{eu}, C_{ed}, C_{Lu}, C_{Ld}, C_{Qe}\}.$$

We included dimension-eight effects to guarantee the positivity of the cross section even for arbitrary large values of the couplings. For completeness, we also included interferences between different dimension-six operators. The chiral structures of the effective operators strongly limit the number of such interference terms and in practice one needs only to consider the interference of the photon and Z dipoles in $pp \to \ell^+\ell^-$, and of the u-type scalar and tensor operators, $C_{LeQu}^{(1,3)}$, in $pp \to \ell^+\ell^-$ and $pp \to \ell\nu_\ell$.

When extracting bounds on the coefficients of effective operators, one should make sure to be working in the regime of validity of the EFT. For the operators that interfere with the SM one can check that the bounds are not dominated by terms quadratic in the new physics couplings. For a clear discussion of this point, we refer to Refs. [53, 48]. For operators with different chiral structures than the SM, the leading contribution to the W and Z production cross sections is quadratic in the BSM coupling, and goes as Λ^{-4}. One might then worry that the constraints on these operators are not reliable because of missing Λ^{-4} contributions from the interference of genuine dimension-eight operators with the SM. This concern is justified for bounds obtained from the total cross section, or from differential distributions that are not sensitive to the quark/lepton chiralities. However, dimension-six operators with different chiral structures than the SM leave clear signatures in observables such as the W and Z polarization fractions, that cannot be mimicked by dimension-eight operators. Thus,
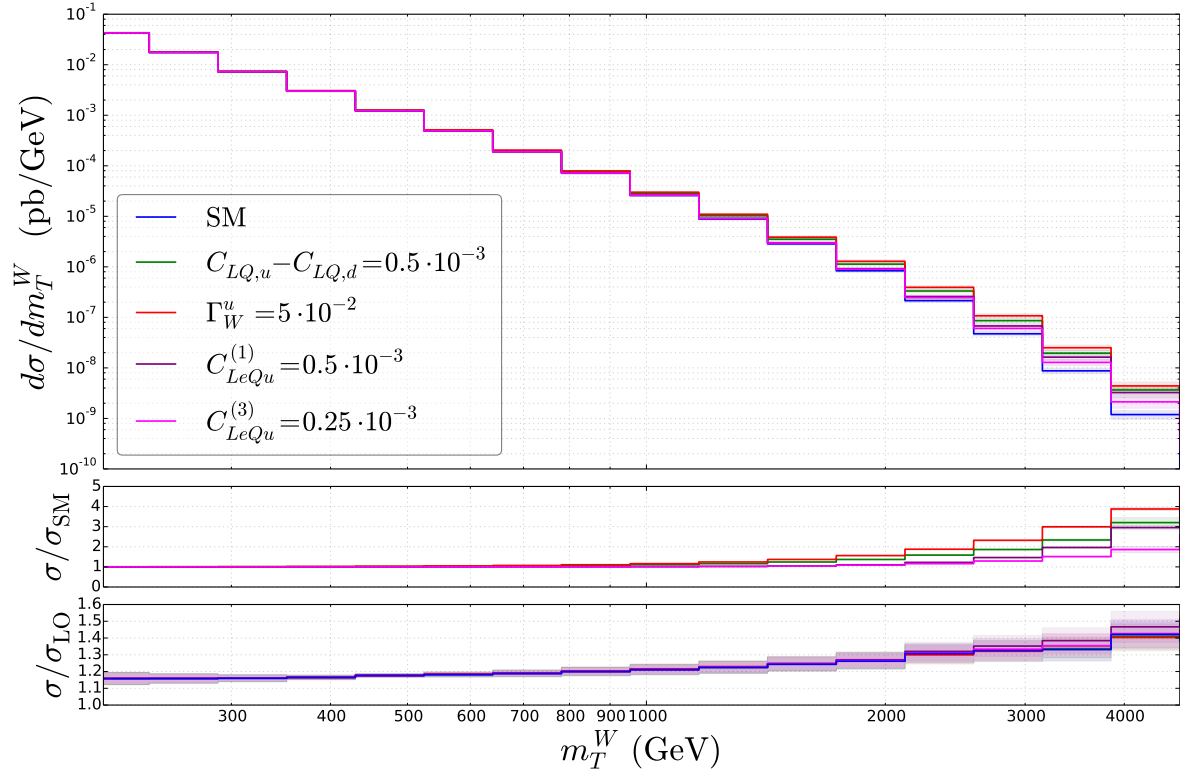
Figure 2.1: Differential $pp \rightarrow e^+\nu_e + e^-\bar{\nu}_e$ cross section as a function of m_T^W, at $\sqrt{S} = 13$ TeV. The middle panel shows the ratio of the differential cross sections in the presence of dimension-six operators and in the SM, while the bottom panel the ratio of the NLO and LO cross sections. The shaded regions indicate the theoretical uncertainties from PDF and scale variations.

in the presence of deviations from the SM, it will be possible to disentangle dimension-six operators with different chiral structure than the SM from genuine dimension-eight effects by studying more differential observables.

We show the resulting $pp \rightarrow e^+\nu_e + e^-\bar{\nu}_e$ cross section at $\sqrt{S} = 13$ TeV as a function of the W transverse mass, m_T^W, in Fig. 2.1, where m_T^W is defined as

$$m_T^W = \sqrt{2|p_T^\ell||p_T^\nu|(1 - \cos \Delta\phi_{\ell\nu})}. \tag{2.38}$$

Here p_T^ℓ and p_T^ν are the charged-lepton and the neutrino transverse momenta, respectively, and $\Delta\phi_{\ell\nu}$ is their azimuthal separation. In blue we depict the SM cross section, while the remaining lines depict the contributions of the four-quark operators $C_{LQ,u} - C_{LQ,d}$ (green), $C_{LeQu}^{(1)}$ (purple) and $C_{LeQu}^{(3)}$ (magenta), and of the dipole operator Γ_W^u (red). The values of the coefficients have been chosen to be close to the bounds discussed in Section 2.3.1. The down-
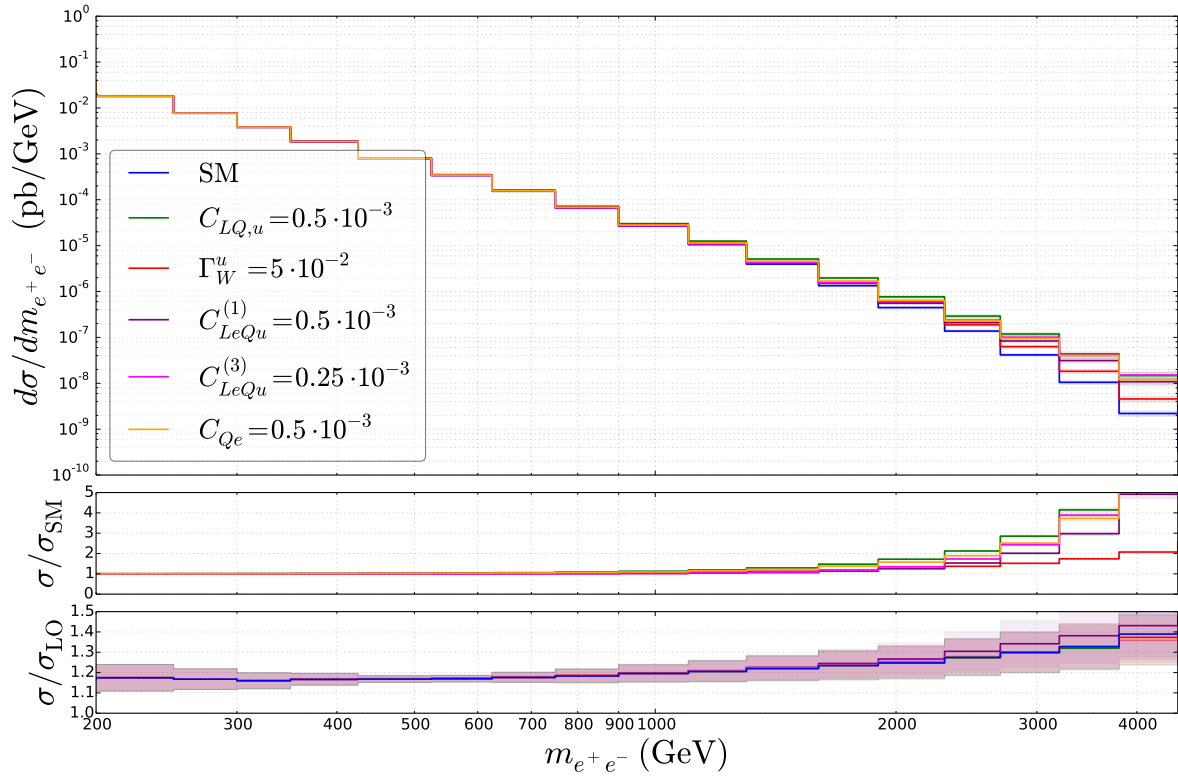
Figure 2.2: Differential $pp \to e^+e^-$ cross section as a function of the dilepton invariant mass, at $\sqrt{S} = 13$ TeV. The shaded regions indicate the theoretical uncertainties from PDF and scale variations.

type and electron-type dipoles Γ_W^d, Γ_W^e, and d-type scalar operator C_{LedQ} induce corrections with the same m_T^W dependence as Γ_W^u and $C_{LeQu}^{(1)}$, respectively.

In Fig 2.2 we show $pp \to e^+e^-$, as a function of the dilepton invariant mass. In addition to the operators shown in Fig. 2.1, we also included the coupling of left-handed quarks to right-handed leptons, C_{Qe}, which does not contribute to $pp \to \ell\nu$. The photon dipole Γ_γ^u gives a correction to the cross section, which is roughly 70% of the weak dipole at large $m_{e^+e^-}$. The remaining u-type couplings, C_{eu} and C_{Lu}, give rise to corrections to the cross sections that have similar shape as $C_{LQ,u}$ and C_{Qe}. Not shown in the figure are d-type couplings, Γ_W^d, Γ_γ^d, $C_{LQ,d}$, C_{ed}, C_{Ld}, C_{LedQ}, which are qualitatively very similar to the corresponding u-type operators, with some suppression from the d-quark PDF.

The cross sections were evaluated using the `PDF4LHC15_nlo_30` PDF set [54], with the factorization and renormalization scales set to $\mu_F = \mu_R = m_{\ell\ell'}$, where $m_{\ell\ell'}$ is the invariant mass of the charged lepton and the neutrino, or of the two charged leptons. The running of the coefficients from the initial scale $\mu_0 = 1$ TeV to μ_R is taken into account by solving Eq. (2.35). The error bands in Figs. 2.1 and 2.2 include the 7−point scale variations, by independently varying μ_F and μ_R between $m_{\ell\ell'}/2$ and $2m_{\ell\ell'}$ excluding the extremes, and

PDF variations, computed with the 30 members of the `PDF4LHC15_nlo_30` PDF set.

For both W and Z production, the uncertainties of the NLO SM cross section are about 2-3% at low m_T^W or $m_{e^+e^-}$, and increase to about 10% at $m_T^W, m_{e^+e^-} \sim 1-2$ TeV, where they are dominated by PDF uncertainties. We find that the cross sections induced by the dimension-six operators that couple to the light quarks are affected by similar errors. In particular, the PDF uncertainties for both the SM and the dimension-six cross sections dominate at large m_T^W or $m_{e^+e^-}$, where they are about 10-15%. The scale variations for operators with a similar chiral structure as the SM, such as $C_{L,Qu}$ or C_{Qe}, as well as the dipole operators and the semileptonic tensor operators are all very similar, being at most around 5%. The scalar operators C_{LedQ} and $C_{LeQu}^{(1)}$, on the other hand, have larger scale uncertainties, close to 10% at high invariant mass.

The cross section induced by the four-fermion and dipole operators, as a function of m_T^W or $m_{l^+l^-}$, falls more slowly than in the SM, and thus the effects are more visible for large invariant mass. This is evident from the middle panels of Figs. 2.1 and 2.2, which show the ratio of the differential cross sections in the presence of dimension-six operators and in the SM. For the four-fermion operators that interfere with the SM, namely $C_{LQ,u}$, $C_{LQ,d}$, C_{eu}, C_{ed}, C_{Lu}, C_{Ld} and C_{Qe}, the ratio scales as $(m_T^W/v)^2$ or $(m_{l^+l^-}/v)^2$, whenever the interference term dominates. The dipole operators $\Gamma_{W,\gamma}^{u,d,e}$ do not interfere with the SM, and contribute at dimension-eight. In this case, the amplitude contains a W/Z propagator, but it has an additional factor of momentum with respect to the SM, so that the squared amplitude is also enhanced by a factor of $(m_T^W/v)^2$. Finally, the scalar and tensor operators, $C_{LeQu}^{(1,3)}$ and C_{LedQ}, do not interfere with the SM and lack the W/Z boson propagator, causing the ratio in the middle panel of Figs. 2.1 and 2.2 to scale as $(m_T^W/v)^4$ and $(m_{\ell^+\ell^-}/v)^4$ at high vector boson transverse or invariant mass.

The bottom panels of Figs. 2.1 and 2.2 show the ratio of the NLO and LO Drell-Yan cross sections. We see that for both the SM and the dimension-six operators the importance of the NLO corrections increases at high m_T^W or $m_{\ell^+\ell^-}$, being around 30%-40% in the highest bins. Most dimension-six operators exhibit a behavior similar to the SM, with the scalar semileptonic operators C_{LedQ} and $C_{LeQu}^{(1)}$ receiving the largest NLO corrections. Since the contribution of dimension-six operators is particularly relevant at high invariant mass, the bottom panel of Fig. 2.1 and 2.2 highlights the importance of including NLO QCD corrections[1].

2.3.1 Bounds on effective operators

We can take advantage of the enhancement at high m_T^W and $m_{\ell^+\ell^-}$ by interpreting the ATLAS and CMS searches for new high-mass phenomena in the dilepton or lepton and missing energy final states [55, 56, 57, 58, 59, 60, 61, 2, 1] as bounds on the coefficients of the effective operators. As an example of the kind of constraints one can obtain, we consider

---

[1]In the same high invariant mass region, higher-order EW corrections also become sizable and need to be taken into account for accurate predictions.

the analyses of Refs. [1] and [2], which used data collected by the ATLAS collaboration during the LHC Run II at 13 TeV, with integrated luminosity of 36.1 fb^{-1}. We calculated the $pp \to e^+ \nu_e$, $pp \to e^- \bar{\nu}_e$ and $pp \to e^+ e^-$ differential cross sections, interfacing to Pythia8 .219 [62, 63] parton shower and hadronization, using the POWHEG method. We used the same binning as the ATLAS collaboration, which considers 7 bins in m_T^W, between 130 GeV and 7 TeV [1], and 10 bins in $m_{e^+e^-}$, from m_Z up to 6 TeV [2]. We applied the same cuts as the experimental collaboration on the leptons and missing energy, but did not perform a detailed detector simulation to determine acceptance and efficiency. In addition, we did not simulate additional SM backgrounds, such as $t\bar{t}$ and diboson production, but used the expected background events listed in Refs. [1] and [2]. For these reasons our bounds have to be interpreted as a crude estimate of the reach of the LHC.

The resulting 90% confidence limits are shown in Table 2.3. We turn on all operators at the new physics scale $\mu_0 = 1$ TeV, assuming that only the couplings to the first generation of quarks are non-zero, and use the electron channels of Refs. [1] and [2], thus constraining the electron component of four-fermion operators. The muon component can be analyzed in a similar fashion. The bounds in the first column of Table 2.3 are extracted using a LO calculation of the correction to the cross section from dimension-six operators, while those on the second column include NLO QCD corrections. We show the limits in two cases. The first bound in each column includes all the bins of Refs. [1] and [2]. In this case, the limits are dominated by the last bin in m_T^W, $m_T^W \in [3, 7]$ TeV, and $m_{e^+e^-}$, $m_{e^+e^-} \in [3, 6]$ TeV. The second bound excludes the highest bin, probing m_T^W and $m_{e^+e^-}$ up to 3 TeV.

From Table 2.3, one can see that the processes considered in this section are not very sensitive to the dipole couplings $\Gamma_{W,\gamma}^{u,d}$. These coefficients are constrained at the 10% level. If we translate these bounds to an estimate of the new physics scale Λ, using $\Gamma_{W,\gamma}^{u,d} \equiv v^2/\Lambda^2$, we see that the effective scale would be $\lesssim 1$ TeV. This is smaller than the scales directly accessed by the experiment, implying the EFT framework might not be applicable in this region and the resulting limits should be interpreted with some caution. On the other hand, the semileptonic four-fermion operators are strongly constrained, in several cases at better than the permil level, corresponding to $\Lambda \sim 10$ TeV. For scalar and tensor operators, the strong bounds suggest that the last two bins are in the regime of validity of the EFT, $\Lambda \gg m_T^W$, $m_{e^+e^-}$. For the remaining operators we checked that for the values of the couplings in Table 2.3 the interference term, linear in v^2/Λ^2, is larger than the quadratic piece.

Comparing the first and second column of Table 2.3 we see that including NLO QCD corrections impacts the coefficients of dimension-six operators at the 10% - 20% level. As expected from Figs. 2.1 and 2.2, the effect is larger for the analysis that uses all bins of Refs. [1] and [2], which is dominated by the bin of highest invariant mass, and the scalar operators C_{LedQ} and $C_{LeQu}^{(1)}$ are the most affected by NLO corrections.

It is interesting to compare the constraints of Table 2.3 with complementary constraints that can be extracted from low-energy observables. First, we point out that the imaginary parts of several operators can be stringently constrained by electric-dipole-moment (EDM) measurements. For example, the imaginary parts of $C_{LeQu,LedQ}^{(1)}$ and $C_{LeQu}^{(3)}$ are probed by

	LO $\times 10^{-4}$		NLO $\times 10^{-4}$		Λ (TeV)	
$\left\|\Gamma_W^u\right\|$	< 480	< 710	< 460	< 640	1.1	0.9
$\left\|\Gamma_\gamma^u\right\|$	< 1200	< 1900	< 1200	< 1900	0.7	0.6
$\left\|\Gamma_W^d\right\|$	< 510	< 730	< 470	< 650	1.1	1.0
$\left\|\Gamma_\gamma^d\right\|$	< 1900	< 2700	< 1800	< 2600	0.6	0.5
$\left\|C_{LedQ}\right\|$	< 6.9	< 12	< 5.7	< 10	10	7.7
$\left\|C_{LeQu}^{(1)}\right\|$	< 4.6	< 10	< 3.9	< 8	12	8.7
$\left\|C_{LeQu}^{(3)}\right\|$	< 1.8	< 4.4	< 1.6	< 4	19	12
$C_{LQ,u}$	$[-7.4, 1.4]$	$[-16, 3.8]$	$[-6.9, 1.2]$	$[-14, 3.0]$	9.3	6.6
$C_{LQ,d}$	$[-7.1, 11]$	$[-14, 20]$	$[-6.9, 9.5]$	$[-13, 17]$	8.0	6.0
$C_{e,u}$	$[-6.9, 3.4]$	$[-16, 8.7]$	$[-6.4, 3.1]$	$[-14, 7.7]$	9.7	6.6
$C_{e,d}$	$[-8.9, 10]$	$[-17, 20]$	$[-8.1, 9.1]$	$[-15, 17]$	8.1	5.9
$C_{L,u}$	$[-6.0, 4.5]$	$[-14, 11]$	$[-5.5, 4.0]$	$[-12, 10]$	10	7.1
$C_{L,d}$	$[-9.0, 9.9]$	$[-18, 19]$	$[-8.4, 8.5]$	$[-15, 16]$	7.8	6.1
$C_{Q,e}$	$[-5.0, 4.0]$	$[-11, 10]$	$[-4.8, 3.4]$	$[-9.6, 8.6]$	11	8.2

Table 2.3: 90% CL bounds on the coefficients of SM-EFT operators that contribute to CC and NC Drell-Yan production, and the corresponding estimates of the scale Λ, assuming $C_i \equiv v^2/\Lambda^2$. The bounds on the first and second columns use, respectively, SM-EFT cross sections at LO and NLO in QCD. Λ is extracted from the NLO bounds, and, for asymmetric limits, the weaker limit is used. The bounds are obtained by turning on all operators at the scale $\mu_0 = 1$ TeV, but with the assumptions that only the couplings to the u and d quarks are non-zero. In each column, the first bound uses all the bins in Refs. [1] and [2], corresponding to a maximum m_T^W and $m_{e^+e^-}$ of $(m_T^W)_{max} = [3, 7]$ TeV and $(m_{e^+e^-})_{max} = [3, 6]$ TeV, while the second bound excludes the last bin, corresponding to $(m_T^W)_{max} = [2, 3]$ TeV and $(m_{e^+e^-})_{max} = [1.8, 3]$ TeV.

measurements of T-violation in paramagnetic systems and in diamagnetic atoms, respectively. Below the QCD scale, the scalar and tensor couplings induce spin-independent and spin-dependent electron-nucleon interactions, often referred to as $\tilde{C}_S$ and $\tilde{C}_T$, respectively [64, 65, 66]. The scalar coupling is most sensitively probed in measurements of T-violation in ThO, while the EDM of ^{199}Hg is sensitive to $\tilde{C}_T$. The current experimental constraints [67, 68] roughly imply $Im\, C_{LeQu, LedQ}^{(1)} \lesssim 10^{-9}$ and $Im\, C_{LeQu}^{(3)} \lesssim 10^{-10}$. Similarly, the imaginary parts of the dipole couplings also induce EDMs at low energies. The resulting limits are especially stringent for the couplings to the photon, $\Gamma_\gamma^{u,d}$, which directly contribute to the neutron EDM [69, 70]. Instead, the $\Gamma_W^{u,d}$ couplings induce the neutron EDM at the one-loop level [20]. The current experimental constraints [71, 67, 72] give $Im\, \Gamma_W^{u,d} \lesssim 10^{-6}$ and $Im\, \Gamma_\gamma^{u,d} \lesssim 10^{-9}$.

The low-energy constraints that can be set on the real parts of the couplings are weaker, and comparable to the direct limits in Table 2.3. Focusing on the four-fermion operators $C_{LeQu}^{(1,3)}$ and C_{LedQ}, we can map them into the scalar, pseudoscalar, and tensor couplings introduced in Refs. [28, 73], $\epsilon_S^* = C_{LeQu}^{(1)} + C_{LedQ}$, $\epsilon_P^* = C_{LeQu}^{(1)} - C_{LedQ}$ and $\epsilon_T^* = C_{LeQu}^{(3)}$. The pseudoscalar coupling ϵ_P is strongly bound by the leptonic decay of the pion, and, in particular, by the ratio $\Gamma(\pi \to e\nu)/\Gamma(\pi \to \mu\nu)$, which is suppressed by m_e^2/m_μ^2 in the SM. ϵ_S is constrained by superallowed β decays [74], while the tensor coupling ϵ_T affects radiative pion decays, such as $\pi \to e\nu\gamma$ and the neutron decay parameters [75, 28, 73]. The analysis of Refs. [75, 28, 73, 76] shows that the bounds on the pseudoscalar coupling are at the level $|\epsilon_P| \lesssim 5 \cdot 10^{-4}$, while for the scalar and tensor $|\epsilon_{T,S}| \lesssim 10^{-3}$, thus making collider observables very competitive with low-energy probes for the real parts of these couplings.

2.3.2 Disentangling dimension-six operators

In light of the comparable sensitivities of low- and high-energy observables, it is very important to construct collider observables that, in the presence of deviations from the SM, are able to differentiate between the various dimension-six operators. Examples are angular distributions. For $pp \to \ell\nu_\ell$ we work in the W helicity frame, that is the frame in which the $\ell\nu_\ell$ system is at rest, with the z-axis chosen to be in the direction of the sum of the momenta of the charged lepton and neutrino in the laboratory frame. We consider the differential distribution with respect to $\cos\theta^*$, where θ^* is the polar angle of the charged lepton in this frame. When the charged lepton and the neutrino emerge from the decay of a W boson, the differential $\cos\theta^*$ distribution is related to the W boson polarization fractions, F_0, F_L, and F_R [77, 78]. We can write the differential distribution as

$$\frac{1}{\sigma}\frac{d\sigma}{d\cos\theta^*} = \frac{3}{8}\left[1 + \cos^2\theta^* + \frac{A_0}{2}(1 - 3\cos^2\theta^*) + A_4\cos\theta^* + \ldots\right], \qquad (2.39)$$

where the dots denote higher powers of $\cos\theta^*$, which can arise if the $\ell\nu_\ell$ system has total angular momentum $J > 1$. σ denotes any differential cross section that does not depend on the kinematics of individual leptons. If the process is mediated by a W boson, the W
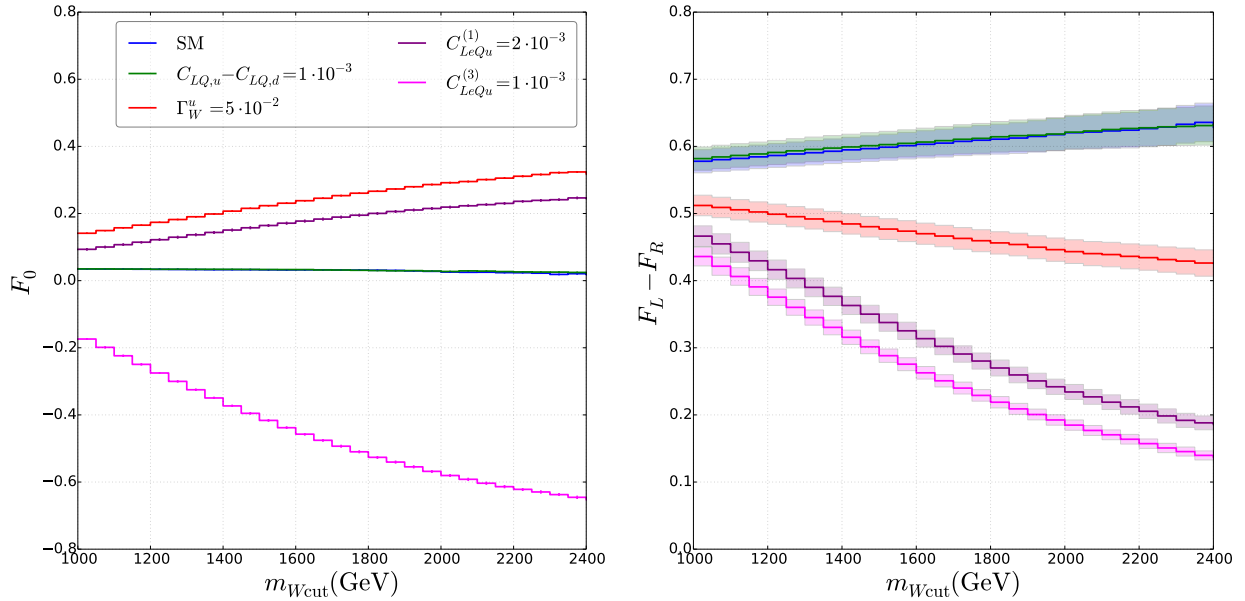
Figure 2.3: Polarization fractions F_0 and $F_L - F_R$ in $pp \to e^+\nu_e$, for $m_W > m_{W\,cut}$, where m_W denotes the invariant mass of the neutrino and charged lepton, at $\sqrt{S} = 13$ TeV. The shaded regions indicate the uncertainties from PDF and scale variations.

polarization fractions are given by

$$F_0 = \frac{A_0}{2}, \qquad F_L = \frac{1}{4}(2 - A_0 \mp A_4), \qquad F_R = \frac{1}{4}(2 - A_0 \pm A_4), \qquad (2.40)$$

for $W^\pm$, respectively. For electron-neutrino invariant mass far from the W mass, we take Eq. (2.40) as the definition of $F_{0,L,R}$.

In Fig. 2.3 we show the values of F_0 and $F_L - F_R = -A_4/2$, for $m_W > m_{W\,cut}$, where m_W denotes the invariant mass of the lepton and the neutrino. The error bands include scale and PDF variations. For illustration sake, we chose larger coefficients compared to Figs. 2.1 and 2.2, but we stress that even for values closer to the limits discussed in Section 2.3.1 the effect on $F_{0,L,R}$ is significant. In the SM, for small values of p_T^W, $A_0 \sim 0$ and A_4 is negative, reflecting the fact that the W boson is mostly produced with left-handed polarization [77]. The values of A_0 and A_4 are not modified by the operators $C_{LQ,u}$ and $C_{LQ,d}$, which have the same chiral structure as the SM, and couple left-handed quark to left-handed lepton fields. On the other hand, the dipole operators, and the scalar and tensor four-fermion operators have a different chiral structure. In the case of the dipoles, the interaction of the W to the quarks flips chirality. As a result the W boson is mostly produced with longitudinal polarization, and, if the dipole operators dominate the cross section, F_0 approaches 1, while A_4 should go to zero. This can explicitly be seen from the tree-level amplitude, that goes as $\sin^2\theta^*$. Indeed Fig. 2.3 shows that, in the presence of a non-vanishing Γ_W^u, as the W invariant mass grows and the contribution of Γ_W^u becomes more important, F_0 increases and
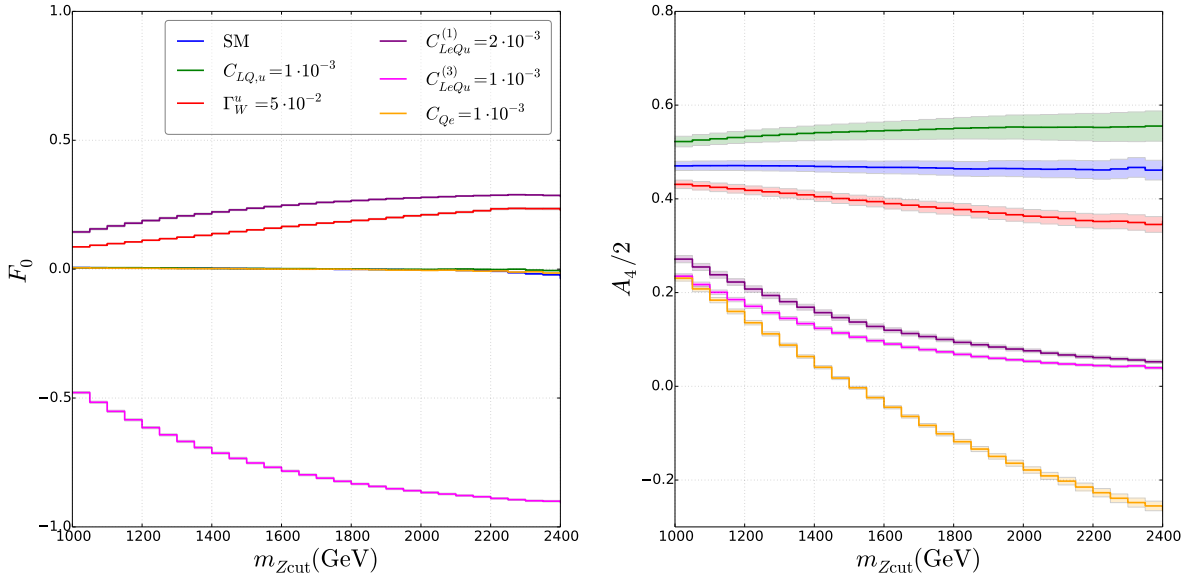
Figure 2.4: Longitudinal polarization F_0 and angular coefficient A_4 in $pp \to e^+e^-$ for $m_Z > m_{Z\,\mathrm{cut}}$, where m_Z denotes the dilepton invariant mass, at $\sqrt{S} = 13$ TeV. The shaded regions indicate the uncertainties from PDF and scale variations.

$F_L - F_R$ decreases. Since, for $\Gamma_W^u = 0.05$, the total cross section is at most 50% larger than in the SM, the polarization fractions shown in Fig. 2.3 do not reach the values expected when the dipole couplings dominate. The cross section induced by a scalar interaction, such as $C_{LeQu}^{(1)}$ and C_{LedQ}, is, at LO, independent of $\cos\theta^*$. In this case, when the cross section is dominated by the scalar contribution, $F_L - F_R$ goes to zero and $F_0 \sim 1/3$, which is in agreement with Fig. 2.3. Finally, for tensor interactions, the tree-level cross section goes as $\cos^2\theta^*$, suggesting that $F_0 \sim -1$ and $A_4 \sim 0$, which is once again confirmed by Fig. 2.3.

While measurement of angular distributions in the W rest frame are experimentally challenging, because of the incomplete knowledge of the neutrino momentum, we hope that the discriminating power shown in Fig. 2.3 motivates the study of variables correlated with $\cos\theta^*$ and m_W [79], which might reveal similar information.

For Z production, we work in the Collins-Soper frame [80] and show F_0 and A_4 as a function of a cut on the leptons invariant mass in Fig. 2.4. In the SM F_0 is very close to zero, and does not significantly depend on the Z invariant mass. A_4 is also close to zero at the Z peak, and its dependence on m_Z is determined by Z/γ^* interference. As the dilepton invariant mass grows, the SM cross section becomes dominated by the coupling to the $SU(2)_L$ gauge boson, resulting in a larger A_4. $C_{LQ,u}$ and $C_{LQ,d}$ do not change this picture, while new dipole, scalar, and tensor operators would dramatically change the value of F_0 and A_4, in the same way as in W production. The operator C_{Qe}, which induces new couplings of left-handed quarks to right-handed leptons, does not change the longitudinal polarization, but, when it becomes dominant with respect to the SM, causes A_4 to flip sign. Additional information

can be extracted from the remaining angular coefficients, which encode the dependence on the azimuthal angle ϕ^*. This brief discussion shows that angular distributions can play a very important role in understanding the origin of new physics, were a deviation from the SM to be observed.

Finally, we note that it is straightforward to include the contributions of gauge-invariant dimension-six operators involving light sterile neutrinos ν_R [28], or lepton-number violating (LNV) dimension-seven operators [81, 82, 83]. For example, in the presence of ν_R it is possible to construct two more scalar ($\mathcal{O}_{qu\nu}$ and $\mathcal{O}'_{lq}$ in the notation of Ref. [28]) and one more tensor operator ($\mathcal{O}'_{lq}$). It is easy to see that, for charged-current processes, $\mathcal{O}_{qu\nu}$, $\mathcal{O}'_{lq}$ and $\mathcal{O}'_{lq}$ give rise to corrections to the squared amplitude that are identical to those of $\mathcal{O}_{LedQ}$, $\mathcal{O}^{(1)}_{LeQu}$ and $\mathcal{O}^{(3)}_{LeQu}$, respectively. Thus, were the cross section of Fig. 2.1 and the angular distributions of Fig. 2.3 to show evidence of scalar or tensor operators, the effect can be attributed to non-standard operators with either left- or right-handed neutrinos (or even to LNV charged-current scalar and tensor operators). In the first case, however, one would expect to see a correlated deviation in $pp \to \ell^+\ell^-$. On the other hand, if the scalar or tensor operators involve ν_R, or are LNV, $SU(2)_L$ gauge-invariance relates the corrections to $pp \to \ell\nu_\ell$ to $pp \to \nu\bar{\nu}$, while $pp \to \ell^+\ell^-$ is unaffected.

2.4 Associated production of a Higgs boson and a W or Z boson

Associated production of a Higgs boson and a W or Z boson is the third most important Higgs boson production mechanism at the LHC. Theoretical predictions for the SM background are available at NNLO in QCD [84, 85, 86, 87] and are matched to the parton shower up to the NNLO+PS level [88]. Contributions from sets of SM-EFT operators, including NLO QCD corrections, have been studied in Refs. [89, 90, 91, 92, 93]. Refs. [89, 90, 91, 92] focused on couplings to the gauge bosons, such as $C_{\varphi W}$, $C_{\varphi B}$ and $C_{\varphi WB}$. Ref. [93] included also the quark operators $c^{(1,3)}_{Q\varphi}$, $c_{U\varphi}$ and $c_{D\varphi}$, with the well-motivated flavor assumptions of universal couplings to the first two generations. Compared to Ref. [93], the SM-EFT operators of Table 2.2 include the right-handed current operator ξ, the Yukawa couplings $Y'_{u,d}$ and the dipole operators $\Gamma^{u,d}_{W,\gamma}$. In addition, we adopt the less restrictive flavor assumptions, discussed in Section 2.2, for $c^{(1,3)}_{Q\varphi}$, $c_{U\varphi}$ and $c_{D\varphi}$. For all the operators in Table 2.2 we include NLO QCD corrections, and interface with the parton shower, building upon the original NLO+PS `POWHEG BOX` code in Ref. [26].

WH and ZH are very sensitive to the modifications of the W and Z boson couplings to quarks, written in a gauge invariant way in Eq. (2.8). These operators require two scalar fields, which induce local quark-Higgs-gauge boson interactions that lead to a significant enhancement of the cross section. Other operators that enter these processes are the dipole operators, since once again $SU(2)_L$-invariance forces the presence of the Higgs field, and

Single coupling				Marginalized			
$C_{\varphi W}$	[-0.20,0.02]	$C_{\varphi \tilde{W}}$	[-0.09,0.09]	$C_{\varphi W}$	[-0.19,0.03]	$C_{\varphi \tilde{W}}$	[-0.15,0.15]
$C_{\varphi B}$	[-0.28,0.15]	$C_{\varphi \tilde{B}}$	[-0.26,0.26]	$C_{\varphi B}$	[-0.06,0.01]	$C_{\varphi \tilde{B}}$	[-0.05,0.05]
$C_{\varphi WB}$	[-0.42,0.07]	$C_{\varphi \tilde{W}B}$	[-0.24,0.24]	$C_{\varphi WB}$	[-0.22,0.03]	$C_{\varphi \tilde{W}B}$	[-0.18,0.18]
Γ^u_W	[-0.05,0.05]	Γ^d_W	[-0.06,0.06]	Γ^u_W	[-0.13,0.13]	Γ^d_W	[-0.13,0.13]
$c^{(1)}_{Q\varphi}$	[-0.04,0.03]	$c^{(3)}_{Q\varphi}$	[-0.01,0.07]	$c^{(1)}_{Q\varphi}$	[-0.06,0.07]	$c^{(3)}_{Q\varphi}$	[-0.03,0.10]
$c_{U\varphi}$	[-0.03,0.05]	$c_{D\varphi}$	[-0.06,0.05]	$c_{U\varphi}$	[-0.06,0.09]	$c_{D\varphi}$	[-0.11,0.09]
Y'_u	[-0.04,0.04]	Y'_d	[-0.04,0.04]	Y'_u	[-0.08,0.08]	Y'_d	[-0.08,0.08]
ξ	[-0.04,0.04]			ξ	[-0.06,0.06]		

Table 2.4: 90% CL level bounds on the coefficients of effective operators that contribute to WH and ZH production. For operators involving quarks, we turned on couplings to the u and d quark. The table on the left shows the bounds obtained assuming that a single operator is turned on at a scale $\Lambda = 1$ TeV. On the right, marginalized bounds, from WH and ZH production and Higgs boson decays to $\gamma\gamma$, γZ, WW^* and ZZ^*.

operators of the form $\varphi^\dagger \varphi X^{\mu\nu} X_{\mu\nu}$ and $\varphi^\dagger \varphi X^{\mu\nu} \tilde{X}_{\mu\nu}$. The contributions of these three classes of operators to the cross section are greatly enhanced at large p_T of the Higgs boson or when the Higgs-weak boson invariant mass is large. WH and ZH production also receive tree-level corrections from the non-standard Yukawa couplings $Y'_{u,d}$. Even though these couplings are effectively dimension-four, they induce a correction to the cross section that is not proportional to the mass of the vector boson, and thus is also enhanced by $p_T^2/m^2_{W,Z}$ at large p_T.

We can appreciate the sensitivity of WH and ZH production to non-standard quark and gauge boson couplings by considering the WH and ZH signal strengths, defined as

$$\mu_{WH} = \frac{\sigma_{W^+H} + \sigma_{W^-H}}{\sigma^{SM}_{W^+H} + \sigma^{SM}_{W^-H}}, \qquad \mu_{ZH} = \frac{\sigma_{ZH}}{\sigma^{SM}_{ZH}}. \tag{2.41}$$

We computed the signal strength at $\sqrt{S} = 8$ TeV using the `PDF4LHC15_nlo_30` PDF sets [54], and extracted bounds using the combined results from the ATLAS and CMS collaborations [94]

$$\mu_{WH}(8\text{TeV}) = 0.89^{+0.40}_{-0.38}, \qquad \mu_{ZH}(8\text{TeV}) = 0.79^{+0.38}_{-0.36}. \tag{2.42}$$

We estimated the scale uncertainties on the signal strength by varying the renormalization and factorization scales μ_F and μ_R between $(m_V+m_H)/2$ and $2(m_V+m_H)$, where m_V denotes the mass of the vector boson. The PDF uncertainties were estimated by evaluating the cross section using the 30 members of the `PDF4LHC15_nlo_30` PDF sets. For the operators we

considered, the theoretical uncertainties are approximately 10%. These uncertainties were taken into account in the extraction of the constraints by following the Rfit approach [95].

The left panel in Table 2.4 shows the 90% CL bounds on the coefficients on effective operators that contribute to WH and ZH production, under the assumption that only one operator is turned on at the new physics scale $\Lambda = 1$ TeV. For simplicity we assumed that only the couplings to the u and d quark are affected. We see that the 8 TeV data, despite the large uncertainties, constrain non-standard couplings to light quarks at the 10% level or better. The only exceptions are the photon dipole operators $\Gamma_\gamma^{u,d}$, which give a small contribution to ZH and are better constrained by NC Drell-Yan production. Constraints on the couplings to gauge bosons $C_{\varphi W}$, $C_{\varphi B}$ and $C_{\varphi WB}$, and their CP-odd counterparts, $C_{\varphi \tilde{W}}$, $C_{\varphi \tilde{B}}$ and $C_{\varphi \tilde{W} B}$, are also weaker, ranging from 10% to 40%.

If we simultaneously turn on all the operators, the limits on the quark operators $c_{Q\varphi}^{(1,3)}$, $c_{U\varphi}$, $c_{D\varphi}$, ξ, $Y'_{u,d}$ and $\Gamma_W^{u,d}$ are weakened by a factor of 2. The bounds on the gauge operators, in particular $C_{\varphi B}$ and $C_{\varphi WB}$, are more affected, becoming significantly weaker. On the other hand, these operators give tree level corrections to the Higgs boson decays, both to $h \to WW^*$ and $h \to ZZ^*$ as well as $h \to \gamma\gamma$ and $h \to \gamma Z$. Since the former two decays are generated at tree level in the SM while the latter two are loop-suppressed, the gauge operators are relatively more important for $h \to \gamma\gamma$ and $h \to \gamma Z$.

In the right panel of Table 2.4 we show the limits on the coefficients of dimension-six operators from WH, ZH, and the Higgs boson branching ratios, obtained under the assumption that all couplings are present at the scale of new physics. We used the combined Run-I ATLAS and CMS results for $\mu_{h\to\gamma\gamma}$, $\mu_{h\to WW^*}$ and $\mu_{h\to ZZ^*}$ [94], and the ATLAS bound on $\mu_{h\to\gamma Z}$ [96]

$$\mu_{h\to\gamma\gamma} = 1.14^{+0.19}_{-0.18}, \qquad \mu_{h\to WW^*} = 1.09^{+0.18}_{-0.16} \qquad \mu_{h\to ZZ^*} = 1.29^{+0.26}_{-0.23} \qquad \mu_{h\to\gamma Z} < 6.6.$$
(2.43)

We see that the Higgs boson branching ratios provide better constraints on $C_{\varphi B(\tilde{B})}$ and $C_{\varphi WB(\tilde{W}B)}$, while they have no significant effect on the remaining operators, for which the WH and ZH cross sections are more sensitive observables. Additional constraints on the Higgs-gauge operators come from electroweak precision observables [20], while strong constraints on non-standard Yukawas, at the $\sim 1\%$ level, can be obtained from the total Higgs boson production cross section and from the Higgs boson decays [97, 98, 99].

We have so far only made use of the total WH and ZH cross sections. More differential information, such as the p_T spectrum of the Higgs boson or the distribution in invariant mass of the Higgs and vector boson, will allow to further tighten the constraints on the effective operators. In addition, in the presence of deviations from the SM expectations, such information would help to disentangle the possible new physics mechanisms. In Ref. [52] we discussed in detail WH production, and suggested that the angular distributions of the charged lepton in the W rest frame can be used to disentangle the different dimension-six operators. We further identified two angular coefficients, A_3 and A_5, which would pinpoint, respectively, the coupling of the W to right-handed quarks of the first generation, ξ_{ud}, or the CP-odd operator $\varphi^\dagger\varphi W_{\mu\nu}\tilde{W}^{\mu\nu}$. The same discussion can be extended to ZH production.
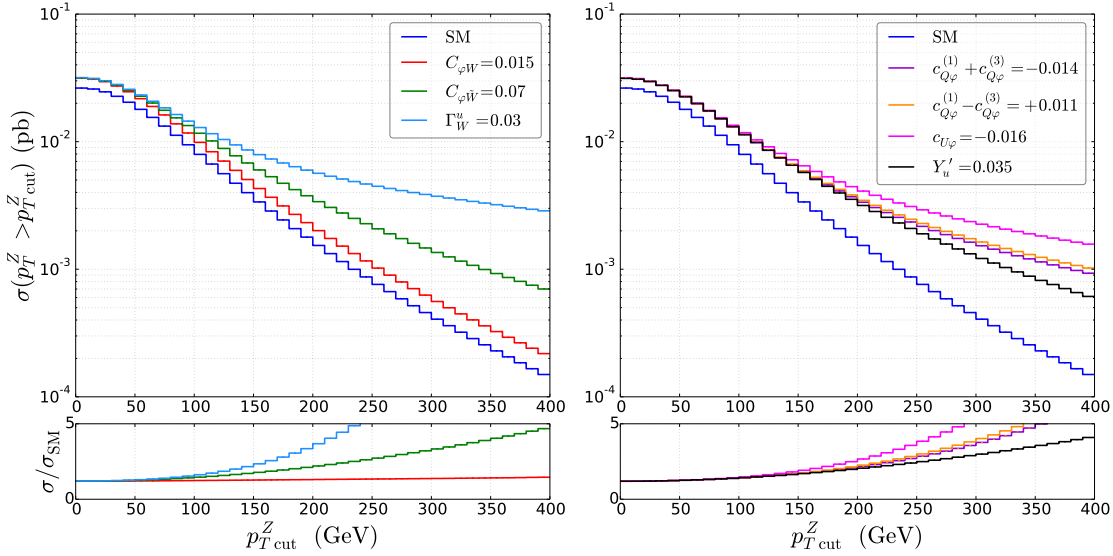
Figure 2.5: Cumulative ZH production cross section for $p_T^Z > p_{T\,\text{cut}}^Z$, at $\sqrt{S} = 13$ TeV.

In Fig. 2.5 we show the cumulative ZH cross section, as a function of a cut on the Z transverse momentum, for $\sqrt{S} = 13$ TeV. The blue line denotes the SM cross section, while we set the couplings of dimension-six operators so that the total cross section with no cut on p_T^Z is 20% larger than the SM. We see that for all operators the contribution increases at large p_T. The increase is most marked for the dipole operators $\Gamma_W^{u,d}$. In this case, if one neglects small SM Yukawas, there is no interference with the SM, and the contribution of the dipole operators is dominated by diagrams in which the Z and Higgs boson are created directly in the $q\bar{q}$ annihilation. These diagrams are enhanced by $(s/v^2)^3$ with respect to the SM, where $\sqrt{s}$ is the partonic center of mass energy. Similarly, the interference of $C_{\varphi\tilde{W}}$ with the SM does not contribute to the cumulative cross section. The correction is thus quadratic in $C_{\varphi\tilde{W}}$, and, for large s, is enhanced by $(s/v^2)^2$ with respect to the SM. In the case of $C_{\varphi W}$ and of the vertex corrections $c_{Q\varphi}^{(1)}$, $c_{Q\varphi}^{(3)}$, $c_{U\varphi}$ and $c_{D\varphi}$, there is competition between the interference and the quadratic pieces, which are enhanced by s/v^2 or $(s/v^2)^2$ compared to the SM, respectively. Finally, the non-standard Yukawa cross section is also enhanced by $p_T^2/m_{Z,W}^2$ at large p_T. Data on differential distributions from the LHC Run II would therefore be extremely helpful in constraining the effective operators in Table 2.4 at the few percent level.

As in the case of WH production, angular distributions of the leptons emitted in the decay of the Z boson can help disentangle the effects of different dimension-six operators. We work in the Z-boson rest frame, with the direction of the z-axis along the momentum of the Z boson in the lab frame. θ^* is the polar angle of the electron in this frame. The x-axis is in the direction orthogonal to the Higgs boson and Z momenta $\hat{x} \sim (\vec{p}_Z \times \vec{p}_H)$. In this frame, we define the azimuthal angle ϕ^* as the angle between the plane containing the
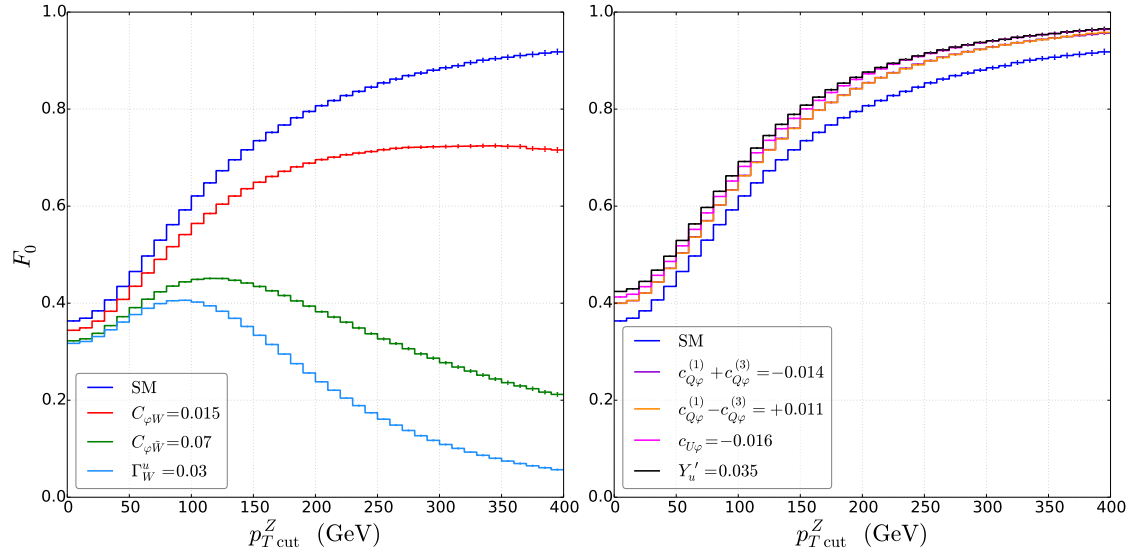
Figure 2.6: Longitudinal polarization of the Z boson in ZH as a function of $p_{T\,\mathrm{cut}}^Z$, at $\sqrt{S} = 13$ TeV.

Z and the Higgs bosons, and the plane containing the Z and the electron. That is

$$\cos\phi^* = \frac{(\vec{p}_Z \times \vec{p}_H) \cdot (\vec{p}_Z \times \vec{p}_{e^-})}{|\vec{p}_Z \times \vec{p}_H|\,|\vec{p}_Z \times \vec{p}_{e^-}|}\ , \tag{2.44}$$

and we note that ϕ^* is invariant under boosts along the Z momentum $\vec{p}_Z$. The angular distribution of the Z boson in this frame is parameterized by 8 coefficients

$$\frac{1}{\sigma}\frac{d\sigma}{d\cos\theta^*\,d\phi^*} = \frac{3}{16\pi}\Big[1 + \cos^2\theta^* + \frac{A_0}{2}(1 - 3\cos^2\theta^*) + A_1 \sin 2\theta^* \cos\phi^* + \frac{A_2}{2}\sin^2\theta^* \cos 2\phi^*$$

$$+ A_3 \sin\theta^* \cos\phi^* + A_4 \cos\theta^* + A_5 \sin\theta^* \sin\phi^* + A_6 \sin 2\theta^* \sin\phi^* + A_7 \sin^2\theta^* \sin 2\phi^*\Big]. \tag{2.45}$$

The coefficients A_0 and A_4 are related to the Z-boson helicity fractions [78, 43, 88].

$$F_0 = \frac{A_0}{2}\ , \qquad F_L - F_R = -\frac{A_4}{2}\,\alpha. \tag{2.46}$$

The difference between left- and right-handed polarization depends on A_4 and on the ratio $\alpha = (c_L^2 - c_R^2)/(c_L^2 + c_R^2)$, where $c_{L,R}$ are the couplings of the Z boson to left- and right-handed leptons. The operators we study do not modify these couplings at tree level, and α is fixed by the Weinberg angle, $\sin\theta_W$.

In Fig. 2.6 we show F_0 as a function of a cut on the Z transverse momentum. The figure shows that the Z boson is produced with a high degree of longitudinal polarization in the SM, and if the SM is modified by the couplings $c_{Q\varphi}^{(1)}$, $c_{Q\varphi}^{(3)}$, $c_{U\varphi}$ (and $c_{D\varphi}$, which is
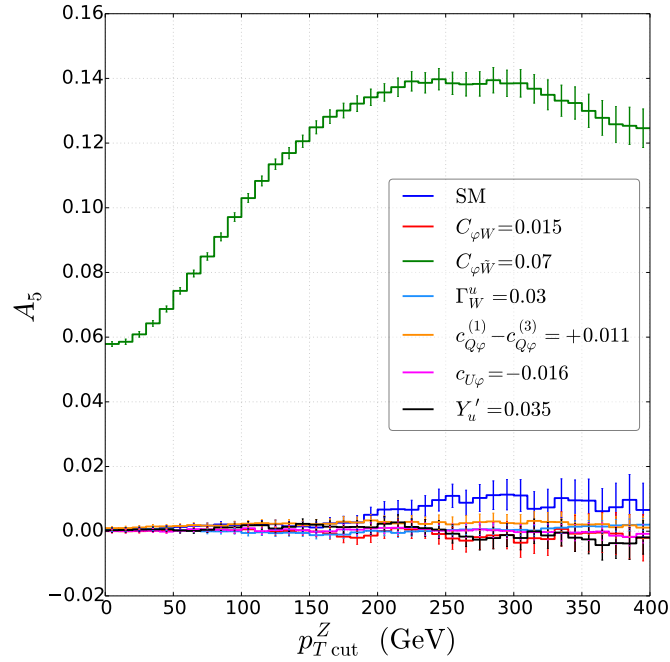
Figure 2.7: Angular coefficient A_5 as a function of $p^Z_{T\,\mathrm{cut}}$, at $\sqrt{S} = 13$ TeV.

not shown in the figure). These couplings have the same helicity structure as the SM Z couplings, and thus it is not surprising that they do not affect the polarization much. The situation is quite different for dipole operators, that prefer the Z boson to have transverse polarization, pushing F_0 to zero at large p_T. In the case of WH production, the operators Γ^u_W and Γ^d_W produce the W boson in an almost complete left-handed and right-handed polarized state, respectively [52]. In the case of ZH production, the difference between left- and right-polarization, captured by the coefficient A_4, is always small, so that both Γ^u_W and Γ^d_W produce a right-polarized Z boson approximately half of the times. The operator $C_{\varphi\tilde{W}}$ also prefers the Z to be transversely polarized.

The remaining coefficients in Eq. (2.45) also carry important information. For example, A_5 is sensitive to CP violation. A_5 vanishes in the SM, at NLO in QCD, but it receives a large contribution from the interference of the operator $C_{\varphi\tilde{W}}$ with the SM, as shown in Fig. 2.7. The remaining dimension-six operators, at least with the assumptions of Sec. 2.2 on their flavor structure, do not contribute to A_5, thus making it a clean observables to pinpoint $C_{\varphi\tilde{W}}$. The uncertainties depicted in Figs. 2.5 - 2.7 only include the statistical error of the Monte Carlo integration.
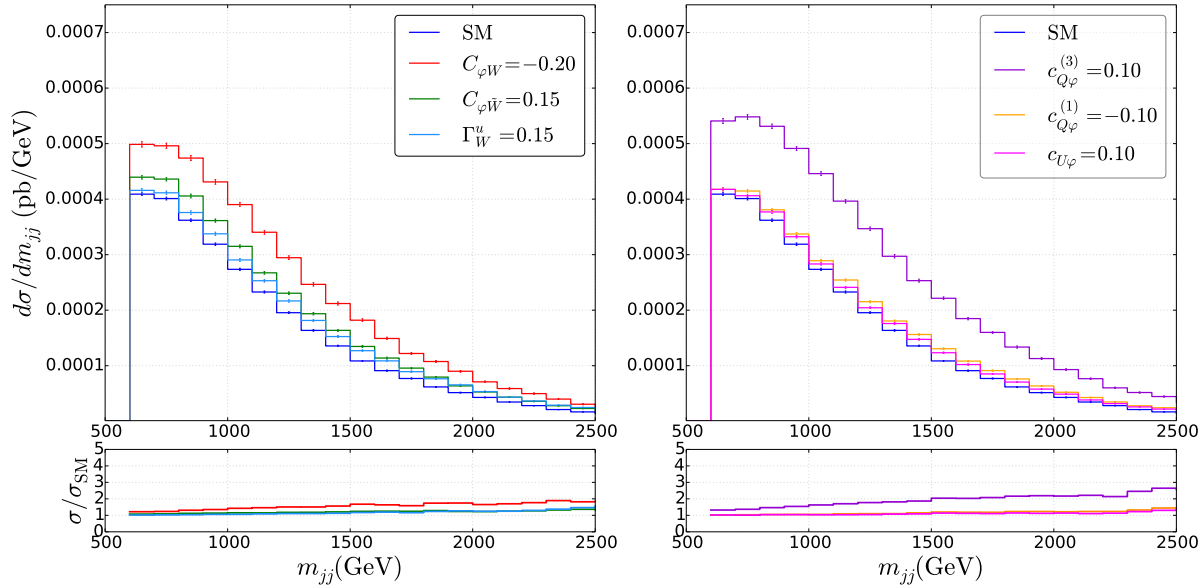
Figure 2.8: Differential VBF cross section, as a function of the dijet invariant mass m_{jj}, at $\sqrt{S} = 8$ TeV, with the standard VBF cuts described in the text.

2.5 Vector boson fusion

Finally we discuss the corrections to Higgs boson production via vector boson fusion. The total cross section for Higgs boson production through VBF has been recently computed in the SM at N³LO in QCD [100]. Fully-differential distributions are available up to NNLO [101] and the interface with parton showering is available at NLO+PS accuracy [25]. For this study, we computed the NLO QCD corrections to both the SM and the dimension-six SM-EFT contributions to the VBF cross sections, building upon the POWHEG implementation presented in Ref. [25]. The contribution of SM-EFT operators, including NLO QCD corrections, has been considered in Ref. [89, 90, 93]. Here we study the operators in Table 2.2, with the flavor assumptions discussed in Sec. 2.2.2.

As in Ref. [25], we neglect contributions from VH production, with the vector boson decaying hadronically, and, for channels with two identical quarks in the final state, we neglect effects due to the interchange of identical quarks. These effects are suppressed in the experimentally interesting region with two widely separated jets of large invariant mass. In the implementation of Ref. [25], POWHEG generates events with the CKM matrix set to the identity, thus reducing the number of Feynman diagrams and singular regions. The final state quarks are then reweighted by the SM CKM matrix before they are showered by a Monte Carlo program. One could use the same approach for dimension-six operators that do not couple to quarks, such as $C_{\varphi W}$. On the other hand, if the SM-EFT operators couples to quarks, such reweighting is not possible, and one needs to generate events with the proper flavor configuration.

Some of the operators described in Section 2.2, such as $\Gamma_\gamma^{u,d}$ or $C_{\varphi B}$, induce contributions to VBF mediated by the exchange of a photon. These contributions can generate collinear divergences, which are cut-off by the p_T and rapidity cuts in the experimentally relevant region, but can make the generation of events extremely inefficient. In order to avoid these singular regions, if the coefficients of operators involving photons are turned on, the generation of events should be performed setting the `bornsuppfact` flag to an appropriate value in the `powheg.input` file.

In Fig. 2.8 we plot the differential cross section with respect to the dijet invariant mass, at $\sqrt{S} = 8$ TeV. We applied the standard VBF cuts, requiring the invariant mass of the two jets to be $m_{jj} > 600$ GeV, the rapidity separation $|y_{j_1} - y_{j_2}| > 4.2$, and that all jets have $p_{Tj} > 20$ GeV and $|y_j| < 5$. We computed the cross section at the renormalization scale $\mu = 2m_Z$, and used the first member of `PDF4LHC15_nlo_30` PDF set. The error bars in Fig. 2.8 only reflect the statistical error of the Monte Carlo integration. The blue curve denotes the SM cross section, while the remaining curves depict the effect of dimension-six operators, turned on one at a time. The coefficients are chosen to be close to the values excluded by VH production, shown in Table 2.4. For these values the correction to the VBF signal strength goes from 10-15% in the case of $C_{\varphi\tilde{W}}$, Γ_W^u, $c_{Q\varphi}^{(1)}$ and $c_{U\varphi}$, to 40% in the case of $C_{\varphi W}$ and 60% in the case of $c_{Q\varphi}^{(3)}$. The VBF signal strength measured at the LHC Run I [94] allows for such deviations, so that, with the exception of $c_{Q\varphi}^{(3)}$, including VBF does not improve the constraints discussed in Section 2.4.

The lower sensitivity of VBF compared to ZH and WH production can be appreciated from the bottom panel of Fig. 2.8, which shows that the VBF cross section induced by SM-EFT operators grows slowly as the dijet invariant mass increases. One advantage of VBF is the possibility to flavor tag the jets in the final states, providing an additional handle on the flavor structure of SM-EFT operators.

2.6 Brief Conclusion

In the previous section we have shown that the Standard Model as an effective field theory can be a very powerful tool in providing general bounds on the scale of new physics. By comparing corrections to Standard Model cross sections in charged and neutral Drell-Yan production, production of a Higgs with associated W/Z and Higgs production via VBF we have obtained several strong exclusion limits for the scale of new physics. See the end of this manuscript for a more in depth discussion of the results and implications.

Chapter 3

W+Charm production

3.1 Introduction

To date, the strange quark parton distribution function, PDF, is one of the least well known Standard Model physical quantities [102]. W+charm quark production is a calculation that can directly probe the strange quark PDF, and a reduction in strange PDF uncertainty will have an effect on many other Standard Model measurements. The process of W+charm production has two physical scales, one of which can vary on a wide range of orders of magnitude and another that is relatively fixed. The first widely varying scale is the hardness of the event that is probed with the momentum of the final state charm quark, or, by proxy, the momentum of a final state D meson that is well separated from other final state radiation. The second scale is the mass of the D meson. As in most physical processes described by two disparate scales, the scales enter into the calculation of a physical observable as a log of scales. If the observable is the transverse momentum of the final state D meson than

$$\frac{\mathrm{d}\sigma}{\mathrm{d}p_T} = \alpha_s^2 \sum_{n=0}^{\infty} a_n \left(\alpha_s \log \frac{p_T}{m_D} \right)^n + \alpha_s^3 \sum_n b_n \left(\alpha_s \log \frac{p_T}{m_D} \right)^n + \ldots \tag{3.1}$$

So that when $p_T \gg m_D$, and

$$\alpha_s \log \frac{p_T}{m_D} \sim 1 \tag{3.2}$$

the perturbative expansion of Eq. (3.1) is no longer valid as every higher order term is as large, or larger, than the lower order terms. However, when $p_T \sim m_D$ the logs of Eq. (3.1) are small, and a perturbative approach will yield a sensible result. What is needed is a method to: 1.) Handle the large logs so that a perturbative expansion can still give a physical result and 2.) Combine the two different regions of phase space, those of large

and small logs, into one calculation that produces the correct perturbative expansion in the correct limits. In the following sections we discuss such method with respect to W+charm production.

3.2   Theoretical Setup

3.2.1   Fixed order cross section

In the regime where the p_T of the heavy D meson is on the order of the heavy meson mass, $m_D \sim p_T$, the logs of Eq. (3.1) are small and fixed order perturbation theory can be used to calculate the differential cross section. The fixed order cross section is written

$$\frac{\mathrm{d}\sigma^{FO}}{\mathrm{d}\phi_{WD}} = \int \mathrm{d}\phi_{Wc}^m \mathrm{d}z \sum_{a,b} f_a(x_a, \mu^2) \, f_b(x_b, \mu^2)$$

$$\times \frac{D(z,\mu^2)_{c/D}^{NP}}{z^2} \times \frac{\mathrm{d}\hat{\sigma}_{ab \to Wc}}{\mathrm{d}\phi_{Wc}^m} \delta^{(5)}(\phi_{WD} - \phi_{WD}(\phi_{Wc}^m, z)) \,. \tag{3.3}$$

Where the partonic cross sections are defined as a power series in α_s

$$\frac{\mathrm{d}\hat{\sigma}_{ab \to Wc}}{\mathrm{d}\phi_{Wc}^m} = \sum \left(\frac{\alpha_s}{2\pi}\right)^n \frac{\mathrm{d}\hat{\sigma}_{ab \to Wc}^{(n)}}{\mathrm{d}\phi_{Wc}^m} \tag{3.4}$$

and differential phase space measures are, with $p_c^2 = m_c^2$

$$\mathrm{d}\phi_{WD} \equiv \mathrm{d}x_a \mathrm{d}x_b \frac{\mathrm{d}^3 p_W}{(2\pi)^3 2E_W} \frac{\mathrm{d}^3 p_D}{(2\pi)^3 2E_D} \mathrm{d}z (2\pi)^4 \delta^{(4)}(k_a + k_b - p_W - p_D/z)$$

$$\mathrm{d}\phi_{Wc}^m \equiv \mathrm{d}x_a \mathrm{d}x_b \frac{\mathrm{d}^3 p_W}{(2\pi)^3 2E_W} \frac{\mathrm{d}^3 p_c}{(2\pi)^3 2E_c} (2\pi)^4 \delta^{(4)}(k_a + k_b - p_W - p_c) \,. \tag{3.5}$$

Because the heavy quark mass acts to stop hard, collinear radiation emission, up to power corrections of Λ_{QCD}/m_D, the charm quark momentum is identified with the momentum of the observed D meson. The delta function $\delta(\phi_{WD} - \phi_{WD}(\phi_{Wc}^m, z))$ ensures the phase space of the massive charm quark and W boson maps onto the phase space of the W and observed D meson. The $D_{c/D}^{NP}(z)$ term is the non-perturbative model that is convolved with the fragmentation function before resummation. This factor needs to be included in the fixed-order calculation so that the two cross sections, fixed-order massive and resummed massless, can cancel in the appropriate limits.

3.2.2   Resummed cross section

In the region of final state phase space where p_T becomes large compared to the heavy meson mass, $m_D \ll p_T$, the mass of the charm can be ignored. As discussed above, this spoils the perturbative expansion of the cross section and leads to infrared singularities associated with radiation collinear to the final state charm quark. In a method analogous to the inclusion of collinear singularities due to emission of radiation of massless initial state partons into parton distribution functions, the final state collinear singularities can be absorbed into a fragmentation function, which encapsulates the physics of the final state charm quark hadronizing into a heavy meson. The cross section in which logarithms of p_T/m_D have been resummed can be written as

$$
\frac{\mathrm{d}\sigma^{RS}}{\mathrm{d}\phi_{WD}} = \int \mathrm{d}\phi_{Wc}^0 \mathrm{d}z \sum_{a,b} f_a(x_a,\mu^2)\, f_b(x_b,\mu^2)
$$

$$
\times \frac{D(z,\mu^2)_{c/D}}{z^2} \times \frac{\mathrm{d}\hat{\sigma}_{ab\to Wc}}{\mathrm{d}\phi_{Wc}^0} \delta^{(5)}(\phi_{WD} - \phi_{WD}(\phi_{Wc}^0,z)) \tag{3.6}
$$

and, as with the massive, fixed-order, partonic cross section, the massless, partonic cross section is defined as a power series in α_s

$$
\frac{\mathrm{d}\hat{\sigma}_{ab\to Wc}}{\mathrm{d}\phi_{Wc}^0} = \sum \left(\frac{\alpha_s}{2\pi}\right)^n \frac{\mathrm{d}\hat{\sigma}_{ab\to Wc}^{(n)}}{\mathrm{d}\phi_{Wc}^0} . \tag{3.7}
$$

The massless case phase space measures, $\mathrm{d}\phi_{WD}$ and $\mathrm{d}\phi_{Wc}^0$ are equivalent to the massive phase space measures with the replacement that $p_c^2 = 0$.

3.2.3   Combining fixed order and resummed cross sections

To create a calculable cross section that will reproduce the correct physical behavior in different regions of phase space we need to combine the two previously defined cross sections. This is done by writing

$$
\frac{\mathrm{d}\sigma}{\mathrm{d}\phi_{WD}} = \frac{\mathrm{d}\sigma^{FO}}{\mathrm{d}\phi_{WD}} + \frac{\mathrm{d}\sigma^{RS}}{\mathrm{d}\phi_{WD}} - \frac{\mathrm{d}\sigma^{RE}}{\mathrm{d}\phi_{WD}} . \tag{3.8}
$$

In order that the sum in Eq. (3.8) exactly recreates the fixed order result at low p_T and the resummed result at high p_T, $\mathrm{d}\sigma^{RE}$ must be a quantity that, up to terms power

suppressed by m_D/p_T, is equal to the fixed order cross section at high p_T and the resummed cross section at low p_T. This quantity can be found in one of two ways. It can be found as the resummed cross section expanded to the same order in α_s as the fixed order OR the result of the resummed cross section calculation with the resummed fragmentation function replaced with its un-resummed initial condition. So that when $m_D \ll p_T$

$$
\begin{aligned}
\frac{d\sigma}{d\phi_{WD}} &= \frac{d\sigma^R}{d\phi_{WD}} + \frac{d\sigma^{FO}}{d\phi_{WD}} - \frac{d\sigma^{RE}}{d\phi_{WD}} \\
&= \frac{d\sigma^{RS}}{d\phi_{WD}} + \frac{d\sigma^{FO}}{d\phi_{WD}} \left[1 - 1 + \mathcal{O}\left(\frac{m_D}{p_T^D} \right) \right] \xrightarrow[\frac{m_D}{p_T} \to 0]{} \frac{d\sigma^{RS}}{d\phi_{WD}} .
\end{aligned}
\tag{3.9}
$$

In the limit $p_T \sim m_D$, there are no large logs, such that the expanded, resummed result becomes equal to the resummed result and

$$
\begin{aligned}
\frac{d\sigma}{d\phi_{WD}} &= \frac{d\sigma^{FO}}{d\phi_{WD}} + \frac{d\sigma^R}{d\phi_{WD}} - \frac{d\sigma^{RE}}{d\phi_{WD}} \\
&= \frac{d\sigma^{FO}}{d\phi_{WD}} + \frac{d\sigma^R}{d\phi_{WD}} \left[1 - 1 + \mathcal{O}\left(\alpha_s^n \log^n \frac{m_D}{p_T^D} \right) \right] \xrightarrow[\frac{m_D}{p_T} \to 1]{} \frac{d\sigma^{FO}}{d\phi_{WD}} .
\end{aligned}
\tag{3.10}
$$

There is overlap in the two cross sections that is not perfectly canceled by subtracting $d\sigma^{RE}$ that can be suppressed in one of two ways. One way, employed by [103], is to modify Eq. (3.8) to include a suppression function $G(m_D, p_T)$ so that

$$
\frac{d\sigma}{d\phi_{WD}} = \frac{d\sigma^{FO}}{d\phi_{WD}} + \left(\frac{d\sigma^R}{d\phi_{WD}} - \frac{d\sigma^{RE}}{d\phi_{WD}} \right) \times G(m_D, p_T) .
\tag{3.11}
$$

$G(m_D, p_T)$ is chosen such that it approaches 0 as $m_D/p_T \to 1$ and 1 as $m_D/p_T \to 0$. The authors of [103] chose

$$
G(m_D, p_T) = \frac{p_T^2}{p_T^2 + c^2 m_D^2}
\tag{3.12}
$$

where c is a constant chosen to set the energy scale at which the suppression switches on/off. We discuss modifications to this suppression function in numerical implementation below.

Another approach to deal with the double counting of terms in Eq. (3.8) is to utilize a profile scale in the resummation $\mu = \mu(p_T)$ chosen such that it smoothly interpolates from $\mu(p_T) = m_D$ for $p_T < \rho \, m_D$ to $\mu(p_T) = p_T$ for $p_T \gg m_D$. One such profile scale function is

$$\mu(p_T) = \begin{cases} m_D\,, & 0 \le p_T \le \rho \, m_D \\ m_D \frac{\mu_{\mathrm{eq}} - p_T}{\mu_{\mathrm{eq}} - \rho \, m_D} + \mu_{\mathrm{eq}} \frac{p_T - \rho \, m_D}{\mu_{\mathrm{eq}} - \rho \, m_D}\,, & \rho \, m_D \le p_T \le \mu_{\mathrm{eq}} \\ p_T\,, & \mu_{\mathrm{eq}} \le p_T \end{cases} \tag{3.13}$$

Much like c in the suppression function, here ρ is chosen to set the scale at which the interpolation is performed.

3.3 Fragmentation Function

3.3.1 Definition of the Fragmentation Function

The fragmentation function describes the probability of a final state parton k with momentum p_k to fragment into a hadron(a D meson in this case) with momentum p_D such that $p_k = p_D/z$. Fragmentation functions of heavy quarks are very important for the study of QCD as they involve scales that span a range from $\mu \gg \Lambda_{QCD}$, where perturbative theory can be used, and scales such that $\mu \sim \Lambda_{QCD}$ where the physics is purely non-pertubative. The main upshot of such a hierarchy of scales is that the quark mass acts as a lower energy cutoff for collinear radiation and perturbation theory methods can be employed. The partonic component of the fragmentation function can be written as a power series in α_s as

$$D_{ij}(z, \mu^2, m_c^2) = \sum_{n=0}^{\infty} \left(\frac{\alpha_s}{2\pi}\right)^n D_{ij}^{(n)}(z, \mu^2, m_c^2)\,. \tag{3.14}$$

The fragmentation function to $\mathcal{O}(\alpha_s)$ are

$$D_{qq}^{(0)}(z, \mu^2, m_c^2) = \delta(1 - z)\,, \tag{3.15}$$

$$D_{qq}^{(1)}(z, \mu^2, m_c^2) = C_F \left\{ \left[\frac{1 + z^2}{1 - z}\right]_+ \left(\log \frac{\mu^2}{m_c^2} - 1\right) - 2\left[\frac{1 + z^2}{1 - z}\log(1 - z)\right]_+ \right\}\,, \tag{3.16}$$

$$D_{qg}^{(1)}(z, \mu^2, m_c^2) = C_F \frac{(1 - z)^2 + 1}{z}\left(\log \frac{\mu^2}{m_c^2} - 1\right)\,, \tag{3.17}$$

$$D_{gq}^{(1)}(z, \mu^2, m_c^2) = T_R(z^2 + (1 - z)^2)\log \frac{\mu^2}{m_c^2}\,. \tag{3.18}$$

The evolution of the fragmentation functions is perturbative and governed by the DGLAP equation

$$\frac{\mathrm{d}}{\mathrm{d}\log\mu^2}D_{i/D}(z,\mu^2) = \sum_j \int \frac{\mathrm{d}\xi}{\xi} P_{ij}(\xi)D_{j/D}\left(\frac{z}{\xi},\mu^2\right). \tag{3.19}$$

$P_{ji}(\xi)$ are the time-like Altarelli-Parisi splitting functions

$$P_{ji}(z) = \frac{\alpha_s}{2\pi} \sum_{n=0}^{\infty} \left(\frac{\alpha_s}{2\pi}\right)^n P_{ji}^{(n)}(z), \tag{3.20}$$

with, at one loop,

$$P_{q_j q_i}^{(0)}(z) = \delta_{ij}C_F\left((1+z^2)\left[\frac{1}{1-z}\right]_+ + \frac{3}{2}\delta(1-z)\right), \tag{3.21}$$

$$P_{gq}^{(0)}(z) = C_F\left(\frac{1+(1-z)^2}{z}\right), \tag{3.22}$$

$$P_{qg}^{(0)}(z) = T_R\left(z^2+(1-z)^2\right), \tag{3.23}$$

$$P_{gg}^{(0)}(z) = 2C_A\left(z\left[\frac{1}{1-z}\right]_+ + \frac{1-z}{z} + z(1-z)\right) + \frac{\beta_0}{2}\delta(1-z). \tag{3.24}$$

The color factors in Eqs.(3.21)–(3.24) are $C_F = 4/3$, $C_A = 3$, $T_R = 1/2$, while β_0 is the leading order coefficient of the beta function,

$$\beta_0 = \frac{11}{3}C_A - \frac{4}{3}T_R n_f. \tag{3.25}$$

The space-like and time-like splitting functions at $\mathcal{O}(\alpha_s^2)$ are given, for example, in Ref. [104]. The non-singlet components and the singlet splitting functions $P_{qq}^{(2)}$ and $P_{gg}^{(2)}$ are given in Refs. [105, 106] and the non-diagonal entries of the singlet matrix, $P_{gq}^{(2)}$ and $P_{qg}^{(2)}$, were calculated in Ref. [107]. However, luckily, in the case of W+charm production, experimentalists use observables in which gluon splitting does not contribute, $\mathcal{O}(D_{c/D} - D_{\bar{c}/D})$, so that there is no gluon fragmentation function contribution.

3.3.2 Solutions to DGLAP

In general, the solution of Eq. (3.19) can be done in several ways, namely: Mellin transformations, orthogonal polynomials methods and brute-force methods.

3.3.2.1 Brute Force

The brute force method [108] was used in the evolution of the fragmentation function at LO and NLO. In this method the derivative of Eq. (3.19) is converted from continuous to discrete by

$$\frac{\mathrm{d}}{\mathrm{d}\log\mu^2}D_{i/D}(z,\mu^2) = \frac{[D_{i/D}(z,\mu^2_{m+1}) - D_{i/D}(z,\mu^2_m)]}{\Delta\log\mu^2_m} \, . \tag{3.26}$$

With this replacement and making the further assumption that the convolutional integral varies slowly as a function of μ then Eq. (3.19) becomes

$$D_{i/D}(z,\mu^2_{m+1}) = D_{i/D}(z,\mu^2_m) + \Delta\log\mu^2_m \sum_j \int \frac{\mathrm{d}\xi}{\xi} P_{ij}(\xi) D_{j/D}\left(\frac{z}{\xi},\mu^2_m\right) \, . \tag{3.27}$$

We shall see shortly that this assumption is valid as the step size in $\mu_m \to 0$. Now we have a method for solving DGLAP evolution numerically, step-by-step. The major drawback of this approach is that in order to provide a numerically stable solution the partonic fragmentation function must also be convoluted with a non-perturbative model. For heavy quarks, a common model is chosen to be, Ref. [109],

$$D_{\mathrm{mod}}(z) = \frac{1}{1+c}\left(\delta(1-z) + c\frac{\Gamma(2+a+b)}{\Gamma(1+a)\Gamma(1+b)}(1-z)^a z^b\right) . \tag{3.28}$$

Once a model is chosen however, it is relatively straightforward to implement Eq. (3.27). A common method to reduce errors caused by the assumption that the integral slowly varies is Heun's method. Heun's method is a variant of the Runge-Kutta second order method in which Eq. (3.27) is calculated for two steps in μ before updating $D_{i/D}(z,\mu^2_{m+1})$ and averaging the results. This can be written as

$$\overline{D}_{i/D}(z,\mu^2_{m+1}) = D_{i/D}(z,\mu^2_m) + \Delta\log\mu^2_m \sum_j \int \frac{\mathrm{d}\xi}{\xi} P_{ij}(\xi) D_{j/D}\left(\frac{z}{\xi},\mu^2_m\right)$$

$$\overline{\overline{D}}_{i/D}(z,\mu^2_{m+1}) = D_{i/D}(z,\mu^2_m) + \Delta\log\mu^2_m \sum_j \int \frac{\mathrm{d}\xi}{\xi} P_{ij}(\xi) \overline{D}_{j/D}\left(\frac{z}{\xi},\mu^2_m\right)$$

So that the final result for $D_{i/D}(z, \mu_{m+1}^2)$ is

$$D_{i/D}(z, \mu_{m+1}^2) = \frac{1}{2}\left(\overline{D}_{i/D}(z, \mu_{m+1}^2) + \overline{\overline{D}}_{i/D}(z, \mu_{m+1}^2) \right) \tag{3.29}$$

One might also notice that Eq. (3.19) for a given fragmentation function receives contributions from all particles that can fragment into the heavy mesons initiating parton. In a full treatment of the evolution of fragmentation functions Eq. (3.19) is now a series of coupled integro-differential equations. Explicitly writing the evolution equation as

$$\frac{\mathrm{d}}{\mathrm{d}\log\mu^2}D_{q_i/D}(z, \mu^2) = \int \frac{\mathrm{d}\xi}{\xi}\left\{ \sum_j P_{q_i q_j}(\xi)D_{q_j/D}\left(\frac{z}{\xi}, \mu^2\right) + P_{q_i g}(\xi)D_{g/D}\left(\frac{z}{\xi}, \mu^2\right) \right\} \tag{3.30}$$

$$\frac{\mathrm{d}}{\mathrm{d}\log\mu^2}D_{g/D}(z, \mu^2) = \int \frac{\mathrm{d}\xi}{\xi}\left\{ \sum_j P_{g q_j}(\xi)D_{q_j/D}\left(\frac{z}{\xi}, \mu^2\right) + P_{gg}(\xi)D_{g/D}\left(\frac{z}{\xi}, \mu^2\right) \right\} \tag{3.31}$$

$$\tag{3.32}$$

one can see that despite starting at zero $D_{g/D}(z, \mu^2)$ receives corrections from its coupling to the quark fragmentation functions. While gluon splitting does not contribute to the class of observables that we will consider one should still include its running while evolving $D_{c/D}(z, \mu^2)$.

3.3.2.2   Mellin Inversion

Another popular approach to DGLAP evolution is the Mellin transformation, where the Mellin transform is defined as

$$\widetilde{F}(N) = \int_0^1 dx\, x^{N-1} f(x)\,. \tag{3.33}$$

So that now Eq. (3.19) becomes

$$\frac{\mathrm{d}}{\mathrm{d}\log\mu^2}\widetilde{D}_D(N,\mu^2) = \widetilde{\gamma}^{(0)}(N,\mu^2)\widetilde{D}_D\left(N,\mu^2\right) \tag{3.34}$$

with

$$\widetilde{\gamma}^{(0)}(N,\mu^2) \equiv \frac{\alpha_s(\mu^2)}{2\pi}\widetilde{P}^{(0)}(N) \tag{3.35}$$

and $\widetilde{D}_D(N,\mu^2)$ and $\widetilde{P}^{(0)}(N)$ are the Mellin transformed fragmentation function and splitting kernel respectively.

Below we present a short derivation of the leading-log resummation equation, in Mellin space. Using

$$\mathrm{d}\log\mu^2 = \frac{\mathrm{d}\alpha_s(\mu^2)}{\beta(\alpha_s)} \tag{3.36}$$

and

$$\beta(\alpha_s) = -b_0\,\alpha_s^2(1 + b_1\alpha_s + b_2\alpha_s^2 + \mathcal{O}(\alpha_s^3))\,. \tag{3.37}$$

Using the above replacements and expanding to leading order in α_s, (3.34) becomes a more recognizable form

$$\frac{\mathrm{d}\widetilde{D}_D(N,\mu^2)}{\widetilde{D}_D(N,\mu^2)} = -\frac{1}{2\pi b_0}\frac{\mathrm{d}\alpha_s(\mu^2)}{\alpha_s(\mu^2)}\,\widetilde{P}^{(0)}(N)\,. \tag{3.38}$$

Eq. (3.38) has the solution

$$\widetilde{D}_D(N,\mu^2) = \widetilde{D}_D(N,\mu_0^2)\left(\frac{\alpha_s(\mu_0^2)}{\alpha_s(\mu^2)}\right)^{\frac{\widetilde{P}^{(0)}(N)}{2\pi b_0}}\,. \tag{3.39}$$

With the above method it is relatively straightforward to derive higher order resummation terms, again in Mellin space. Here, without derivation, the NLL result for $D_D(z,\mu^2)$ is

$$\frac{\widetilde{D}_D(N,\mu^2)}{\widetilde{D}_D(N,\mu_0^2)} = \left(\frac{\alpha_s(\mu_0^2)}{\alpha_s(\mu^2)}\right)^{\frac{\widetilde{P}^{(0)}(N)}{2\pi b_0}} \exp\left\{\frac{\alpha_s(\mu^2)-\alpha_s(\mu_0^2)}{4\pi^2 b_0}\left[\widetilde{P}^{(1)}(N)-\frac{2\pi b_1}{b_0}\widetilde{P}^{(0)}(N)\right]\right\}. \quad (3.40)$$

Where $\widetilde{P}^{(1)}(N)$ is the Mellin transform of the next-to-leading order spilling functions and $\widetilde{D}_D(N,\mu_0^2)$ is, as at LO, the fragmentation function initial condition or the fixed order fragmentation function before evolution. In this case $\widetilde{D}_D(N,\mu_0^2)$ is

$$\widetilde{D}_D(N,\mu_0^2) = \int dz\, z^{N-1}$$
$$\times \left\{\delta(1-z) + \frac{\alpha_s(\mu_0^2)}{2\pi}\, C_F\left[\frac{1+z^2}{1-z}\left(\log\left(\frac{\mu_0^2}{m_c^2}\right)-2\log(1-z)+1\right)\right]_+\right\}. \quad (3.41)$$

After Mellin transformation, it is clear that Eqs. (3.39) and (3.40) are much simpler to calculate numerically than Eq. (3.19). The difficulty with this approach, however, lies in the return to z space required to use the evolved fragmentation function in cross section calculations.

The inverse Mellin transform is defined as

$$f(x) = \frac{1}{2\pi i}\int_{c-i\infty}^{c+i\infty} dN\, x^{-N}\widetilde{F}(N), \quad (3.42)$$

where the contour defined by $\int_{c-i\infty}^{c+i\infty}$ should be choosen c such that the poles of $x^{-N}\widetilde{F}(N)$ lie to the left of c in the complex plane.

Given the form of the inverse Mellin transformation it is clear that straightforward, numerical solution to integration is not possible. A common approach to solving this inversion equation is to deform the contour in Eq. (3.42) and approximate the curve of steepest descent of the contour. This approximation is done with a summation of Laguerre polynomials which can be numerically evaluated for a fixed μ^2 and z, [110]. Unfortunately, this method of Mellin inversion is unstable for the evolution of fragmentation functions beyond leading order. Both parton distribution functions and fragmentation functions evolve according to Eq. (3.19), and both scale as $\frac{1}{N}$ for small N in Mellin space. While PDF's are regular as $z \to 1$, fragmentation functions and their initial conditions beyond leading order are not. Starting at next-to-leading order the initial conditions of $D_{j/D}(z/\xi,\mu^2)$ involve plus distributions, whose Mellin transforms tend towards negative infinity for large N. So for some

values of μ^2 and z the contour in Eq. (3.42) has no saddle point and the numerical calculation is wildly unstable. So far literature on the subject has yet to yield a proof that such ill-behaved functions at $z \to 1$ do or do not have a stable numerical method for Mellin inversion. While it is possible that one exists, it is beyond the scope of this work to investigate further. Despite being only a LO method, the Mellin/Inverse Mellin transformation method does have a novel use. In the case of the brute force method the fragmentation function was first convoluted with a non-perturbative model in order for numerical convergence. In the Mellin method no such model is needed. A purely partonic resummed fragmentation function can be used to internally test numerical implementation and as a good cross check on the brute force method.

3.3.2.3   Numerical Results

In Fig. 3.1a we plot the leading-log fragmentation function that was resummed by first convoluting with a non-perturbative model then solving Eq. (3.19) with the brute force method. By comparison, Fig. 3.1b is the leading-log fragmentation function resummed with the Mellin inversion method with no need for convolution with a non-perturbative model. Note that in the fragmentation function without a model the delta function initial condition has been smeared out but still has a strong rise as $z \to 1$. It is not surprising that the brute force method struggles to numerically converge with such a feature.

In Fig. 3.1c we have plotted a straightforward check on the charm fragmentation function. The blue curve is the numerical value of the left-hand side of Eq. (3.19) or the derivative of the charm fragmentation function with respect to the scale μ plotted over a range of z. The orange curve is the numerical value of the right-hand side of Eq. (3.19) or the integral of coupled fragmentation functions convolved with their respective splitting kernels over a range of z. This plot, Fig. 3.1c, shows that indeed the resummed charm fragmentation function solves the DGLAP running equation, Eq. (3.19). As a complement to the numerical result of Fig. 3.1c we have also shown the same numerical check for the gluon fragmentation function in Fig. 3.1d. This also clearly is a solution to the DGLAP evolution equation. As discussed above even though the initial condition for the gluon fragmentation function was zero it was made non-zero by its coupling to the charm fragmentation function.
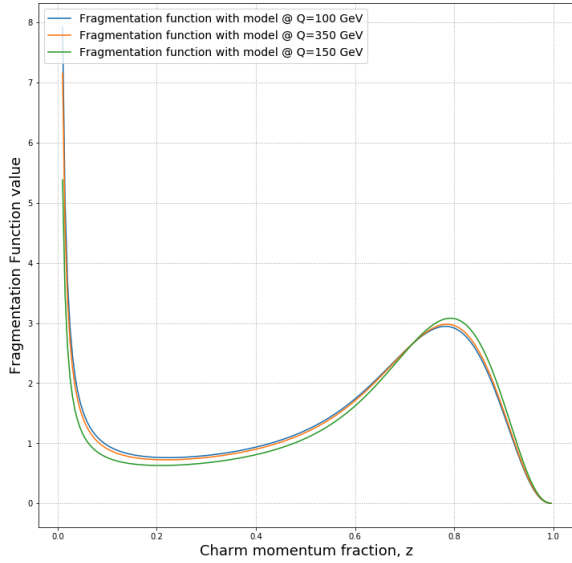
(a) Leading-log Fragmentation function convolved with non-perturbative model before resummation.
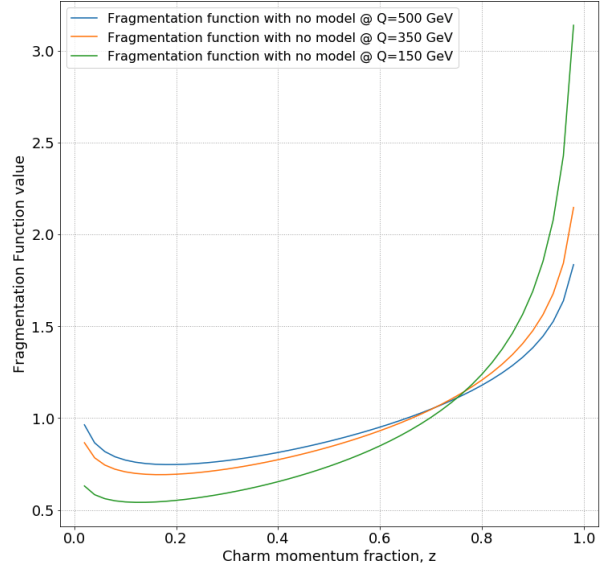
(b) Leading-log Fragmentation function resummed without convolution with non-perturbative model
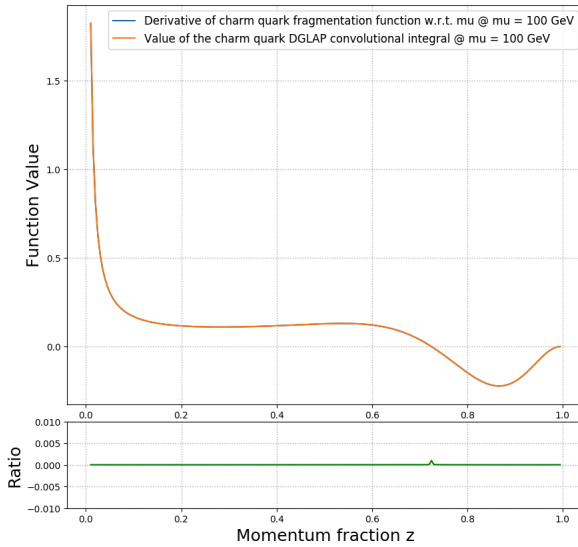
(c) (Blue curve)Left-hand side of Eq. (3.19), the value of the derivative of the charm fragmentation function with respect to μ calculated for the range of momentum-fraction z (Orange curve) Right-hand side of Eq. (3.19), the value of the charm quark DGLAP convolutional integral on the range of z (Green Curve) Ratio of the two curves.
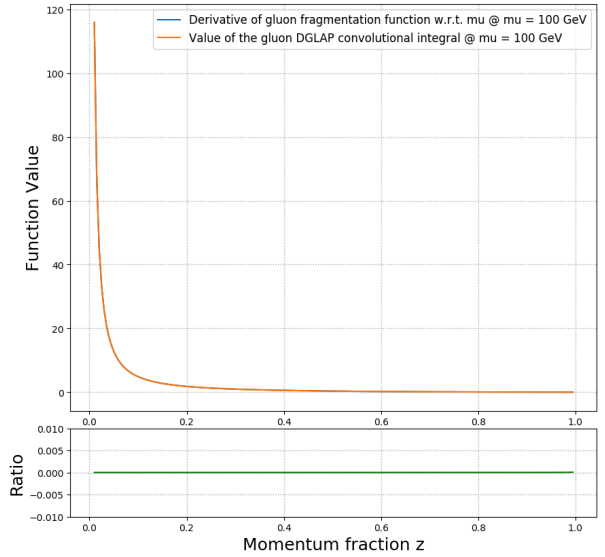
(d) (Blue curve)Left-hand side of Eq. (3.19), the value of the derivative of the gluon fragmentation function with respect to μ calculated for the range of momentum-fraction z (Orange curve) Right-hand side of Eq. (3.19), the value of the gluon DGLAP convolutional integral on the range of z (Green Curve) Ratio of the two curves.

Figure 3.1: Numerical results for fragmentation function resummation and checks.

3.4 LOLL implementation

What follows is a discussion of a numerical implementation of the calculation at leading-order plus a leading-log resummation of the fragmentation function. By taking Eqs. (3.3), (3.6), (3.8) and using the leading-order terms in α_s these become

$$
\begin{aligned}
\frac{\mathrm{d}\sigma^{LOLL}}{\mathrm{d}\phi_{WD}} =& \sum_{a,b} \int \mathrm{d}\phi_{Wc}^m \, f_a(x_a, \mu^2) \, f_b(x_b, \mu^2) \, \times \, \frac{\mathrm{d}\hat{\sigma}_{ab\to Wc}^{(0)}}{\mathrm{d}\phi_{Wc}^m} \delta^{(5)}(\phi_{WD} - \phi_{WD}(\phi_{Wc}^m, z)) \\
& + \int \frac{\mathrm{d}z}{z^2} \mathrm{d}\phi_{Wc}^0 \, f_a(x_a, \mu^2) \, f_b(x_b, \mu^2) \, \times \, \frac{\mathrm{d}\hat{\sigma}_{ab\to Wc}^{(0)}}{\mathrm{d}\phi_{Wc}^0} \\
& \times \left\{ D(z, \mu^2)_{c/D} - D(z, \mu_0^2)_{c/D} \right\} \delta^{(5)}(\phi_{WD} - \phi_{WD}(\phi_{Wc}^0, z)) \,.
\end{aligned} \tag{3.43}
$$

Notice that $D(z, \mu_0^2)_{c/D}$ is interpreted as the un-evolved fragmentation function.

The numerical calculation was implemented using GenEvA [111],[112],[113], a Monte-Carlo event generator with several advantages over other event generators, mainly: a novel method of phase space calculation that avoids double counting of phase space regions and a natural scale matching mechanism. The results generated here were run on a compute cluster at Lawrence Berkeley National Lab. The center of mass energy of the hadronic collisions $E_{cm} = 8\,\mathrm{TeV}$ and the parton distribution functions used were the CT10NLO set, [114].
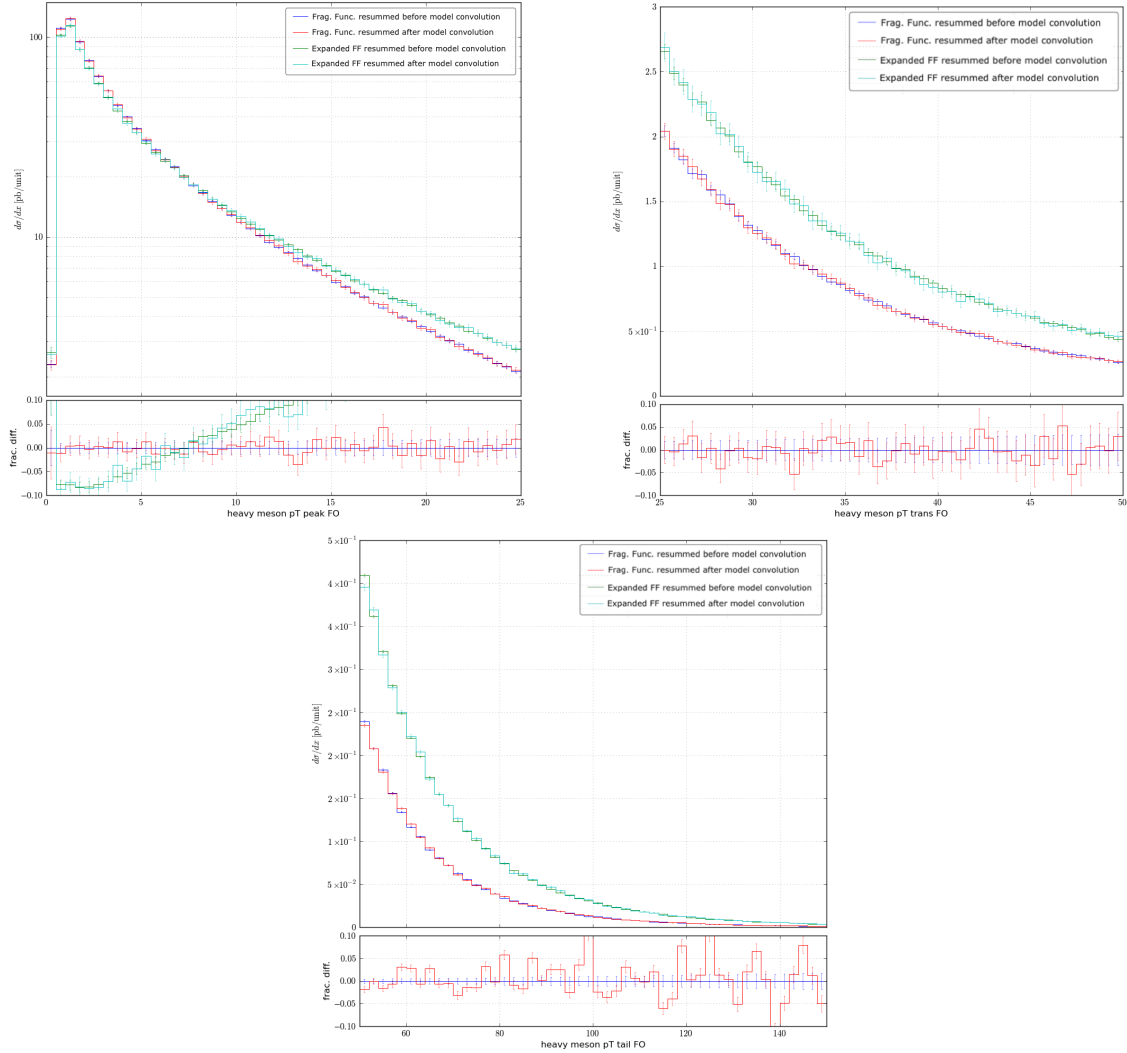
Figure 3.2: Plots of three ranges of cross sections with respect to heavy meson p_T. (Red curve): Resummed cross section with non-perturbative model convolution occurring after cross section calculation (Blue curve): Resummed cross section with non-perturbative model convolution occurring before resummation and cross section calculation (Cyan curve): Resummed cross section using fragmentation function expanded to leading order with non-perturbative model convolution occurring after cross section calculation (Green curve): Resummed cross section using fragmentation function expanded to leading order with non-perturbative model convolution occurring before resummation and cross section calculation

Before analysis of the full numerical result it is good to notice an important check on the resummation method and the numerical implementation itself. Because the Mellin method for resummation allowed for numerical convergence without a non-perturbative model, we can add back the convolution of this model to a calculation, which used the partonic fragmen-

tation function in Eq. (3.43), but now doing the convolution after the cross section has been calculated. This was done by multiplying the cross section by the non-perturbative model when the differential cross sections were being calculated with respect to various observables. In other words, the weights of the observables were multiplied by the non-perturbative model before binning into histograms. This is a subtle difference but it yields a result necessary for ensuring the non-perturbative models applied to calculations are correctly implemented. In Figure 3.2 the plotted quantities are as follows: The red and blue curves are the fully resummed cross sections while the green and cyan curves are the resummed cross sections expanded to leading-order. The blue and green curves, however, were calculated using the fragmentation function convolved with a non-perturbative model before resummation. The red and cyan curves, on the other hand, were calculated by first calculating the cross section using a fragmentation function resummed without a model, then those cross sections were convolved with a model before generating the plots differential in an observable, in this case p_T of the heavy meson. To within numerical uncertainty, these curves agree and this should give us confidence that: 1.) The two methods of resummation agree on the running fragmentation function and 2.) We have correctly numerically implemented the non-perturbative model convolution needed in later calculations.
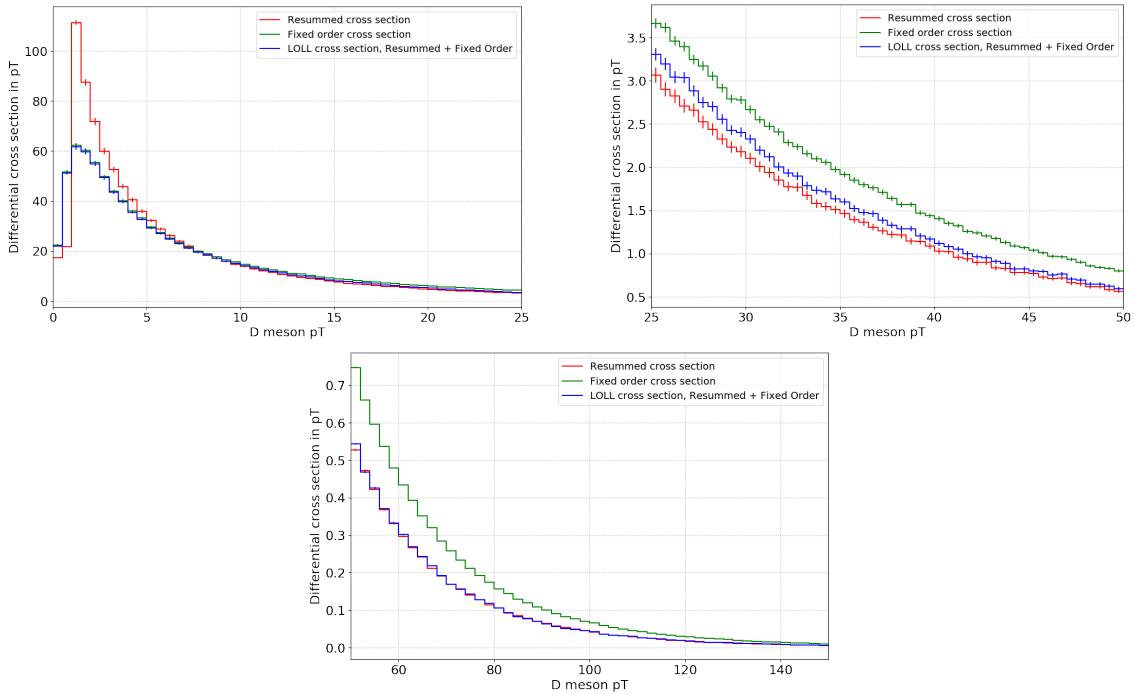

Figure 3.3: Plots of three ranges of cross sections with respect to heavy meson p_T. (Blue curve): LO+LL cross section (Green curve): Massive charm cross section (Red curve): Resummed cross section

Figure 3.3 shows the results of a full leading order plus leading log calculation. Because

heavy meson p_T is of importance to experimentalists and it is one of the defining scales of the underlying physics, we plot $\frac{d\sigma}{dp_T}$ to assess the calculations validity in various regions of phase space. In this implementation the method that was used to ensure the merged fixed-order plus resummed cross sections was that of the suppression function in Eq. (3.11). The main takeaways from Figure 3.3 are as follows: 1.) The full LOLL cross section reproduces the massive cross section at low p_T 2.) The full LOLL cross section reproduces the resummed cross section at high p_T 3.) The two cross sections are smoothly merged together with the help of the suppression function.

3.5 Future inclusion of NLO QCD corrections

Although not numerically implemented in this work, we present all the necessary components for a full NLO + NLL calculation. We begin with the matching of partonic cross section coefficients and follow with explicit derivation of several subtractions and finite contributions.

3.5.1 Matching coefficients

In the following we demonstrate the procedure for matching partonic to hadronic states in a straightforward, QCD approach. Because the fixed order calculation is carried out maintaining a massive charm quark, it is referred to as the "massive calculation". In the resummed calculation, on the other hand, a massless charm is used in the resummation process and so it is referred to as the "massless calculation". This is to ovoid confusion in our naming convention, as a massless calculation can be carried out to fixed order.

3.5.1.1 Fixed order matching

In the following section we calculate the various components of the coefficients, $d\hat{\sigma}$, by calculating initial partonic states with parton distribution functions and expanding to the desired order.

In the case of leading order matching in the massive calculation the zeroth order term is simply

$$\frac{d\hat{\sigma}_{ab\to Wc}}{d\phi_{Wc}^m} = \frac{d\hat{\sigma}_{ab\to Wc}^{(0)}}{d\phi_{Wc}^m} . \tag{3.44}$$

At next-to-leading order the PDFs can be written as

$$f_{ia}(x) = \delta_{ia}\,\delta(1-x) - \frac{\alpha_s}{2\pi}\left(\frac{1}{\epsilon}P_{ia}(x) - K_{ia}(x) + \mathcal{O}(\alpha_s^2)\right) \tag{3.45}$$

where $P_{ia}(x)$ are the Altarelli-Parisi spitting kernels. In the usual $\overline{\text{MS}}$ subtraction scheme, $K_{ia}(x) = 0$, [115].

Expanding Eq. (3.3) to next-to-leading order the cross section is now

$$\frac{\mathrm{d}\hat{\sigma}^{(1)}_{ab\to Wc}}{\mathrm{d}\phi^m_{Wc}} = \frac{\mathrm{d}\hat{\sigma}^{FO(1)}_{ab\to Wc}}{\mathrm{d}\phi^m_{Wc}}(x_a, x_b)+$$
$$\frac{1}{\epsilon}\frac{\alpha_s}{2\pi}\int \mathrm{d}z \sum_i \left[\frac{\mathrm{d}\hat{\sigma}^{(0)}_{ib\to Wc}}{\mathrm{d}\phi^m_{Wc}}(zx_a, x_b)P_{ia}(z) + \frac{\mathrm{d}\hat{\sigma}^{(0)}_{ai\to Wc}}{\mathrm{d}\phi^m_{Wc}}(x_a, zx_b)P_{ib}(z)\right]. \tag{3.46}$$

To continue in the calculation we determine $\mathrm{d}\hat{\sigma}^{FO(1)}$ by writing

$$\frac{\mathrm{d}\hat{\sigma}^{FO(1)}_{ab\to Wc}}{\mathrm{d}\phi^m_{Wc}} = \frac{\mathrm{d}\hat{\sigma}^V_{ab\to Wc}}{\mathrm{d}\phi^m_{Wc}} + \int \sum_j \mathrm{d}\phi_{rad}\frac{\mathrm{d}\hat{\sigma}^R_{ab\to Wcj}}{\mathrm{d}\phi^m_{Wcj}}\frac{\phi^m_{Wcj}}{\mathrm{d}\phi^m_{Wc}\mathrm{d}\phi_{rad}} \tag{3.47}$$

and the new phase space measure for 3-body final states is

$$\mathrm{d}\phi^m_{Wcj} \equiv \mathrm{d}x_a\mathrm{d}x_b\frac{\mathrm{d}^3p_W}{(2\pi)^3 2E_W}\frac{\mathrm{d}^3p_c}{(2\pi)^3 2E_c}\frac{\mathrm{d}^3p_j}{(2\pi)^3 2E_j}(2\pi)^4\delta^{(4)}(k_a + k_b - p_W - p_c - p_j), \tag{3.48}$$

where $\mathrm{d}\sigma^V$ is the contribution from 2-to-2 loop diagrams, which include so-called bubble, triangle and box diagrams. The bubble and triangle diagrams are both UV and IR divergent while the box diagrams are only IR divergent. The UV divergences in $\mathrm{d}\sigma^V$'s bubble diagrams are canceled out by appropriate mass renormalization counter-terms while the UV divergences in the triangle diagrams are canceled out by charge renormalization counter-terms. From now on the term $\mathrm{d}\sigma^V$ is assumed to have UV divergences canceled so only IR singularities remain. These singularities will be canceled by terms in the expansion of the PDF's and real emission cross section. While for an IR safe observable the singularities in $\mathrm{d}\sigma^V$ are canceled by terms in $\mathrm{d}\sigma^R$, this cancellation is not trivial and lead to the main difficulty in higher order QCD calculations. This is due to the fact that the cancellations in Eq. (3.47) occur after integration over $\mathrm{d}\sigma^R$. This means they arise from different phase spaces and cannot cancel one-another out before numerical calculation. In order to proceed with a numerical implementation, the divergences in Eq. (3.47) must be made regular by a suitable subtraction method. Using the FKS subtraction formalism, [22], we write

$$0 = \int \mathrm{d}\phi^m_{Wcj} \left[\frac{\mathrm{d}\sigma^S_{ab \to Wcj}}{\mathrm{d}\phi^m_{Wcj}} - \frac{\mathrm{d}\sigma^S_{ab \to Wcj}}{\mathrm{d}\phi^m_{Wcj}} \right]$$

$$= \int \mathrm{d}\phi^m_{Wcj} \frac{\mathrm{d}\sigma^S_{ab \to Wcj}}{\mathrm{d}\phi^m_{Wcj}} - \int \mathrm{d}\phi^m_{Wc}\mathrm{d}\phi_{rad} \frac{\phi^m_{Wcj}}{\phi^m_{Wc}\phi_{rad}} \frac{\mathrm{d}\sigma^S_{ab \to Wcj}}{\mathrm{d}\phi^m_{Wcj}}$$

$$= \int \mathrm{d}\phi^m_{Wcj} \frac{\mathrm{d}\sigma^S_{ab \to Wcj}}{\mathrm{d}\phi^m_{Wcj}} - \int \mathrm{d}\phi^m_{Wc} \frac{\mathrm{d}\sigma^I_{ab \to Wc}}{\mathrm{d}\phi^m_{Wc}} \tag{3.49}$$

with

$$\frac{\mathrm{d}\sigma^I_{ab \to Wc}}{\mathrm{d}\phi^m_{Wc}} = \int \mathrm{d}\phi_{rad} \frac{\phi^m_{Wcj}}{\phi^m_{Wc}\phi_{rad}} \frac{\mathrm{d}\sigma^S_{ab \to Wcj}}{\mathrm{d}\phi^m_{Wcj}} . \tag{3.50}$$

Adding Eq. (3.49) to Eq. (3.47), for an infrared safe observable $\mathcal{O}$

$$\frac{\mathrm{d}\hat{\sigma}^{FO(1)}_{ab \to Wc}}{\mathrm{d}\mathcal{O}} = \int \mathrm{d}\phi^m_{Wc} \left[\frac{\mathrm{d}\hat{\sigma}^V_{ab \to Wc}}{\mathrm{d}\phi^m_{Wc}} + \frac{\mathrm{d}\hat{\sigma}^I_{ab \to Wc}}{\mathrm{d}\phi^m_{Wc}} \right] \delta(\mathcal{O} - \mathcal{O}(\phi^m_{Wc}))$$

$$+ \int \sum_j \mathrm{d}\phi_{rad}\mathrm{d}\phi^m_{Wc} \frac{\phi^m_{Wcj}}{\mathrm{d}\phi^m_{Wc}\mathrm{d}\phi_{rad}} \left[\frac{\mathrm{d}\hat{\sigma}^R_{ab \to Wcj}}{\mathrm{d}\phi^m_{Wcj}} - \frac{\mathrm{d}\hat{\sigma}^S_{ab \to Wcj}}{\mathrm{d}\phi^m_{Wcj}} \right] \delta(\mathcal{O} - \mathcal{O}(\phi^m_{Wcj})). \tag{3.51}$$

3.5.1.2   Resummed matching

As with the zeroth order massive matching, the massless term is also simply

$$\frac{\mathrm{d}\hat{\sigma}_{ab \to Wc}}{\mathrm{d}\phi^0_{Wc}} = \frac{\mathrm{d}\hat{\sigma}^{(0)}_{ab \to Wc}}{\mathrm{d}\phi^0_{Wc}} . \tag{3.52}$$

In the case where the charm can be considered massless, as with the massive calculation, the PDFs are needed to absorb initial state singularities, however; now there is a new final state collinear singularity, that is absorbed into the fragmentation function. The fragmentation function, to the order we are working to, is written

$$D_{ij}(x) = \delta_{ij}\,\delta(1 - x) - \frac{\alpha_s}{2\pi} \left(\frac{1}{\epsilon} P_{ij}(x) + \mathcal{O}(\alpha_s^2) \right) . \tag{3.53}$$

Now Eq. (3.46) is modified by the addition of the fragmentation function

$$
\frac{\mathrm{d}\hat{\sigma}_{ab\to Wc}^{(1)}}{\mathrm{d}\phi_{Wc}^0} = \frac{\mathrm{d}\hat{\sigma}_{ab\to Wc}^{FO(1)}}{\mathrm{d}\phi_{Wc}^0}(x_a, x_b) + \frac{1}{\epsilon}\frac{\alpha_s}{2\pi}\left\{ \frac{\mathrm{d}\hat{\sigma}_{ab\to Wc}^{(0)}}{\mathrm{d}\phi_{Wc}^0(z)}(x_a, x_b)P_{qc}(z) \right.
$$

$$
\left. \int \mathrm{d}s \sum_i \left[\frac{\mathrm{d}\hat{\sigma}_{ib\to Wc}^{(0)}}{\mathrm{d}\phi_{Wc}^0}(zx_a, x_b)P_{ia}(z) + \frac{\mathrm{d}\hat{\sigma}_{ai\to Wc}^{(0)}}{\mathrm{d}\phi_{Wc}^0}(x_a, zx_b)P_{ib}(z) \right] \right\}. \tag{3.54}
$$

3.5.1.3   Collinear subtraction

Here we calculate the initial state collinear subtraction term with the method of [115] by first using the common parametrization of the momentum of the radiated parton j

$$
p_j = \frac{\xi_j\sqrt{s}}{2}\left(1, \frac{2\overrightarrow{p_\perp}}{\sqrt{s}}, y_j\right) \tag{3.55}
$$

where the new variables are

$$
\xi_j = \frac{2E_j}{\sqrt{s}}, \qquad y_j = \cos\theta_j, \quad. \tag{3.56}
$$

So that soft singularities correspond to $\xi \to 0$ and collinear singularities correspond to $y \to \pm 1$. This means that all infrared divergences of the final state parton j are recreated by the term

$$
\frac{\mathrm{d}\sigma_{ab\to Wcj}^{(S)}}{\mathrm{d}\phi_{Wcj}^m} = \lim_{\xi\to 0}\frac{\mathrm{d}\sigma_{ab\to Wcj}^{(1)}}{\mathrm{d}\phi_{Wcj}^m} + \lim_{y\to 1}\frac{\mathrm{d}\sigma_{ab\to Wcj}^{(1)}}{\mathrm{d}\phi_{Wcj}^m} + \lim_{y\to -1}\frac{\mathrm{d}\sigma_{ab\to Wcj}^{(1)}}{\mathrm{d}\phi_{Wcj}^m}
$$

$$
- \lim_{\substack{\xi\to 0\\ y\to 1}}\frac{\mathrm{d}\sigma_{ab\to Wcj}^{(1)}}{\mathrm{d}\phi_{Wcj}^m} - \lim_{\substack{\xi\to 0\\ y\to -1}}\frac{\mathrm{d}\sigma_{ab\to Wcj}^{(1)}}{\mathrm{d}\phi_{Wcj}^m}
$$

$$
\equiv \frac{\mathrm{d}\sigma_{ab\to Wcj}^{\mathrm{SOFT}}}{\mathrm{d}\phi_{Wcj}^m} + \frac{\mathrm{d}\sigma_{ab\to Wcj}^{\mathrm{COLL}_A}}{\mathrm{d}\phi_{Wcj}^m} + \frac{\mathrm{d}\sigma_{ab\to Wcj}^{\mathrm{COLL}_B}}{\mathrm{d}\phi_{Wcj}^m}, \tag{3.57}
$$

with the additional definitions

$$
\begin{aligned}
\frac{\mathrm{d}\sigma_{ab\to Wcj}^{\text{SOFT}}}{\mathrm{d}\phi_{Wcj}^m} &= \lim_{\xi\to 0} \frac{\mathrm{d}\sigma_{ab\to Wcj}^{(1)}}{\mathrm{d}\phi_{Wcj}^m} \\
\frac{\mathrm{d}\sigma_{ab\to Wcj}^{\text{COLL}_A}}{\mathrm{d}\phi_{Wcj}^m} &= \lim_{y\to 1} \frac{\mathrm{d}\sigma_{ab\to Wcj}^{(1)}}{\mathrm{d}\phi_{Wcj}^m} - \lim_{\substack{\xi\to 0 \\ y\to 1}} \frac{\mathrm{d}\sigma_{ab\to Wcj}^{(1)}}{\mathrm{d}\phi_{Wcj}^m} \\
\frac{\mathrm{d}\sigma_{ab\to Wcj}^{\text{COLL}_B}}{\mathrm{d}\phi_{Wcj}^m} &= \lim_{y\to -1} \frac{\mathrm{d}\sigma_{ab\to Wcj}^{(1)}}{\mathrm{d}\phi_{Wcj}^m} - \lim_{\substack{\xi\to 0 \\ y\to -1}} \frac{\mathrm{d}\sigma_{ab\to Wcj}^{(1)}}{\mathrm{d}\phi_{Wcj}^m} \,.
\end{aligned}
\tag{3.58}
$$

As in [115], the $\mathrm{d}\sigma^{\text{COLL}}$'s can be calculated by

$$
\frac{\mathrm{d}\sigma_{ab\to Wcj}^{\text{COLL}_A}}{\mathrm{d}\phi_{Wcj}^m} = \sum_j \frac{4\pi\alpha_s\mu^{2\epsilon}}{p_j\cdot k_a} P_{aj}(z,\epsilon)\frac{\mathrm{d}\sigma_{ab\to Wc}^{(0)}}{\mathrm{d}\phi_{Wc}^m}\,,
\tag{3.59}
$$

with $P_{aj}(z,\epsilon)$ as the Altarelli-Parisi splitting kernels, away from one and in $d = 4 - 2\epsilon$ dimensions.
Using

$$
\mathrm{d}\phi_{Wcj}^m = \frac{1}{2(2\pi)^{3-2\epsilon}}\left(\frac{s}{4}\right)^{1-\epsilon}\xi_j^{1-2\epsilon}(1-y_j^2)^{-\epsilon}\,\mathrm{d}\xi_j\,\mathrm{d}y_j\,\mathrm{d}\Omega_{2-2\epsilon}\,\mathrm{d}\phi_{Wc}^m
\tag{3.60}
$$

one can show that

$$
\begin{aligned}
\int \mathrm{d}\phi_{Wcj}^m &\frac{\mathrm{d}\sigma_{ab\to Wcj}^{\text{COLL}_A}}{\mathrm{d}\phi_{Wcj}^m}\delta(\phi_{Wc}^m - \phi_{Wc}^m(\phi_{Wcj}^m)) \\
&= \frac{\alpha_s}{2\pi}\int \mathrm{d}z\left\{\sum_j (1-z)P_{aj}(z,0)\left[2\left[\frac{\log(1-z)}{1-z}\right]_+ - \left[\frac{\log\frac{\mu^2}{s}}{1-z}\right]_+\right.\right. \\
&\left.\left. \qquad -\frac{1}{\epsilon}\left[\frac{1}{1-z}\right]_+ - P_{aj}'(z,\epsilon)\Bigg|_{\epsilon=0}\right]\right\}\frac{\mathrm{d}\sigma_{ab\to Wc}^{(0)}}{\phi_{Wc}^m}(zx_a,x_b)\,.
\end{aligned}
\tag{3.61}
$$

An analogous formula can be calculated in the same manner for $\mathrm{d}\sigma^{\text{COLL}_B}$, while the soft subtraction term is not presented here but can be found in [115]. With these subtraction pieces the full NLO differential cross section can be calculated.

As for the resummed calculation, all previous subtraction methods are carried over to the massless regime with the addition of the subtraction of final state collinear singularities.

3.5.2 Partonic cross sections

3.5.2.1 Fixed order cross sections

The Born cross section is easy to calculate in the massive case, and we turn to stating several of the next-to-leading order contributions to the massive cross section. After using the appropriate subtractions the remaining finite pieces of the cross section are given as follows

$$
\frac{\mathrm{d}\hat{\sigma}^{(1)}_{ab\to Wc}}{\mathrm{d}\phi^m_{Wc}}(x_a, x_b) = \frac{\mathrm{d}\sigma^{\mathrm{VIRT},finite}_{ab\to Wc}}{\mathrm{d}\phi^m_{Wc}} + \frac{\mathrm{d}\sigma^{\mathrm{SOFT},finite}_{ab\to Wc}}{\mathrm{d}\phi^m_{Wc}}
$$
$$
+ \frac{\mathrm{d}\sigma^{\mathrm{COLL}_A,finite}_{ab\to Wc}}{\mathrm{d}\phi^m_{Wc}} + \frac{\mathrm{d}\sigma^{\mathrm{COLL}_B,finite}_{ab\to Wc}}{\mathrm{d}\phi^m_{Wc}} + \frac{\mathrm{d}\sigma^{\mathrm{REAL},finite}_{ab\to Wc}}{\mathrm{d}\phi^m_{Wc}} . \tag{3.62}
$$

The finite piece of the virtual diagrams was calculated and validated with FORM and the Mathematica package FormCalc + LoopTools. The formula for the virtual matrix elements are too lengthy to present in full but are straightforward to calculate in one of many NLO programs. The finite contribution from the soft subtraction is

$$
\frac{\mathrm{d}\sigma^{\mathrm{SOFT},finite}_{ab\to Wc}}{\mathrm{d}\phi^m_{Wc}} = \frac{\alpha_s}{2\pi} \frac{\mathrm{d}\hat{\sigma}^{(0)}_{ab\to Wc}}{\mathrm{d}\phi^m_{Wc}}(x_a, x_b) \left\{ (C_A + C_F) \left(\frac{1}{2} \log^2 \frac{\mu^2}{s} - \frac{\pi^2}{6} \right) \right.
$$
$$
+ C_F \left(-\log \frac{\mu^2}{s} \log \frac{(m_c^2 - u)^2}{sm_c^2} - I_\varepsilon(u) + \log \frac{\mu^2}{s} + \frac{1}{\beta} \log \frac{1+\beta}{1-\beta} \right)
$$
$$
\left. + C_A \left(\log \frac{\mu^2}{s} \log \frac{m_c^2 - u}{m_c^2 - t} + \frac{1}{2} I_\varepsilon(u) - \frac{1}{2} I_\varepsilon(t) \right) \right\}, \tag{3.63}
$$

with

$$
I_\varepsilon(x) = -2 \left(\frac{1}{4} \log^2 \frac{1-\beta}{1+\beta} + \log \left(\frac{m_c^2 - x}{\sqrt{s}E_c} \frac{1}{1+\beta} \right) \log \left(\frac{m_c^2 - x}{\sqrt{s}E_c} \frac{1}{1-\beta} \right) \right.
$$
$$
\left. + \mathrm{Li}_2 \left(1 - \frac{m_c^2 - x}{\sqrt{s}E_c(1+\beta)} \right) + \mathrm{Li}_2 \left(1 - \frac{m_c^2 - x}{\sqrt{s}E_c(1-\beta)} \right) \right), \tag{3.64}
$$

where $\beta = \sqrt{1 - m_c^2/E_c^2}$, and in the partonic center of mass frame, $E_c = (s + m_c^2 - m_W^2)/(2\sqrt{s})$.

After subtraction the finite initial state collinear pieces are

$$
\frac{\mathrm{d}\sigma_{ab\to Wc}^{\text{COLL}_A,finite}}{\mathrm{d}\phi_{Wc}^m} = \frac{\alpha_s}{2\pi}\int \mathrm{d}z \frac{\mathrm{d}\sigma_{jb\to Wc}^{(0)}}{\phi_{Wc}^m}(zx_a, x_b)\Bigg\{\sum_j (1-z)P_{aj}(z,0)\left[2\left[\frac{\log(1-z)}{1-z}\right]_+\right.
$$
$$
\left.-\left[\frac{\log\frac{\mu^2}{s}}{1-z}\right]_+ - P'_{aj}(z,\epsilon)\bigg|_{\epsilon=0}\right]\Bigg\}
$$
$$
\frac{\mathrm{d}\sigma_{ab\to Wc}^{\text{COLL}_B,finite}}{\mathrm{d}\phi_{Wc}^m} = \frac{\alpha_s}{2\pi}\int \mathrm{d}z \frac{\mathrm{d}\sigma_{aj\to Wc}^{(0)}}{\phi_{Wc}^m}(x_a, zx_b)\Bigg\{\sum_j (1-z)P_{bj}(z,0)\left[2\left[\frac{\log(1-z)}{1-z}\right]_+\right.
$$
$$
\left.-\left[\frac{\log\frac{\mu^2}{s}}{1-z}\right]_+ - P'_{bj}(z,\epsilon)\bigg|_{\epsilon=0}\right]\Bigg\}. \tag{3.65}
$$

Explicitly taking the Altarelli-Parisi splitting functions and inserting into the general collinear subtraction form (3.65), the qg and gg splitting channel finite contributions are

$$
\frac{\mathrm{d}\sigma_{ab\to Wc}^{\text{COLL}_A,finite}}{\mathrm{d}\phi_{Wc}^m} = C_F\frac{\alpha_s}{2\pi}\int \mathrm{d}z \frac{\mathrm{d}\sigma_{ab\to Wc}^{(0)}}{\phi_{Wc}^m}(zx_a, x_b)\Bigg\{(1-z)+2(1+z^2)\left[\frac{\log(1-z)}{1-z}_+\right]
$$
$$
-(1+z^2))\left[\frac{1}{1-z_+}\right]\log\frac{\mu^2}{s}\Bigg\} \tag{3.66}
$$

and

$$
\frac{\mathrm{d}\sigma_{ab\to Wc}^{\text{COLL}_B,finite}}{\mathrm{d}\phi_{Wc}^m} = C_A\frac{\alpha_s}{\pi}\int \mathrm{d}z\, z\frac{\mathrm{d}\sigma_{ab\to Wc}^{(0)}}{\phi_{Wc}^m}(x_a, zx_b)\Bigg\{\left[\frac{\log(1-z)^2 s/\mu^2}{1-z}_+\right]
$$
$$
+(1-z)\left(\frac{1}{z}+z\right)\log((1-z^2)s/\mu^2)\Bigg\}. \tag{3.67}
$$

Finally, the finite real contribution is given by

$$
\frac{\mathrm{d}\sigma_{ab\to Wc}^{\text{REAL},finite}}{\mathrm{d}\phi_{Wc}^m} = \int \mathrm{d}\phi_{rad}\frac{\phi_{Wcj}^m}{\mathrm{d}\phi_{Wc}^m \mathrm{d}\phi_{rad}}\left[\frac{\mathrm{d}\hat{\sigma}_{ab\to Wcj}^R}{\mathrm{d}\phi_{Wcj}^m} - \frac{\mathrm{d}\sigma_{mn\to Wcj}^{(S)}}{\mathrm{d}\phi_{Wcj}^m}\right]\delta(\phi_{Wc}^m - \phi_{Wc}^m(\phi_{Wcj}^m)). \tag{3.68}
$$

Now all finite next-to-leading order pieces, Eq. (3.62) can be combined with the leading order cross section, Eq. (3.44) to give a full NLO cross section.

3.5.2.2 Resummed cross sections

The Born, and initial state subtraction calculations are carried out in the same manner in the massless case as in the massive case. With the finite massless integrated soft subtraction piece being

$$
\frac{\mathrm{d}\sigma_{ab\to Wc}^{\mathrm{SOFT},finite}}{\mathrm{d}\phi_{Wc}^0} = \frac{\alpha_s}{2\pi} \frac{\mathrm{d}\hat{\sigma}_{ab\to Wc}^{(0)}}{\mathrm{d}\phi_{Wc}^0}(x_a, x_b) \Bigg\{ (C_A + 2C_F)\left(\frac{1}{2}\log^2\frac{\mu^2}{s} - \frac{\pi^2}{6}\right)
$$
$$
- 2C_F\left(-\log\frac{\mu^2}{s}\log\frac{(-u)^2}{s-m_W^2} - \mathrm{Li}_2\left(-\frac{t}{u}\right)\right)
$$
$$
+ C_A\left(\log\frac{\mu^2}{s}\log\frac{u}{t} + \mathrm{Li}_2\left(-\frac{t}{u}\right) - \mathrm{Li}_2\left(-\frac{u}{t}\right)\right) \Bigg\}. \tag{3.69}
$$

An important factor, not in the massive case as discussed above, is the final state collinear subtraction and finite contribution to the cross section. In the massive case, Eq. (3.68), the subtraction term $d\sigma^{(S)}$, is calculated by the usual method in [115], while for the massless case a subtle modification is required. In Ref. [115], the authors assume a generic jet function/algorithm that regulates final state divergences associated with collinear radiation. This function is not present in this case as the final state logarithms are being resummed by fragmentation function evolution. So now when numerically implementing Eq. (3.68), these collinear divergences are regulated with plus distributions. However, because the collinear region of phase space of the cross section is being modified, an extra term, called the collinear remnant, must be added back to recover the full cross section. This takes the form of

$$
R_{CR} = C_F \int \frac{dz}{z^2}\Bigg[(1-z) + 2(1+z^2)\left[\frac{\log(1-z)}{1-z}\right]_+
$$
$$
+ (1+z^2)\frac{1}{(1-z)_+}\log\left(\frac{4E_c^2}{\mu_F^2}\frac{y_{cut}}{2}\right)\Bigg], \tag{3.70}
$$

where E_c is the charm quark energy, μ_F^2 is the fragmentation factorization scale and y_{cut} is the cutoff of the collinear plus functions used to regulate divergences in Eq. (3.68).

So that the contribution of the collinear remnant to the total cross section is

$$
\frac{\mathrm{d}\sigma_{ab\to Wc}^{\mathrm{COLL}c,finite}}{\mathrm{d}\phi_{Wc}^0} = \frac{\alpha_s}{2\pi}\int \sum_i \frac{dz}{z^2} R_{CR}\, D_{i/D}(z,\mu^2)\frac{\mathrm{d}\hat{\sigma}_{ab\to Wi}^{(0)}}{\mathrm{d}\phi_{Wc}^0}(x_m, x_n)
$$

$$
\tag{3.71}
$$

and collecting all terms

$$\frac{\mathrm{d}\hat{\sigma}^{(1)}_{ab \to Wc}}{\mathrm{d}\phi^0_{Wc}}(x_a, x_b) = \frac{\mathrm{d}\sigma^{\mathrm{VIRT},finite}_{ab \to Wc}}{\mathrm{d}\phi^0_{Wc}} + \frac{\mathrm{d}\sigma^{\mathrm{SOFT},finite}_{ab \to Wc}}{\mathrm{d}\phi^0_{Wc}} + \frac{\mathrm{d}\sigma^{\mathrm{COLL}_A,finite}_{ab \to Wc}}{\mathrm{d}\phi^0_{Wc}}$$
$$+ \frac{\mathrm{d}\sigma^{\mathrm{COLL}_B,finite}_{ab \to Wc}}{\mathrm{d}\phi^0_{Wc}} + \frac{\mathrm{d}\sigma^{\mathrm{COLL}_c,finite}_{ab \to Wc}}{\mathrm{d}\phi^0_{Wc}} + \frac{\mathrm{d}\sigma^{\mathrm{REAL},finite}_{ab \to Wc}}{\mathrm{d}\phi^0_{Wc}} . \tag{3.72}$$

3.5.3 Future Outlook

What we have presented is a way forward to include NLO QCD corrections to W+charm processes. By taking Eqs. (3.3), (3.6), (3.8) and keeping next-to-leading order terms, one can show that now

$$\frac{\mathrm{d}\sigma^{NLONLL}}{\mathrm{d}\phi_{WD}} = \sum_{a,b} \int \frac{\mathrm{d}z}{z^2} D(z, \mu^2)^{NP}_{c/D} \mathrm{d}\phi^m_{Wc} f_a(x_a, \mu^2) \, f_b(x_b, \mu^2)$$
$$\times \left(\frac{\mathrm{d}\hat{\sigma}^{(0)}_{ab \to Wc}}{\mathrm{d}\phi^m_{Wc}} + \frac{\alpha_s}{2\pi} \frac{\mathrm{d}\hat{\sigma}^{(1)}_{ab \to Wc}}{\mathrm{d}\phi^m_{Wc}} \right) \delta^{(5)}(\phi_{WD} - \phi_{WD}(\phi^m_{Wc}, z))$$
$$+ \int \frac{\mathrm{d}z}{z^2} \mathrm{d}\phi^0_{Wc} f_a(x_a, \mu^2) \, f_b(x_b, \mu^2) \times \left\{ D(z, \mu^2)_{c/D} - D(z, \mu_0^2)_{c/D} \right\}$$
$$\times \left(\frac{\mathrm{d}\hat{\sigma}^{(0)}_{ab \to Wc}}{\mathrm{d}\phi^0_{Wc}} + \frac{\alpha_s}{2\pi} \frac{\mathrm{d}\hat{\sigma}^{(1)}_{ab \to Wc}}{\mathrm{d}\phi^0_{Wc}} \right) \delta^{(5)}(\phi_{WD} - \phi_{WD}(\phi^0_{Wc}, z)) \tag{3.73}$$

where each component needed for the calculation is presented above.

With a suitable codebase for collecting terms and integrating Eq. (3.73) one should be able to achieve NLO precision in this process. It is useful to note that this approach to include NLO corrections to heavy meson production is now fully differential in the final W plus D meson cross section. This allows for analysis with heavy meson p_T, as other approaches have provided, but also has a way forward for predictions important in other experimental observables. With the ability to calculate a wide range of physical observables experimentalists can now more accurately test the Standard Model in regions of experimental phase space in which such accuracy was not possible previously.

Chapter 4

Conclusion

We have shown in this work that by utilizing the Standard Model as an effective theory we can increase the precision of theoretical predictions and set stronger bounds on the structure of new theories. With regards to the SM-EFT, our work has shown that it can be used in several ways to probe the scale of new physics. By including NLO QCD corrections to several SM-EFT operators and matching to parton showers using the `POWHEG` method, we now have new method to calculate corrections to SM processes. The resulting `POWHEG BOX V2` computer code will be made publicly available on the `powhegbox.mib.infn.it` webpage. We have presented several new constraints on SM-EFT operator coefficients extracted from Monte-Carlo event generation matching to parton shower simulations.

Some of the results can be summarized as follows: In charged and neutral current Drell-Yan processes, NLO corrections are on the order of $10-20\%$ of the leading-order calculation. These events are relatively insensitive to dipole couplings $\Gamma_{W,\gamma}^{u,d}$ and, as such, constraints on these operators are not well constrained by measurements in the high m_T^W regions of phase space. Conversely, the semi-leptonic four-fermion operators are very strongly constrained by high W transverse mass. By utilizing these stronger bounds, the scale of new physics is pushed to $\Lambda \sim 10\,TeV$. The bounds on the real parts of dimension 6 operators we have presented are comparable to the current best limits set by low-energy experiments. However, low-energy experiments, such as electric-dipole-moment measurements, set stronger limits on the imaginary parts of these coefficients. In associated production of a Higgs Boson and a W on Z boson, under some simplifying assumptions, we have constrained non-standard couplings to light quarks on the order of 10% or better in some cases. By loosening these assumptions, and allowing all operators to contribute simultaneously, constraints are indeed weakened. However, there is an upshot in that the operators most affected by this loosened assumption, contribute to a Higgs decay that is loop suppressed in the Standard Model, namely the $h \to \gamma\gamma$ and $h \to \gamma Z$ decay channels. By combining associated Higgs and W/Z production with Higgs branching ratios we still can provide a meaningful constraint on several coefficients. Lastly, in Higgs production via vector-boson-fusion we have shown that the sensitivity to SM-EFT operators is lower than in associated Higgs and W/Z production. While measurements in sector does not increase the bounds on operator coefficients, it does

provide a method for probing the flavor structure of SM-EFT operators through tagged dijet final states.

We have also demonstrated the need for more precise measurements in W+charm production and given the disparity of scales in these events a simple fixed order calculation is not adequate. In this work we show a general method for combining a fixed order QCD calculation in which the p_T of the heavy meson is low and perturbation theory holds, to a resummed calculation, where large logs that potentially spoil perturbative convergence are effectively resummed. During this method several other important concepts have been inspected. By utilizing two different methods for resummation we have validated both methods convergence as well as tested the overall consistency in the numerical implementation of the calculation. One of several ways can be used to interpolate between the fixed order and resummed calculation, resulting in a cross section that is valid in both low p_T and high p_T regimes. By using the above method we combined a leading-order QCD calculation with a QCD calculation resummed to leading-logarithm accuracy and provide a fully differential cross section that can be used to calculate a wide range of observables. A way forward to include next-to-leading order QCD corrections to W+charm events was discussed and all the necessary components provided. It is important to note that this NLO corrected cross section would still be fully differential in final state momenta, thus giving great flexibility in its uses in providing experimental predictions. Probably a more important feature of this calculation is its ability to increase theoretical bounds in a region of experimental phase space that can directly probe the strange PDF and, by extension, better constrain the theoretical uncertainty in many other Standard Model measurements.

Bibliography

[1]   M. Aaboud *et al.*, "Search for new high-mass phenomena in the dilepton final state using 36 fb^1 of proton-proton collision data at $\sqrt{s} = 13$ TeV with the ATLAS detector," *JHEP*, vol. 10, p. 182, 2017.

[2]   M. Aaboud *et al.*, "Search for a new heavy gauge boson resonance decaying into a lepton and missing transverse momentum in 36 fb^{-1} of *pp* collisions at $\sqrt{s} = 13$ TeV with the ATLAS experiment," 2017.

[3]   H. YUKAWA, "On the interaction of elementary particles. i," *Nippon Sugaku-Buturigakkwai Kizi Dai 3 Ki*, vol. 17, pp. 48–57, 1935.

[4]   M. Gell-Mann, "Symmetries of baryons and mesons," *Phys. Rev.*, vol. 125, pp. 1067–1084, Feb 1962.

[5]   B. Bjrken and S. Glashow, "Elementary particles and su(4)," *Physics Letters*, vol. 11, no. 3, pp. 255 – 257, 1964.

[6]   G. Aad *et al.*, "Observation of a new particle in the search for the Standard Model Higgs boson with the ATLAS detector at the LHC," *Phys. Lett.*, vol. B716, pp. 1–29, 2012.

[7]   F. Abe *et al.*, "Observation of top quark production in $\overline{p}p$ collisions with the collider detector at fermilab,"

[8]   S. Abachi *et al.*, "Observation of the top quark," *Phys. Rev. Lett.*, vol. 74, pp. 2632–2637, 1995.

[9]   M. Bona *et al.*, "The Unitarity Triangle Fit in the Standard Model and Hadronic Parameters from Lattice QCD: A Reappraisal after the Measurements of Delta m(s) and BR(B $\rightarrow$ tau nu(tau))," *JHEP*, vol. 10, p. 081, 2006.

[10]   J. Charles *et al.*, "Current status of the Standard Model CKM fit and constraints on $\Delta F = 2$ New Physics," *Phys. Rev.*, vol. D91, no. 7, p. 073007, 2015.

[11]   Y. Amhis *et al.*, "Averages of *b*-hadron, *c*-hadron, and τ-lepton properties as of summer 2016," 2016.

[12] R. H. Parker, C. Yu, W. Zhong, B. Estey, and H. Müller, "Measurement of the fine-structure constant as a test of the standard model," *Science*, vol. 360, no. 6385, pp. 191–195, 2018.

[13] V. Andreev *et al.*, "Measurement of Jet Production Cross Sections in Deep-inelastic ep Scattering at HERA," *Eur. Phys. J.*, vol. C77, no. 4, p. 215, 2017.

[14] C. Glasman, "Precision tests of QCD with jets and vector bosons at HERA and Teva-Tron," in *Proceedings, 34th International Conference on High Energy Physics (ICHEP 2008): Philadelphia, Pennsylvania, July 30-August 5, 2008*, 2008.

[15] P. de Jong, "Supersymmetry searches at the LHC," in *Proceedings, 32nd International Symposium on Physics in Collision (PIC 2012): Strbske Pleso, Slovakia, September 12-15, 2012*, pp. 241–254, 2012.

[16] W. Buchmüller and D. Wyler, "Effective Lagrangian Analysis of New Interactions and Flavor Conservation," *Nucl. Phys. B*, vol. 268, p. 621, 1986.

[17] B. Grzadkowski, M. Iskrzynski, M. Misiak, and J. Rosiek, "Dimension-Six Terms in the Standard Model Lagrangian," *JHEP*, vol. 1010, p. 085, 2010.

[18] E. E. Jenkins, A. V. Manohar, and M. Trott, "Renormalization Group Evolution of the Standard Model Dimension Six Operators II: Yukawa Dependence," *JHEP*, vol. 01, p. 035, 2014.

[19] E. E. Jenkins, A. V. Manohar, and M. Trott, "Renormalization Group Evolution of the Standard Model Dimension Six Operators I: Formalism and lambda Dependence," *JHEP*, vol. 10, p. 087, 2013.

[20] R. Alonso, E. E. Jenkins, A. V. Manohar, and M. Trott, "Renormalization Group Evolution of the Standard Model Dimension Six Operators III: Gauge Coupling Dependence and Phenomenology," *JHEP*, vol. 04, p. 159, 2014.

[21] P. Nason, "A New method for combining NLO QCD with shower Monte Carlo algorithms," *JHEP*, vol. 11, p. 040, 2004.

[22] S. Frixione, P. Nason, and C. Oleari, "Matching NLO QCD computations with Parton Shower simulations: the POWHEG method," *JHEP*, vol. 11, p. 070, 2007.

[23] S. Alioli, P. Nason, C. Oleari, and E. Re, "A general framework for implementing NLO calculations in shower Monte Carlo programs: the POWHEG BOX," *JHEP*, vol. 06, p. 043, 2010.

[24] S. Alioli, P. Nason, C. Oleari, and E. Re, "NLO vector-boson production matched with shower in POWHEG," *JHEP*, vol. 07, p. 060, 2008.

[25] P. Nason and C. Oleari, "NLO Higgs boson production via vector-boson fusion matched with shower in POWHEG," *JHEP*, vol. 02, p. 037, 2010.

[26] G. Luisoni, P. Nason, C. Oleari, and F. Tramontano, "$HW^{\pm}/HZ + 0$ and 1 jet at NLO with the POWHEG BOX interfaced to GoSam and their merging within MiNLO," *JHEP*, vol. 10, p. 083, 2013.

[27] S. Alioli, W. Dekens, M. Girard, and E. Mereghetti, "NLO QCD corrections to SM-EFT dilepton and electroweak Higgs boson production, matched to parton shower in POWHEG," 2018.

[28] V. Cirigliano, M. González-Alonso, and M. L. Graesser, "Non-standard Charged Current Interactions: beta decays versus the LHC," *JHEP*, vol. 02, p. 046, 2013.

[29] S. Schael *et al.*, "Precision electroweak measurements on the Z resonance," *Phys. Rept.*, vol. 427, pp. 257–454, 2006.

[30] C. Patrignani *et al.*, "Review of Particle Physics," *Chin. Phys.*, vol. C40, no. 10, p. 100001, 2016.

[31] G. D'Ambrosio, G. Giudice, G. Isidori, and A. Strumia, "Minimal flavor violation: An Effective field theory approach," *Nucl.Phys.*, vol. B645, pp. 155–187, 2002.

[32] M. Misiak and M. Munz, "Two loop mixing of dimension five flavor changing operators," *Phys. Lett.*, vol. B344, pp. 308–318, 1995.

[33] J. A. M. Vermaseren, S. A. Larin, and T. van Ritbergen, "The four loop quark mass anomalous dimension and the invariant quark mass," *Phys. Lett.*, vol. B405, pp. 327–333, 1997.

[34] G. Degrassi, E. Franco, S. Marchetti, and L. Silvestrini, "QCD corrections to the electric dipole moment of the neutron in the MSSM," *JHEP*, vol. 0511, p. 044, 2005.

[35] C. Anastasiou, L. J. Dixon, K. Melnikov, and F. Petriello, "Dilepton rapidity distribution in the Drell-Yan process at NNLO in QCD," *Phys. Rev. Lett.*, vol. 91, p. 182002, 2003.

[36] K. Melnikov and F. Petriello, "Electroweak gauge boson production at hadron colliders through O(alpha(s)**2)," *Phys. Rev.*, vol. D74, p. 114017, 2006.

[37] S. Catani, L. Cieri, G. Ferrera, D. de Florian, and M. Grazzini, "Vector boson production at hadron colliders: a fully exclusive QCD calculation at NNLO," *Phys. Rev. Lett.*, vol. 103, p. 082001, 2009.

[38] S. Dittmaier and M. Kramer, "Electroweak radiative corrections to W boson production at hadron colliders," *Phys. Rev.*, vol. D65, p. 073007, 2002.

[39] U. Baur, O. Brein, W. Hollik, C. Schappacher, and D. Wackeroth, "Electroweak radiative corrections to neutral current Drell-Yan processes at hadron colliders," *Phys. Rev.*, vol. D65, p. 033007, 2002.

[40] U. Baur and D. Wackeroth, "Electroweak radiative corrections to $p\bar{p} \to W^{\pm} \to \ell^{\pm}\nu$ beyond the pole approximation," *Phys. Rev.*, vol. D70, p. 073015, 2004.

[41] C. M. Carloni Calame, G. Montagna, O. Nicrosini, and A. Vicini, "Precision electroweak calculation of the charged current Drell-Yan process," *JHEP*, vol. 12, p. 016, 2006.

[42] S. Dittmaier and M. Huber, "Radiative corrections to the neutral-current Drell-Yan process in the Standard Model and its minimal supersymmetric extension," *JHEP*, vol. 01, p. 060, 2010.

[43] A. Karlberg, E. Re, and G. Zanderighi, "NNLOPS accurate Drell-Yan production," *JHEP*, vol. 09, p. 134, 2014.

[44] S. Alioli, C. W. Bauer, C. Berggren, F. J. Tackmann, and J. R. Walsh, "Drell-Yan production at NNLL+NNLO matched to parton showers," *Phys. Rev.*, vol. D92, no. 9, p. 094020, 2015.

[45] S. Hoche, Y. Li, and S. Prestel, "Drell-Yan lepton pair production at NNLO QCD with parton showers," *Phys. Rev.*, vol. D91, no. 7, p. 074015, 2015.

[46] S. Alioli *et al.*, "Precision studies of observables in $pp \to W \to \ell\nu_l$ and $pp \to \gamma, Z \to \ell^{+}\ell^{-}$ processes at the LHC," *Eur. Phys. J.*, vol. C77, no. 5, p. 280, 2017.

[47] I. Brivio, Y. Jiang, and M. Trott, "The SMEFTsim package, theory and tools," *JHEP*, vol. 12, p. 070, 2017.

[48] I. Brivio and M. Trott, "The Standard Model as an Effective Field Theory," 2017.

[49] M. Farina, G. Panico, D. Pappadopulo, J. T. Ruderman, R. Torre, and A. Wulzer, "Energy helps accuracy: electroweak precision tests at hadron colliders," *Phys. Lett.*, vol. B772, pp. 210–215, 2017.

[50] A. Greljo and D. Marzocca, "High-p_T dilepton tails and flavor physics," *Eur. Phys. J.*, vol. C77, no. 8, p. 548, 2017.

[51] S. Alioli, M. Farina, D. Pappadopulo, and J. T. Ruderman, "Catching a New Force by the Tail," *Phys. Rev. Lett.*, vol. 120, no. 10, p. 101801, 2018.

[52] S. Alioli, V. Cirigliano, W. Dekens, J. de Vries, and E. Mereghetti, "Right-handed charged currents in the era of the Large Hadron Collider," *JHEP*, vol. 05, p. 086, 2017.

[53] R. Contino, A. Falkowski, F. Goertz, C. Grojean, and F. Riva, "On the Validity of the Effective Field Theory Approach to SM Precision Tests," *JHEP*, vol. 07, p. 144, 2016.

[54] J. Butterworth *et al.*, "PDF4LHC recommendations for LHC Run II," *J. Phys.*, vol. G43, p. 023001, 2016.

[55] S. Chatrchyan *et al.*, "Search for new physics in final states with a lepton and missing transverse energy in pp collisions at the LHC," *Phys. Rev.*, vol. D87, no. 7, p. 072005, 2013.

[56] G. Aad *et al.*, "Search for high-mass dilepton resonances in pp collisions at $\sqrt{s} = 8\text{TeV}$ with the ATLAS detector," *Phys. Rev.*, vol. D90, no. 5, p. 052005, 2014.

[57] G. Aad *et al.*, "Search for contact interactions and large extra dimensions in the dilepton channel using proton-proton collisions at $\sqrt{s} = 8$ TeV with the ATLAS detector," *Eur. Phys. J.*, vol. C74, no. 12, p. 3134, 2014.

[58] G. Aad *et al.*, "Search for new particles in events with one lepton and missing transverse momentum in *pp* collisions at $\sqrt{s} = 8$ TeV with the ATLAS detector," *JHEP*, vol. 09, p. 037, 2014.

[59] V. Khachatryan *et al.*, "Search for physics beyond the standard model in dilepton mass spectra in proton-proton collisions at $\sqrt{s} = 8$ TeV," *JHEP*, vol. 04, p. 025, 2015.

[60] V. Khachatryan *et al.*, "Search for heavy gauge W' boson in events with an energetic lepton and large missing transverse momentum at $\sqrt{s} = 13$ TeV," *Phys. Lett.*, vol. B770, pp. 278–301, 2017.

[61] V. Khachatryan *et al.*, "Search for narrow resonances in dilepton mass spectra in proton-proton collisions at $\sqrt{s} = 13$ TeV and combination with 8 TeV data," *Phys. Lett.*, vol. B768, pp. 57–80, 2017.

[62] T. Sjöstrand, S. Mrenna, and P. Z. Skands, "A Brief Introduction to PYTHIA 8.1," *Comput. Phys. Commun.*, vol. 178, pp. 852–867, 2008.

[63] T. Sjöstrand, S. Ask, J. R. Christiansen, R. Corke, N. Desai, P. Ilten, S. Mrenna, S. Prestel, C. O. Rasmussen, and P. Z. Skands, "An Introduction to PYTHIA 8.2," *Comput. Phys. Commun.*, vol. 191, pp. 159–177, 2015.

[64] T. Fleig and M. Jung, "Model-independent determinations of the electron EDM and the role of diamagnetic atoms," 2018.

[65] M. Jung and A. Pich, "Electric Dipole Moments in Two-Higgs-Doublet Models," *JHEP*, vol. 04, p. 076, 2014.

[66] J. Engel, M. J. Ramsey-Musolf, and U. van Kolck, "Electric Dipole Moments of Nucleons, Nuclei, and Atoms: The Standard Model and Beyond," *Prog. Part. Nucl. Phys.*, vol. 71, pp. 21–74, 2013.

[67] J. Baron *et al.*, "Order of Magnitude Smaller Limit on the Electric Dipole Moment of the Electron," *Science*, vol. 343, no. 6168, pp. 269–272, 2014.

[68] W. C. Griffith, M. D. Swallows, T. H. Loftus, M. V. Romalis, B. R. Heckel, *et al.*, "Improved Limit on the Permanent Electric Dipole Moment of Hg-199," *Phys. Rev. Lett.*, vol. 102, p. 101601, 2009.

[69] T. Bhattacharya, V. Cirigliano, R. Gupta, H.-W. Lin, and B. Yoon, "Neutron Electric Dipole Moment and Tensor Charges from Lattice QCD," *Phys. Rev. Lett.*, vol. 115, no. 21, p. 212002, 2015.

[70] T. Bhattacharya, V. Cirigliano, S. Cohen, R. Gupta, A. Joseph, H.-W. Lin, and B. Yoon, "Iso-vector and Iso-scalar Tensor Charges of the Nucleon from Lattice QCD," *Phys. Rev.*, vol. D92, no. 9, p. 094511, 2015.

[71] C. A. Baker, D. D. Doyle, P. Geltenbort, K. Green, M. G. D. van der Grinten, *et al.*, "An Improved experimental limit on the electric dipole moment of the neutron," *Phys. Rev. Lett.*, vol. 97, p. 131801, 2006.

[72] J. Pendlebury *et al.*, "Revised experimental upper limit on the electric dipole moment of the neutron," *Phys. Rev.*, vol. D92, no. 9, p. 092003, 2015.

[73] V. Cirigliano, S. Gardner, and B. Holstein, "Beta Decays and Non-Standard Interactions in the LHC Era," *Prog. Part. Nucl. Phys.*, vol. 71, pp. 93–118, 2013.

[74] J. C. Hardy and I. S. Towner, "Superallowed $0^+ \rightarrow 0^+$ nuclear decays: 2014 critical survey, with precise results for V_{ud} and CKM unitarity," *Phys. Rev.*, vol. C91, no. 2, p. 025501, 2015.

[75] V. Cirigliano, J. Jenkins, and M. González-Alonso, "Semileptonic decays of light quarks beyond the Standard Model," *Nucl. Phys.*, vol. B830, pp. 95–115, 2010.

[76] M. González-Alonso, O. Naviliat-Cuncic, and N. Severijns, "New physics searches in nuclear and neutron β decay," 2018.

[77] Z. Bern *et al.*, "Left-Handed W Bosons at the LHC," *Phys. Rev.*, vol. D84, p. 034008, 2011.

[78] W. J. Stirling and E. Vryonidou, "Electroweak gauge boson polarisation at the LHC," *JHEP*, vol. 07, p. 124, 2012.

[79] G. Aad *et al.*, "Measurement of the polarisation of W bosons produced with large transverse momentum in pp collisions at $\sqrt{s} = 7$ TeV with the ATLAS experiment," *Eur. Phys. J.*, vol. C72, p. 2001, 2012.

[80] J. C. Collins and D. E. Soper, "Angular Distribution of Dileptons in High-Energy Hadron Collisions," *Phys. Rev.*, vol. D16, p. 2219, 1977.

[81] A. de Gouvea and J. Jenkins, "A Survey of Lepton Number Violation Via Effective Operators," *Phys. Rev.*, vol. D77, p. 013008, 2008.

[82] L. Lehman, "Extending the Standard Model Effective Field Theory with the Complete Set of Dimension-7 Operators," *Phys. Rev.*, vol. D90, no. 12, p. 125023, 2014.

[83] V. Cirigliano, W. Dekens, J. de Vries, M. L. Graesser, and E. Mereghetti, "Neutrinoless double beta decay in chiral effective field theory: lepton number violation at dimension seven," *JHEP*, vol. 12, p. 082, 2017.

[84] O. Brein, A. Djouadi, and R. Harlander, "NNLO QCD corrections to the Higgs-strahlung processes at hadron colliders," *Phys. Lett.*, vol. B579, pp. 149–156, 2004.

[85] G. Ferrera, M. Grazzini, and F. Tramontano, "Associated WH production at hadron colliders: a fully exclusive QCD calculation at NNLO," *Phys. Rev. Lett.*, vol. 107, p. 152003, 2011.

[86] G. Ferrera, M. Grazzini, and F. Tramontano, "Higher-order QCD effects for associated WH production and decay at the LHC," *JHEP*, vol. 04, p. 039, 2014.

[87] J. M. Campbell, R. K. Ellis, and C. Williams, "Associated production of a Higgs boson at NNLO," *JHEP*, vol. 06, p. 179, 2016.

[88] W. Astill, W. Bizon, E. Re, and G. Zanderighi, "NNLOPS accurate associated HW production," *JHEP*, vol. 06, p. 154, 2016.

[89] F. Maltoni, K. Mawatari, and M. Zaro, "Higgs characterisation via vector-boson fusion and associated production: NLO and parton-shower effects," *Eur. Phys. J.*, vol. C74, no. 1, p. 2710, 2014.

[90] F. Demartin, F. Maltoni, K. Mawatari, B. Page, and M. Zaro, "Higgs characterisation at NLO in QCD: CP properties of the top-quark Yukawa interaction," *Eur. Phys. J. C*, vol. 74, no. 9, p. 3065, 2014.

[91] K. Mimasu, V. Sanz, and C. Williams, "Higher Order QCD predictions for Associated Higgs production with anomalous couplings to gauge bosons," *JHEP*, vol. 08, p. 039, 2016.

[92] C. Degrande, B. Fuks, K. Mawatari, K. Mimasu, and V. Sanz, "Electroweak Higgs boson production in the standard model effective field theory beyond leading order in QCD," *Eur. Phys. J.*, vol. C77, no. 4, p. 262, 2017.

[93] A. Greljo, G. Isidori, J. M. Lindert, D. Marzocca, and H. Zhang, "Electroweak Higgs production with HiggsPO at NLO QCD," *Eur. Phys. J.*, vol. C77, no. 12, p. 838, 2017.

[94] G. Aad *et al.*, "Measurements of the Higgs boson production and decay rates and constraints on its couplings from a combined ATLAS and CMS analysis of the LHC pp collision data at $\sqrt{s} = 7$ and 8 TeV," *JHEP*, vol. 08, p. 045, 2016.

[95] J. Charles, A. Höcker, H. Lacker, S. Laplace, F. R. Le Diberder, J. Malclès, J. Ocariz, M. Pivk, and L. Roos, "CP violation and the CKM matrix: Assessing the impact of the asymmetric B factories," *Eur. Phys. J.*, vol. C41, pp. 1–131, 2005.

[96] M. Aaboud *et al.*, "Searches for the $Z\gamma$ decay mode of the Higgs boson and for new high-mass resonances in *pp* collisions at $\sqrt{s} = 13$ TeV with the ATLAS detector," *JHEP*, vol. 10, p. 112, 2017.

[97] G. Perez, Y. Soreq, E. Stamou, and K. Tobioka, "Constraining the charm Yukawa and Higgs-quark coupling universality," *Phys. Rev.*, vol. D92, no. 3, p. 033016, 2015.

[98] Y. T. Chien, V. Cirigliano, W. Dekens, J. de Vries, and E. Mereghetti, "Direct and indirect constraints on CP-violating Higgs-quark and Higgs-gluon interactions," *JHEP*, vol. 02, p. 011, 2016. [JHEP02,011(2016)].

[99] Y. Soreq, H. X. Zhu, and J. Zupan, "Light quark Yukawa couplings from Higgs kinematics," *JHEP*, vol. 12, p. 045, 2016.

[100] F. A. Dreyer and A. Karlberg, "Vector-Boson Fusion Higgs Production at Three Loops in QCD," *Phys. Rev. Lett.*, vol. 117, no. 7, p. 072001, 2016.

[101] M. Cacciari, F. A. Dreyer, A. Karlberg, G. P. Salam, and G. Zanderighi, "Fully Differential Vector-Boson-Fusion Higgs Production at Next-to-Next-to-Leading Order," *Phys. Rev. Lett.*, vol. 115, no. 8, p. 082002, 2015.

[102] A. Kusina, T. Stavreva, S. Berge, F. I. Olness, I. Schienbein, K. Kovarik, T. Jezo, J. Y. Yu, and K. Park, "Strange Quark PDF Uncertainty and its Implications for W/Z Production at the LHC," 2013. [Acta Phys. Polon. Supp.6,219(2013)].

[103] M. Cacciari, M. Greco, and P. Nason, "The p t spectrum in heavy-flavour hadroproduction," *Journal of High Energy Physics*, vol. 1998, no. 05, p. 007, 1998.

[104] R. K. Ellis, W. J. Stirling, and B. R. Webber, "QCD and collider physics," *Camb. Monogr. Part. Phys. Nucl. Phys. Cosmol.*, vol. 8, pp. 1–435, 1996.

[105] A. Mitov, S. Moch, and A. Vogt, "Next-to-Next-to-Leading Order Evolution of Non-Singlet Fragmentation Functions," *Phys. Lett.*, vol. B638, pp. 61–67, 2006.

[106] S. Moch and A. Vogt, "On third-order timelike splitting functions and top-mediated Higgs decay into hadrons," *Phys. Lett.*, vol. B659, pp. 290–296, 2008.

[107] A. A. Almasy, S. Moch, and A. Vogt, "On the Next-to-Next-to-Leading Order Evolution of Flavour-Singlet Fragmentation Functions," *Nucl. Phys.*, vol. B854, pp. 133–152, 2012.

[108] M. Miyama and S. Kumano, "Numerical solution of Q**2 evolution equations in a brute force method," *Comput. Phys. Commun.*, vol. 94, pp. 185–215, 1996.

[109] M. Cacciari, P. Nason, and C. Oleari, "A Study of heavy flavored meson fragmentation functions in e+ e- annihilation," *JHEP*, vol. 04, p. 006, 2006.

[110] G. Tsamasphyros and P. S. Theocaris, "Numerical inversion of Mellin transforms," *BIT Numerical Mathematics*, vol. 16, pp. 313–321, Sep 1976.

[111] C. W. Bauer, F. J. Tackmann, and J. Thaler, "GenEvA. I. A New framework for event generation," *JHEP*, vol. 12, p. 010, 2008.

[112] C. W. Bauer, F. J. Tackmann, and J. Thaler, "GenEvA. II. A Phase space generator from a reweighted parton shower," *JHEP*, vol. 12, p. 011, 2008.

[113] S. Alioli, C. W. Bauer, C. Berggren, A. Hornig, F. J. Tackmann, C. K. Vermilion, J. R. Walsh, and S. Zuberi, "Combining Higher-Order Resummation with Multiple NLO Calculations and Parton Showers in the GENEVA Monte Carlo Framework," in *Proceedings, 48th Rencontres de Moriond on QCD and High Energy Interactions: La Thuile, Italy, March 9-16, 2013*, pp. 313–316, 2013.

[114] H.-L. Lai, M. Guzzi, J. Huston, Z. Li, P. M. Nadolsky, J. Pumplin, and C. P. Yuan, "New parton distributions for collider physics," *Phys. Rev.*, vol. D82, p. 074024, 2010.

[115] S. Frixione, Z. Kunszt, and A. Signer, "Three jet cross-sections to next-to-leading order," *Nucl. Phys.*, vol. B467, pp. 399–442, 1996.